Ab initio STUDY OF THE EFFECT OF SOLUTE ATOMS ON VACANCY DIFFUSION IN NI-BASED SUPERALLOYS

by

KAMAL NAYAN GOSWAMI

A thesis submitted to
The University of Birmingham
for the degree of
DOCTOR OF PHILOSOPHY

School of Metallurgy and Materials
College of Engineering and Physical Sciences
The University of Birmingham
December 2016

Dedicated to my late grandfather, who was the first teacher in my life

ACKNOWLEDGEMENTS

PUBLICATIONS

- K. N. Goswami and A. Mottura. *Can slow-diffusing solute atoms reduce vacancy diffusion in advanced high-temperature alloys?*. Materials Science and Engineering: A, 617:194-199, November 2014.

- K. N. Goswami and A. Mottura. *A kinetic Monte Carlo study of vacancy diffusion in non-dilute Ni-Re alloys* (under preparation).

Abstract

Single crystal Ni-based superalloys are used in the highest temperature components in jet turbine engines owing to their excellent properties under creep conditions. These alloys owe their properties greatly to their chemical composition, and in particular the addition of slow diffusing elements like Re and W delays the creep deformation significantly. The microstructure in these alloys comprises of cuboids of the hard precipitate phase γ' embedded in a matrix of softer phase γ. At high temperatures, the creep dislocations gliding through γ do not shear the γ' precipitates and hence these dislocations have to climb around the γ' precipitates along the γ / γ' interfaces in order to continue gliding. The climb of dislocations requires the absorption and emission of vacancies at the dislocation cores depending on the direction of climb. This sets up a concomitant flux of vacancies in the γ phase which have to diffuse from emitting cores to absorbing cores. Vacancy diffusion through the γ phase has been suggested to be the rate-controlling process and determines how fast the vacancies are made available for creep deformation to continue. Slow diffusing elements like Re and W partition to the γ phase and are expected to interact with the vacancies in slowing them down. The objective of the present investigation is to calculate the effect of chemical composition in γ on the rate of vacancy diffusion. *Ab initio* electronic structure calculations based on density functional theory have been used to calculate the thermodynamic and kinetic parameters in both dilute as well as non-dilute alloys. Binary alloys of Re, W and Ta in Ni were considered. Ta is a fast diffusing solute in Ni and was also included in the present investigation to understand how the vacancy diffusion is affected by the presence of fast diffusing elements. Analytical formulations were used to calculate the diffusion coefficients. Kinetic Monte Carlo simulations were performed as a theoretical experiment to calculate the vacancy diffusion coefficient particularly in the non-dilute systems where the accuracy of analytical formulations were marred by a number of simplifying assumptions. Results from calculations on dilute alloys

using analytical formulations based on Manning's random alloy model suggested that the role of both slow as well as fast diffusers on the vacancy diffusion coefficients was minimal. However, results from kinetic Monte Carlo simulations on dilute as well as non-dilute alloys suggested appreciable modifications of the vacancy diffusion coefficients, suggesting that the beneficial role of slow-diffusing atoms in Ni-based superalloys could be partly explained by their effect on vacancy diffusion.

TABLE OF CONTENTS

7   Conclusions and Scope for Future Work   137

List of References   140

LIST OF FIGURES

LIST OF TABLES

CHAPTER 1

INTRODUCTION

Ni-based superalloys represent a class of materials designed to withstand extreme conditions [1]. Their excellent performance under high temperature creep conditions, amongst others, make them suitable for applications such as turbine blades in gas turbine engines used for jet propulsion in civil and military aircrafts (see Figure 1.1). From thermodynamic considerations, high engine efficiencies are achieved at high operating temperatures and over the past few decades, the improvements in superalloy technology have raised the temperature capability of the gas turbine engines beyond 1273 K [1]. This has mostly been achieved by altering the chemical composition of these superalloys considerably. The addition of Re, a rare and expensive metal, in particular was seen to have a strong creep strengthening effect. But even as the improvement in strength is clearly seen, an understanding of the fundamental mechanism leading to the observed strengthening is still lacking [2]. High temperature creep is dependent on the rate of vacancy diffusion and an accepted argument within the superalloys community is that slow diffusing atoms, like Re, slow down the vacancy diffusion, leading to the lowering of creep deformation rate [2]. Other important elements like Ta, W and Mo are also potent strengtheners, albeit to a lesser degree. The present work aims at investigating the effect of various alloying additions on the vacancy diffusion in Ni based superalloys from a variety of computational techniques in an attempt to explain the observed strengthening as well as to generate meaningful diffusion data for future alloy design programmes.
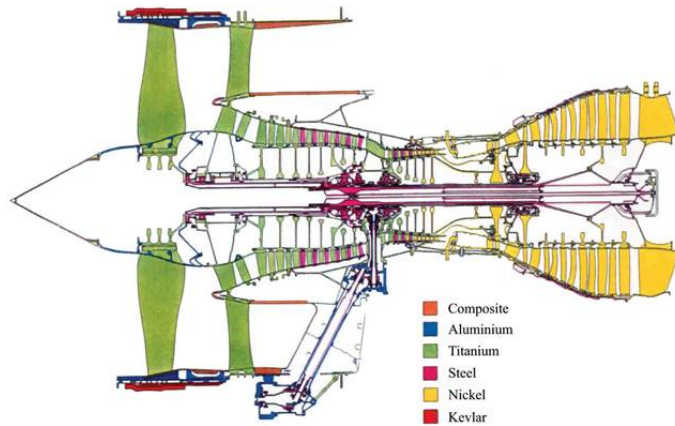
Figure 1.1: A schematic of the longitudinal section of a jet engine showing the materials used. Ni-based superalloys (in yellow) are used in the combuster and turbine sections[1]
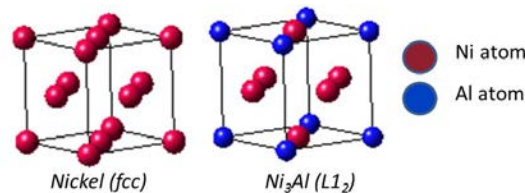
Figure 1.2: Ni representing the γ phase and Ni$_3$Al the ordered γ' phase. In a superalloy, various alloying additions are made which substitute for Ni or Al in one or both the phases

1.1 Physical metallurgy of Ni-based superalloys

Single crystal Ni-based superalloys, simply put are γ-γ' alloys where γ phase is the random substitutional solid solution of Ni and γ' phase is the Ni$_3$Al based ordered phase with a $L1_2$ structure(see Figure 1.2) [1]. The choice of Ni as the base element for superalloys comes from the fact that it has a face centred cubic crystal structure from ambient temperature up to its melting temperature of 1728 K. An *fcc* structure means that Ni is ductile and tough [1] and no phase transformations ensures that there is no unwanted expansion or contraction at high temperatures. The *fcc* structure is a closed-packed structure with 12 possible slip systems [3] resulting in higher ductility compared to other crystal structures. The outer d-electrons in Ni form strong cohesive bonds leading to the high strength [1]. Also, compared to other *fcc* metals in the transition series, it has a lower rate of self-diffusion which gives the structure more stability under creep conditions. The γ phase forms a continuous matrix in which cuboidal precipitates of γ' phase are embedded
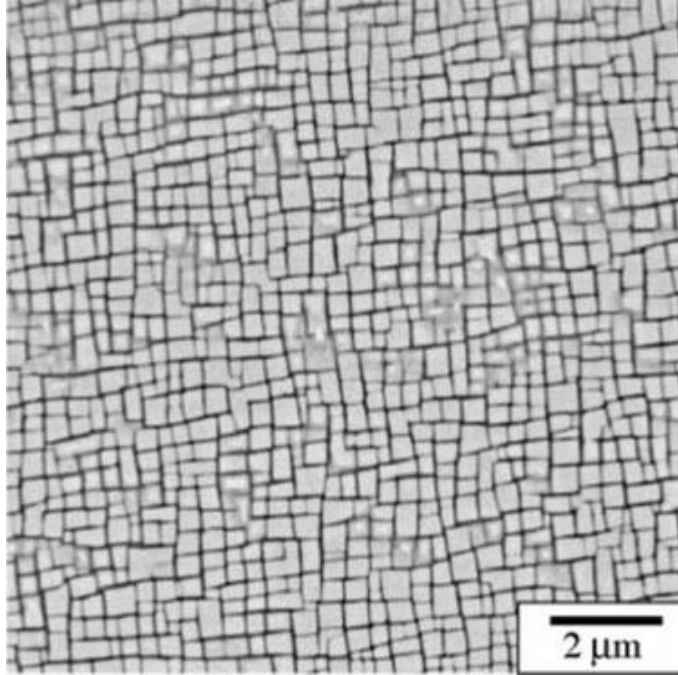
Figure 1.3: The γ-γ' microstructure of a commercial superalloy CMSX-4 [1]

in a coherent manner with its <001> crystallographic direction aligned to the <001> crystallographic direction of the γ phase. The γ' phase gives order strengthening and exhibits anomalous yielding phenomena, a characteristic unique to some $L1_2$ phases where the strength of the γ' phase increases with temperature [4]. For this reason, their volume fraction is kept as high as 70 %. Figure 1.3 shows a typical microstructure for a commercial Ni-based superalloy CMSX-4. One can clearly see the high volume fraction of the γ' phase embedded in thin γ matrix. There are other phases known as Topologically Closed Packed (TCP) phases [5] which sometimes form during processing or service conditions, however they are detrimental to the creep performance and are hence undesirable.

From a historical point of view, the superalloys have been in use since the 1940s. Advancements in the casting technologies led to a shift from wrought to cast alloys with equiaxed structure, and then from equiaxed structure to columnar structure using directional solidification methods (see Figure 1.4) [1]. Modern day turbine blades are made of single crystal superalloys using the investment casting methods [6]. These alloys show drastic improvements in creep performance when compared to the previous versions. As grain boundaries are completely removed, grain boundary sliding/migration which are

3
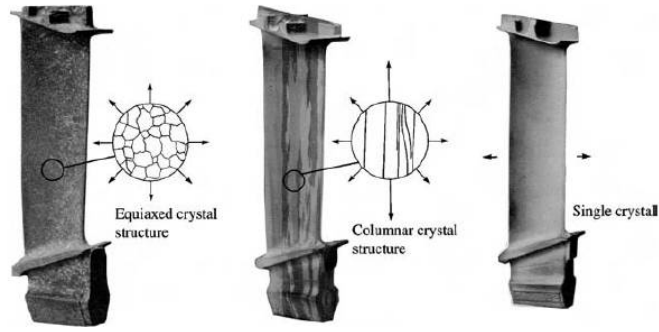
Figure 1.4: The turbine blades in equiaxed, columnar and single crystal forms [1].

common at high temperatures are taken out of the equation [1]. Also, elements like B and C previously added to the polycrystalline Ni-based superalloys, which promoted the formation of eutectic mixtures during casting, are no longer needed. Absence of grain boundaries also reduces the occurrence of incipient melting during further heat treatments. The as-cast dendritic structure is homogenised by a solutioning treatment to remove the micro-segregation in the composition and to dissolve eutectic mixtures rich in γ'. Further ageing treatment leads to the formation of γ' precipitates with optimum size and uniform distribution [1].
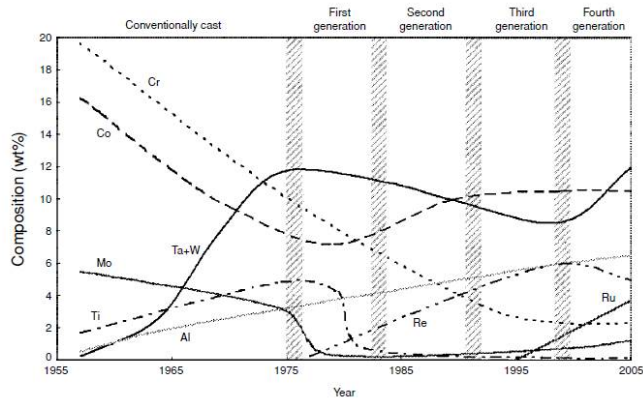
Figure 1.5: Trends in the Ni-based superalloy chemistry over the years [1].

Superalloys are highly alloyed systems with over 10 alloying additions (see Figure 1.5). Each added element has a specific role and a preference for a particular phase. The most common elements include Al, Ta, Ti, W, Re, Mo, Cr, Co and Ru. Grain boundary strengthening elements like B and C which were added earlier are no longer needed since modern blades used in the hottest parts of jet engines are now single-crystal blades. Al and

4

Ta are strong γ' formers and are present in appreciable amounts in modern superalloys. W, which otherwise partitions to the γ' phase is rejected towards γ in the presence of Ta [7] where it acts as a solid solution strengthener. Re, the main subject of the current study, on the other hand strongly partitions to the γ phase and has a dramatic effect on improving the creep lives of superalloys [8]. Infact, second and third generation of superalloys are marked by the addition of 3 wt. % and 6 wt. % of Re respectively [1]. Fourth generation superalloys are marked by the addition of Ru which reduces the propensity of the formation of TCP phases on the addition of Re [9].

1.2   High temperature creep

Creep is a manifestation of inelastic behaviour which becomes significant in metals only at high temperatures, where the strain in the material increases with time under constant stress. This occurs even at stresses substantially lower than the yield strength of the material. Ni-based superalloys are used in high temperature applications where deformation due to creep becomes significant. As an example, in CMSX-4, which is a second generation superalloy, the yield strength at 1223 K is about 600 MPa, however even a stress of 200 MPa can cause a creep strain of 5 % after 1800 h [1]. Consequently, with time, strain will be accumulated and excessive creep deformation will cause failure of the component. The jet engine components such as the turbine blades are machined to fit tight tolerances and hence creep strains greater than a few percent render them unfit for service[1].

In the case of Ni-based superalloys, a number of regimes for the different mechanisms of creep deformation have been identified based on the applied stress and temperature as shown in Figure 1.6 [1]. Figure 1.7 shows the creep curves in different regimes for a second-generation superalloy CMSX-4. At low temperatures (<1023 K), the superalloys undergo primary creep deformation with a decrease in strain rate with strain. Shearing of the γ' precipitates is possible at sufficiently high stresses (>500 MPa) by complex dislocation reactions. Creep at very high temperatures (>1323 K) is characterised by di-
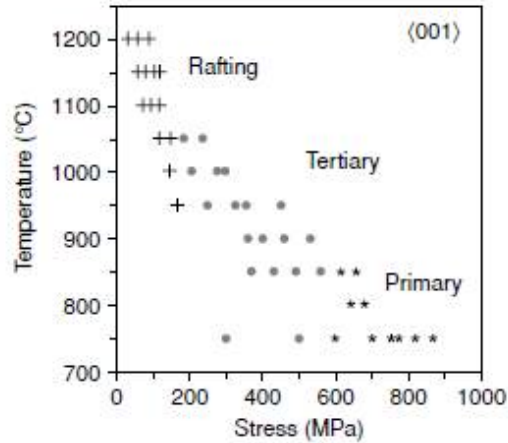
Figure 1.6: Applied stress and temperature conditions for the different creep regimes to operate [1].

rectional coarsening of the γ' precipitates to form rafts and by the formation of equilibrium dislocation networks at the γ/γ' interfaces [10].

However, across wide ranges of temperatures and applied stresses, in the intermediate tertiary regime, creep dislocations do not penetrate the γ' precipitates [1]. The slip is of the a/2<1$\bar{1}$0>{111} type and is limited to the γ channels. The dislocations dissociate into two Shockley partials of the a/6<112> type separated by an intrinsic stacking fault. No shearing of the γ' precipitates occur, and hence, substantial cross-slip or climb is required for the dislocations to avoid the precipitates. The creep therefore occurs by a glide-plus-climb mechanism. The glide step produces almost all of the strain, but the climb controls the velocity. And since dislocation climb relies on diffusional processes, it can be assumed that the rate controlling step is diffusion [2].

1.3 The Rhenium effect

The first generation of single crystal Re-free superalloys were followed by the second generation superalloys in the 1990s and third generation superalloys in the 2000s marked by the addition of 3 wt.% and 6 wt.% Re respectively. The pioneering studies on the Re addition to single crystal Ni-based superalloys was conducted by Giamei et al [8, 11].

6
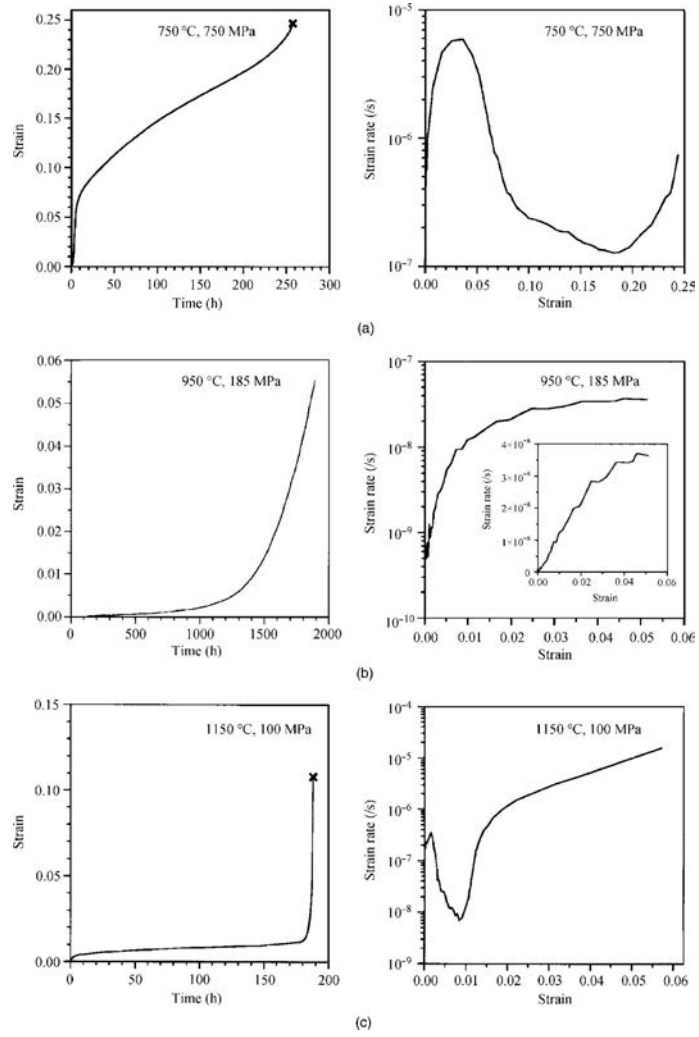
Figure 1.7: Constant load creep data for CMSX-4 in different regimes [1].
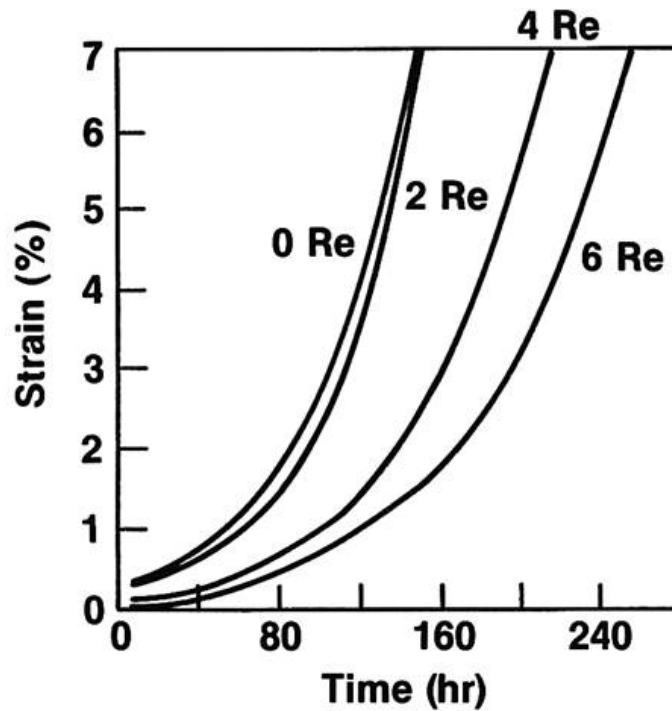
Figure 1.8: Effect of Re addition on a model alloy 444 (Temperature =1172 K, applied stress =380 MPa)[11].

In this study, Re was added to a modified MAR-M200 alloy to replace W, keeping the W+Re wt.% constant. Four alloys with 0, 2 , 4 and 6 wt.% Re were tested in creep at 1172 K and 380 MPa. Figure 1.8 shows the tertiary creep curves from the study of Giamei et al [11] clearly demonstrating how Re addition helps delay the accumulation of creep strain. Since then several other investigtions have been carried out, which confirmed the beneficial role of Re addition under tertiary creep [12, 13, 14, 15]. However, Re is one of the most expensive transition metals, so much so that it could be responsible for up to half the cost of the raw material needed to make the turbine blades [2] .The high price and limited availability of Re makes it important to understand the underlying mechanisms for the observed creep strengthening, such that in the future, the amount of Re added can be reduced for cost related benefits.

Re almost entirely partitions to the γ phase, reduces the γ' coarsening rate and also increases the γ/γ' misfit . However, these properties do not explain the beneficial role of Re as seen in the tertiary creep regime in Ni-based superalloys. Several investigations

8

have been carried out to elucidate the role of Re in creep strengthening.

1.3.1   Solid solution strengthening

Addition of solute atoms to a solvent lattice forms a solid solution which is invariably stronger than the solvent [3]. The solute additions increase the yield stress and the level of the stress-strain curve as a whole [16]. These solute atoms, thus, offer resistance to dislocation motion, which leads to the observed strengthening. Traditionally, the solid solution strengthening is thought to be related to the elastic interaction between the solute atoms and the dislocations owing to the size misfit between the solute and the solvent atoms. The distortions produced by the solute atoms in the solvent lattice interact with the elastic stress fields produced by the core of the dislocations, and hence the solid solution strengthening should be directly proportional to the size misfit of the solute atom. However, this is not the case as other factors also play an important role. Solid solution strengthening also encompasses other effects such as modulus misfit, valence effects, effects on stacking fault energy (see Section (1.3.2)). Also, clustering and short range ordering can play a role, more on which has been discussed in Section (1.3.3). Since creep deformation is mostly limited to the γ phase at high temperatures, it is reasonable to assume that Re plays a part in hindering dislocation glide in the γ phase.

Gan et al [17] used variety of instrumented indentation techniques to quantify the degree of solid solution strengthening for many transition metals in binary Ni alloys. It was ensured that all the binary alloys were single phase γ alloys and were properly homogenized to do away with any role of clustering or ordering. It was shown that the solutes which had a larger atomic radius also showed a higher compressibility in the Ni lattice and hence the effect of atomic size misfit was minimum. The alloy hardness was found to vary with the solute species with Nb, Ta, Rh and Ir showing maximum potency for solid solution hardening, while Re only had a minimal effect (see Figure 1.9). It was argued that the potency of solute atoms in solid solution strengthening should be governed by their effect on the stacking fault energies in Ni.
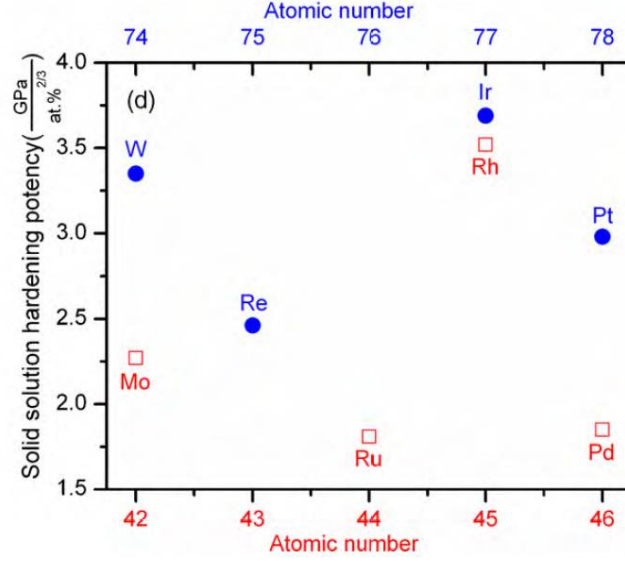
Figure 1.9: Solid solution hardening potency for the different solutes in binary Ni alloys[17].

1.3.2 Stacking fault energy

The slip system in *fcc* crystals is a/2<1$\bar{1}$0>{111} which means the deformation in these crystals should take place by the gliding of dislocations causing a slip along the 1/2<1$\bar{1}$0> direction on the close-packed {111} planes. However, it is energetically favourable for these dislocations to split into two partial dislocations of the a/6<112> type. These dislocations are known as Shockley partials. One can clearly see that the reaction is energetically favourable by applying the Frank's rule, which states that the energy of a dislocation is proportional to the square of its Burgers vector [18]:

$$\frac{a}{2}\langle 110 \rangle \{\bar{1}11\} \rightarrow \frac{a}{6}\langle 211 \rangle \{\bar{1}11\} + \frac{a}{6}\langle 12\bar{1} \rangle \{\bar{1}11\} \qquad (1.1)$$

The passage of a perfect dislocation does not create a planar defect. However, the passage of the first Shockley partial dislocation creates an intrinsic stacking fault (ISF) by locally changing the atomic coordination. In *fcc* crystals, the ABCABCABCABC packing sequence is changed to ABCACABCABC, thus creating two neighbouring planes with the *hcp* coordination locally [18]. This intrinsic stacking fault is removed on the passage of the second Shockley partial dislocation [18]. Thus, in principle, we have two
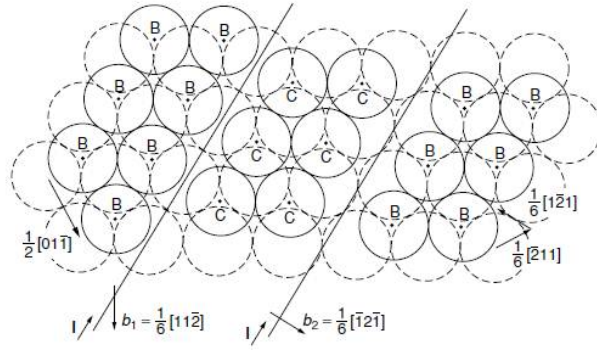
Figure 1.10: Two Shockley partials and a stacking fault on a {111} plane in the γ phase [1].

partial dislocations and a stacking fault in between (see Figure 1.10). When encountering a barrier, these partial dislocations must recombine for either cross-slip or climb depending on their character, *i.e.* edge or screw. The separation between the two partial dislocations depends on their elastic repulsion and also on the stacking fault energy (SFE) [18]. The lower the SFE, the larger is the separation between the two partial dislocations, and it is comparatively difficult for them to come together and recombine. Thus, another hypothesis for the observed creep strengthening by Re could be connected to the fact that it may play a significant role on the reduction in SFE in Ni-based superalloys [19].

Ni has one of the highest SFE of the various *fcc* metals. This is of the order of 120 - 130 mJ/ m^2 [20], and almost all alloying additions lower the SFE values in Ni. Yu et al [21] and Shang et al [20] studied the effect of alloying additions on the SFE in dilute binary alloys of Ni using density functional theory calculations. A reduction of about 25 mJ/m^2 was calculated for Re at a temperature of 0 K. This reduction increases further at 300 K. However, the reduction was similar in magnitude to other alloying elements like W and Mo. Thus, Re does not overshadow the others in terms of reduction in SFE. Pettinari et al [22] and Diologent et al [23] have also examined the role of Re on SFE in the γ phase of commercial Ni-based superalloys through experiments. Different alloys with and without Re were studied with a wide range of variation in composition. However, both studies confirmed that there was hardly any difference between the SFE of Ni-based alloys with and without Re, and the values always lie between 20 - 32 mJ/m^2 Hence, the hypothesis

that Re plays a significant role in the reduction of SFE in Ni-based superalloys has to be excluded.

1.3.3 Cluster formation and short range ordering

Blavette et al [12] had suggested from 1-dimensional atom probe tomography studies that Re forms clusters in Ni, a finding that was later supported by Wanderka et al [24]. Clusters of solute atoms can act as better hindrance to dislocation glide than individual solute atoms and hence they argued that the observed creep strengthening on Re addition is due to the formation of Re clusters in Ni. Indeed, the Ni-Re system shows a miscibility gap [25] and hence one could expect Re to show clustering especially at lower temperatures, however, since the operating temperatures of Ni-based superalloys is high, the entropy effects are likely to overcome these clustering tendencies. In their studies, Blavette et al [12] and Wanderka et al [24] found that the number of Re atoms in different atomic layers showed a deviation from that expected from a random distribution of Re atoms. Some atomic layers had fewer than random number of Re atoms, while other layers had more than a random number of Re atoms. However, the conclusions from these 1-D APT studies were based on datasets which consisted of a few thousand atoms, and hence the statistical viabilty of these studies can be questioned. Moreover, these deviations from random distribution do not clarify if there is a tendency for clustering or short range ordering (SRO). Later 3-D APT studies were conducted by Mottura et al [26, 27] to study the Re-clustering in Ni-based superalloys as well as in binary Ni-Re alloys. 3-D APT had a clear advantage over 1-D APT in terms of statistical accuracy given that the dataset collected consisted of hundreds of millions of atoms. Their results clearly showed that Re is distributed randomly in Ni and that the presence of some clusters is indispensible due to the statistical fluctuations. However, one must point out that the use of APT to study clustering can be problematic since there are systematic errors in the measured atomic positions. Other techniques like extended X-Ray absorption fine spectroscopy (EXAFS) which can determine the local atomic environment around an atom was also conducted
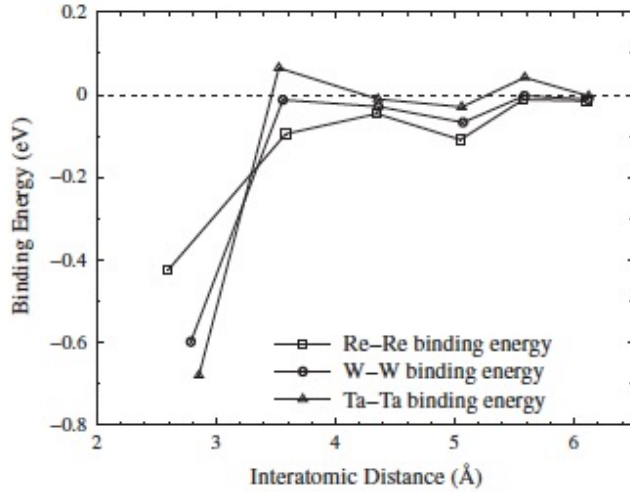
Figure 1.11: Calculated binding energies for Re-Re, W-W and Ta-Ta pairs [29].

by Mottura et al [28] to study Re clusters in Ni. Again, results from these studies showed that Re is coordinated by 12 Ni atoms, and no evidence was found for Re clustering in Ni.

To complement these experimental studies, Mottura et al [29] also performed theoretical calculations based on density functional theory. Binding energies were calculated for Re-Re nearest neighbour pairs in Ni and these results are shown in Figure 1.11 together with the results for Ta and W. From definition, a negative binding energy means that the pair is energetically unfavourable. A negative binding energy was calculated for the Re-Re first nearest neighbour pairs while on further separation of Re atoms, the magnitude of the binding energy dropped significantly. Similar results were found for Ta and W. Also, binding energy calculations on small Re clusters up to 4 atoms in size also showed that they were energetically unfavourable. It must, however, be pointed that the calculations performed by Mottura et al [29] did not include magnetism and it is a matter of debate whether results from non-magnetic calculations at 0 K are representative of Ni alloys at high temperature as Ni loses its ferromagnetic property above its Curie temperature of 630 K [30]. According to He et al [31], the local magnetic moments in Ni fluctuate at finite temperatures leading to a nonzero local magnetic moment. A complete consideration of the Gibbs free energy at high temperature should thus include the thermal magnetic

excitations, which is a formidable task at the present time [31]. Indeed, He et al [31] have calculated enthalpies of formation in various Ni-Re alloys and found that magnetism plays an important role. The nonmagnetic and ferromagnetic formation enthalpies of random alloys in the Ni rich part of the Ni-Re system showed a drastic change from ordering to phase separation [31]. Other theoretical studies [32] predicted the presence of an ordered intermetallic Ni_4Re with the $D1_a$ structure from ferromagnetic calculations in the Ni-Re system at lower temperatures. This intermetallic phase is expected to dissolve at higher temperatures due to entropy effects, but the authors argued that some remnant short range ordering is expected. However, given the slow diffusion rate of Re in Ni, the formation of this ordered intermetallic phase at lower temperatures and the associated SRO is questionable, and needs to be validated by experiments.

1.3.4 Enrichment at the γ/γ' interface

Re enrichment in the γ phase close to the γ/γ' interfaces was observed in several Ni-based superalloys [33, 34] from atom probe studies. Given that the dislocations have to climb at the γ/γ' interfaces for creep deformation to proceed, such enrichments could pin the dislocations, making it difficult for them to climb. This enrichment appeared to be in the form of a 'bow wave' of Re in the γ phase ahead of the γ' interface [33, 34] and it was more pronounced than some of the other elements. Ge et al [35] on the other hand found no evidence of Re enrichments in the γ phase in the uncrept samples, but found regions enriched in Re in the γ phase close to the interface in the crept samples. They also argued that aggregation of Re near the dislocation cores, would mean that vacancies would have to exchange positions with a Re atom for climb, and given the high energy barrier for this [36], it would make climb more difficult.

Given these observations, it was important to understand if the observed enrichment was due to the rejection of Re during coarsening of the γ' precipitates at the service temperature or was it because of the γ' phase growth on cooling. In either case, the movement of the γ/γ' interface could be achieved by the diffusion of γ' forming elements

like Al and Ta towards the γ' phase, with a concomitant rejection of γ phase formers like Re. Phase field simulations were done to understand this phenomena by Mottura et al [27] by predicting the γ/γ' interface growth on cooling from high temperatures and the simulations accurately predicted the composition profiles close to the γ/γ' interfaces when compared to their own atom probe data. It was shown that the movement of the γ/γ' interface was strongly dependent on the cooling rate and the interface movement was small on fast cooling, which can possibly explain why no Re enrichment was found in the case of Ge et al [35] for uncrept samples. Thus, it was clear that the growth of the γ/γ' interface is diffusion-limited, as the diffusion of solute elements is not fast enough to reach equilibrium. Given the replication of the enrichment/depletion of the solute elements near the interface by these cooling simulations when compared to the experiments, it was concluded that the observed Re enrichment was due to the rejection of Re from the growing γ' precipitates on cooling from high temperatures and that such enrichments were not expected at the service temperatures [27]. It was also observed that in cases where secondary γ' precipitates formed inside the γ matrix, the extent of the γ/γ' interface migration was small. It was evident because diffusion over smaller distances was required, and γ' forming elements like Al and Ta which were further away from primary γ' precipitates need not be transported for long distances. Warren et al [33] had also seen Re enrichments near the spherical secondary γ' precipitates similar in size to the ones near the primary γ' precipitates. The secondary γ' precipitates can only form inside the γ phase on cooling, and hence they concluded that the Re enrichments near the primary γ' precipitates also must have formed on cooling from high temperatures, and hence one should not expect Re-enrichments at the γ/γ' interfaces at the operating temperatures of Ni-based superalloys.

Motivation for the present work

All the above-mentioned studies remain inconclusive in their determination of the Re-effect. This leads us to examine if the creep strengthening due to Re can be attributed to
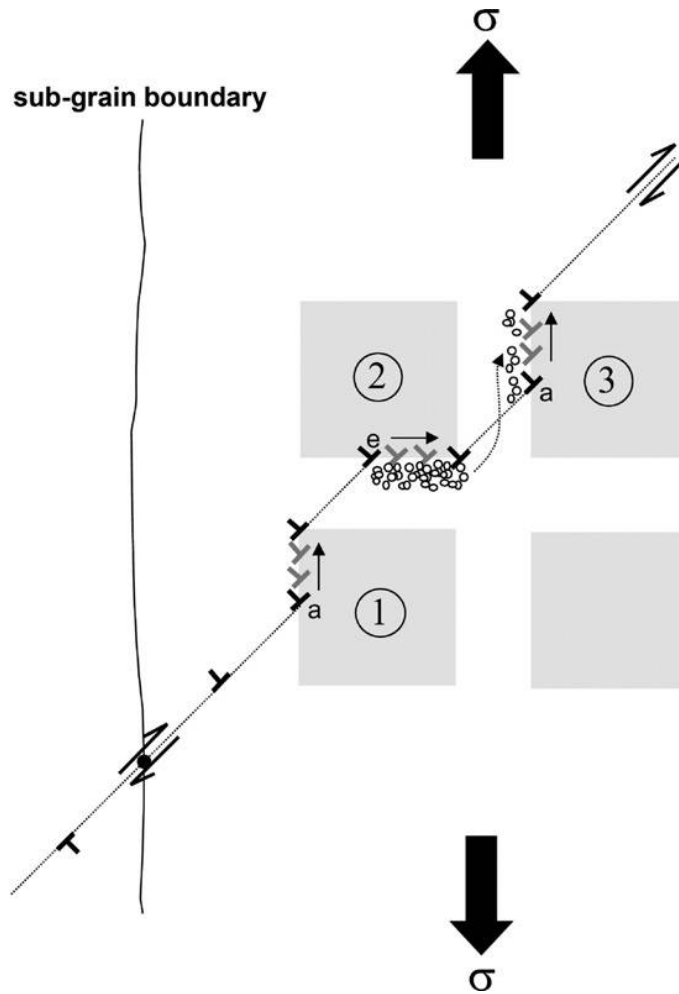
Figure 1.12: Combined glide-plus-climb mechanism in the tertiary regime [38].

its slow diffusion rate in Ni. Janotti et al [36] and Karunaratne et al [37] have determined the vacancy assisted diffusion coefficients for a number of elements in binary Ni systems. Both observe that Re is the slowest diffusing element in Ni, amongst the important solute elements added to Ni-based superalloys. Re is therefore expected to retard the diffusion controlled processes. It is therefore important to delve deeper into the role of solute elements on the diffusion in Ni-based superalloys.

1.4 Dislocation mechanisms and the role of vacancy diffusion

Across a wide range of temperature and stress combinations in the tertiary creep regime, the deformation in Ni-based superalloys is restricted to the thin γ channels [1], as discussed earlier. The gliding dislocations do not penetrate the γ' precipitates and hence they have to climb around them at the γ/γ' interfaces for deformation to continue. Depending on the microstructure and the loading direction, the dislocations have to either climb up or down. The upward dislocation climb is associated with the absorption of vacancies, while the downward dislocation climb is associated with the emission of vacancies. Figure 1.12 shows that the dislocation climb along the horizontal γ channels releases vacancies, while vacancies are absorbed along the vertical γ channels [38]. This creates a simultaneous flux of vacancies from the horizontal to the vertical channels. Slow diffusing solutes such as Re and W partition to the γ phase where they could act as strong hindrances to the diffusion of vacancies. Infact, this is the accepted argument within the superalloys community for the origin of the Re-effect [29].

Quantitative estimations of how chemistry affects the diffusion of vacancies are also desirable since these may be used to inform deformation models at the higher length-scales. Many implementations of discrete dislocation dynamics (DDD) are becoming mature enough to treat dislocation climb explicitly, and assume that the flow of vacancies to and from the cores is the rate-controlling mechanism [39] and [40]. Others assume a value of 10, 100 and 1000 for the ratio of the mobilities of glide and climb, expecting this ratio to be dependent on temperature and alloy composition [41]. Similarly, constitutive creep models commonly show that the minimum creep strain rate, $\dot{\epsilon}$ is proportional to an effective diffusion factor D_{eff}, which is thought to be strongly influenced by chemistry such as the presence of slow-diffusing atoms [38, 42].

$$\dot{\epsilon} \propto D_{\text{eff}} \tag{1.2}$$

Our hypothesis is that the vacancy diffusion coefficient D_v is proportional to the effective diffusion coefficient D_{eff} and hence is an equivalent measure of D_{eff}. This is because the diffusion of vacancies in the γ matrix in one direction means the simultaneous diffusion of atoms (predominantly Ni) in the reverse direction. Similar to D_{eff}, the vacancy diffusion coefficient D_v is also dependent on the composition of the alloy and a reliable estimate of how single solute atoms may affect vacancy diffusion is needed.

1.5   Macroscopic diffusion theory

Before we discuss the atomic mechanisms of diffusion in the next chapter, a brief summary of some of the concepts in macroscopic diffusion is presented here.

1.5.1   Fick's laws of diffusion

Consider a gas in a thin-walled pressure vessel, the concentration at the inner surface of which is maintained at a constant level C. The gas diffuses through the thin walls and escapes to the surroundings. The concentration at the outer surface is thus zero. Assuming that the diffusion is happening along the x-axis, this would eventually lead to a steady state concentration gradient $\frac{\partial C}{\partial x}$ of the gas in the wall, and the flux of the gas J passing through the pressure vessel can be given as,

$$J = -D\frac{\partial C}{\partial x} \tag{1.3}$$

where D is the diffusion coefficient of the gas and has the units of m^2/s. Flux is the amount of gas passing through a unit area in a unit time and has the units of mol/m^{2}s. Equation (1.3) is called the Fick's first law of diffusion [43]. However, in most practical situations, the steady-state condition is never established and the concentration varies with both distance and time. For those cases, we have Fick's second law of diffusion [43],
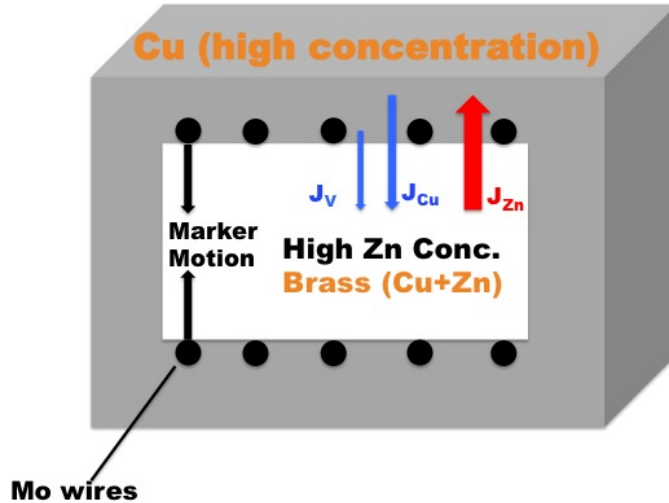
Figure 1.13: A schematic of the Kirkendall's diffusion experiment on α-brass (source - Wikipedia)

$$\frac{\partial C}{\partial t} = \frac{\partial}{\partial x}\left(D\frac{\partial C}{\partial x}\right) \tag{1.4}$$

Solving for Equation (1.4), one can obtain the concentration profile as a function of distance x at any given time t. However, it must be noted that the thermodynamic driving force for diffusion is not the concentration gradient, but the chemical potential gradient, as this leads to a decrease in the overall Gibbs free energy [44]. In some cases, this requires uphill diffusion, which is the diffusion from a lower concentration to higher concentration. Diffusion ceases when the chemical potential for all the components in an alloy is same everywhere. However, since concentration gradients are much easier to measure, and uphill diffusion is less common, it is more convenient to express diffusion equations in terms of concentration gradients [43].

1.5.2   Kirkendall experiment and Darken's equations

In the case of single component systems, self-diffusion occurs even without the presence of a concentration gradient. This is because the atoms are in a constant state of vibration, and occassionally they can jump to nearby vacant sites (or interstitials) if they can overcome the energy barrier (more on this in next chapter) [44]. This also means that there

is only one diffusion coefficient called the self-diffusion coefficient. However, in the case of substitutional alloys, atoms of different metals diffuse at different rates, known as their intrinsic diffusivities and this was first established by Kirkendall and Smigelskas through their interdiffusion experiments [45]. They conducted experiments on diffusion couples made of pure Cu and α-brass (Cu - 30 wt.% Zn) and placed insoluble Mo markers at the interface, as shown in Figure (1.13). The experiment was carried out at a temperature where the interdiffusion of Cu and Zn was possible. It was observed that the marker plane shifted towards α-brass in reference to the boundary plane at the end of the diffusion experiment [45]. This was because Zn diffuses faster from α-brass to Cu , than Cu diffuses into α-brass. Indeed, this phenomenon was observed for a number of other metals and alloys. The unequal diffusion of the two metals also established that substitutional diffusion occurs by a vacancy mechanism. Infact, the flux of the vacancies in a diffusion couple is opposite to the net flux of the atoms. In the case of Cu and α-brass, the Cu side has an excess of vacancies, while the α-brass side is deplete of vacancies. The presence of jogged edge dislocations can act as vacancy sources/sinks in order to maintain an equilibrium number of vacancies on either side [43]. Absorption of vacancies by the extra half plane of atoms in the α-brass side would cause the shrinking and the eventual annihilation of the dislocation, while emission of vacancies (or the absorption of atoms) by the dislocations on the Cu side would ultimately introduce extra lattice planes. Thus, in the presence of a concentration gradient in substitutional alloys, a rigid shift is to be expected in the lattice frame relative to the laboratory frame [46]. This is observed macroscopically by the shift of the marker plane towards the α-brass side.

Darken published detailed mathematical analysis on the Kirkendall's experiments for binary substitutional alloys[43]. The total number of atoms per unit volume is assumed to be a constant irrespective of the composition. His first equation calculates the velocity of the marker plane, v to be [43]

$$v = (D_{\mathrm{A}} - D_{\mathrm{B}})\frac{\partial X_{\mathrm{A}}}{\partial x} \tag{1.5}$$

where D_A and D_B are the intrinsic diffusivities of the two metals and X_A is the mol-fraction of metal A. His second equation defines a combined chemical diffusion coefficient called the interdiffusion coefficient, $\tilde{D}$ and is related to the intrinsic diffusivities as [43],

$$\tilde{D} = X_B D_A + X_A D_B \tag{1.6}$$

where X_A and X_B are the mol-fractions of A and B respectively. The interdiffusion coefficient, $\tilde{D}$ should be used in Equation (1.4) in the case of binary substitutional alloys. In the case of a dilute alloy of B in A, this equation simply reduces to,

$$\tilde{D} \approx D_B \tag{1.7}$$

1.5.3 Tracer diffusion coefficients and thermodynamic factor

Radioactive tracers are used to experimentally measure the self-diffusion coefficients of metals, since they are chemically identical to the metals. Small quantities of radioactive isotopes are deposited on the metals, and after annealing at a fixed temperature, the diffusivities measured by solving for the Equation (1.4). In an alloy, the tracer diffusivity D_B^* can be measured in a similar way, and it gives the rate at which B atoms diffuse in a chemically homogeneous alloy, while the intrinsic diffusivity D_B gives the rate at which the B atoms would diffuse when a concentration gradient is present. The intrinsic diffusivity D_B can be related to the tracer diffusivity D_B^* by the following relationship [44],

$$D_B = \phi D_B^* \tag{1.8}$$

where ϕ is known as the thermodynamic factor and is given as [44],

$$\phi = 1 + \frac{d \ln \gamma_A}{d \ln X_A} = 1 + \frac{d \ln \gamma_B}{d \ln X_B} = \frac{X_A X_B}{RT} \frac{d^2 G}{dX^2} \tag{1.9}$$

where γ_A and γ_B are the activity coefficients of A and B respectively, while G is the

free energy. The last equality follows from the Gibbs-Duhem equation [45]. For an ideal or a dilute solution, ϕ becomes unity, and hence the tracer diffusivity is the same as the intrinsic diffusivity [44]. This is very convenient as the calculations described in the present investigation calculate the tracer diffusion coefficients in the absence of any concentration gradient. Only in the case of non-dilute solutions, the tracer diffusion coefficients do not represent the intrinsic diffusion coefficients [44]. Also, vacancy concentration in metals is low even at high temperatures, and hence vacancies always form a dilute solution in alloys. Thus, it follows that consideration of the thermodynamic factor is not necessary for the calculation of vacancy diffusion coefficients.

For further reading on diffusion in binary and multicomponent substitutional alloys, one is advised to read the work of Van der Ven et al [47] and the references therein.

1.6 Diffusion data in Ni-based superalloys

Experimental measurements of self-diffusion and solute diffusion coefficients have been carried out in Ni and its alloys by a variety of experimental techniques. For a precise measurement of diffusion coefficients it is desirable to conduct a single investigation over a wide range of temperature [50]. In the case of self-diffusion of Ni, the most important ones are the works of Bakker et al [49] and Maier et al [48] carried out on single crystal Ni samples over a wide range of temperature in the high temperature regime and low temperature regime respectively (Figure 1.14). Other important works measuring one or more parameters in the self-diffusion coefficients of Ni are also available in the literature, the values of which have been compared to the results from the present work in Table 4.3.

Karunaratne et al [37] have calculated interdiffusion coefficients in binary alloys of Re, W and Ta in Ni within dilute regime using the Boltzmann-Matano analysis, where they found that these coefficients were almost independent of the concentration (Figure 1.15). Ta was found to be the fastest diffuser of the three, while Re was the slowest, being almost two orders of magnitude lower than that of Ta. The interdiffusion coefficient of W lied
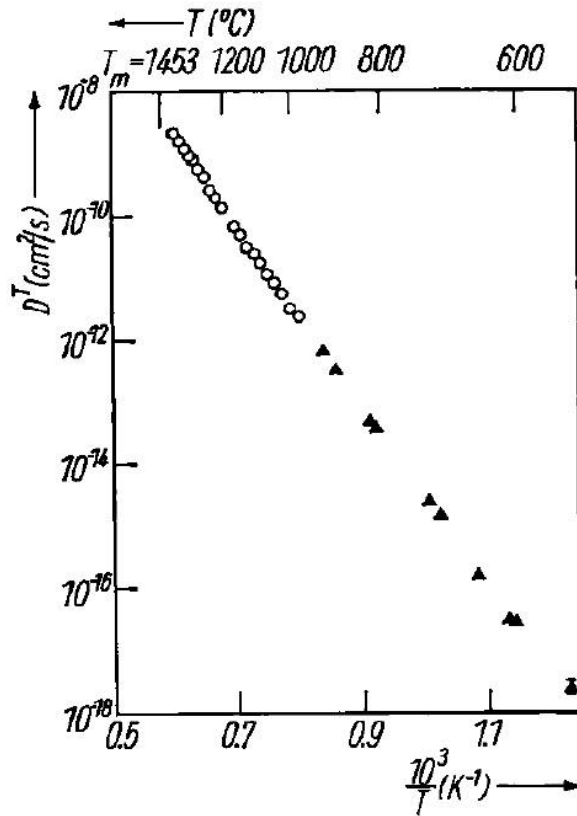
Figure 1.14: Arrhenius plot of self diffusion coefficient of Ni in single crystals from low [48] to high temperatures [49].
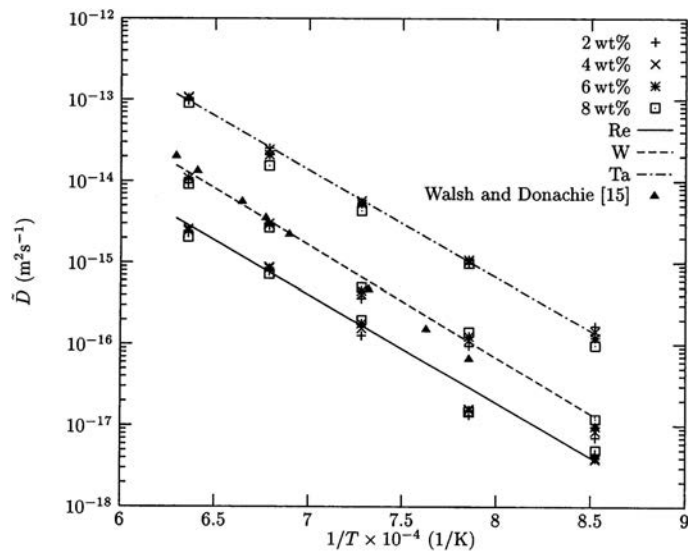
Figure 1.15: Interdiffusion coefficients in the γ phases of Ni-Ta, Ni-W and Ni-Re systems [37].

almost midway between Ta and Re. They attributed the difference in the interdiffusion coefficients of Re, W and Ta in Ni to their diffusion pre-factors, while the derived activation energies were very similar (see Equation (2.1) for definitions of diffusion pre-factors and activation energies).

This however, is in stark contrast to the results obtained by Janotti et al [36] from *ab initio* methods. They have systematically calculated the diffusion coefficients of transition metal solutes in Ni (Figure 1.16a), observing a similar trend as Karunaratne et al [37]. However, they found that the activation energy barriers vary significantly amongst different solutes in Ni (Figure 1.16b). Re (Atomic Number 75) was found to have the highest activation energy barrier amongst all the solutes. This was also confirmed from other *ab initio* works ([51], [52]). The experimental values for diffusion pre-factors and activation energies are commonly obtained by fitting the diffusion data to the Arrhenius relationship, and hence are prone to inconsistencies especially if the investigated temperature range is small. On the other hand, these parameters are calculated directly in *ab initio* methods. As a result, the experimental values may not be necessarily expected to match the pre-factor and activation energy values obtained from *ab initio* methods.

Schuwalow et al [52] have calculated the vacancy diffusion coefficients for solutes in Ni within dilute limits using a combination of *ab initio* calculations and kinetic Monte Carlo simulations. Only one solute atom was considered in the simulation in the dilute limit and vacancy jump barriers around it were accurately calculated. This eliminated the possibility of any solute-solute interactions. The solute concentration was varied by changing the size of the simulation cell, and the maximum possible solute concentration was approximately 3 wt.% (about 0.9 at.%). The results showed a minimal influence of the presence of solutes on vacancy diffusion, with a 3 wt.% Re addition slowing down the vacancy diffusion by about 5% (Figure 1.17). They concluded that within the dilute limits, interactions between the vacancies and solute atoms were too weak to have a net effect at the relevant temperatures, but also suggested that consideration of solute-solute interactions were necessary to account for the local fluctuations in solute concentration,
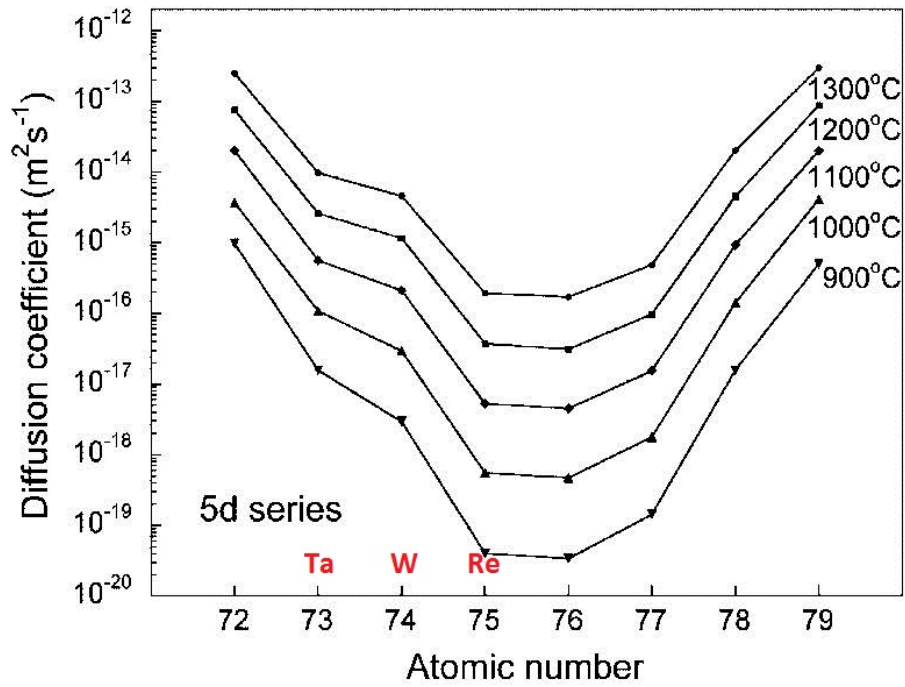
(a) Calculated diffusion coefficients for the 5d transition metals in Ni [36]
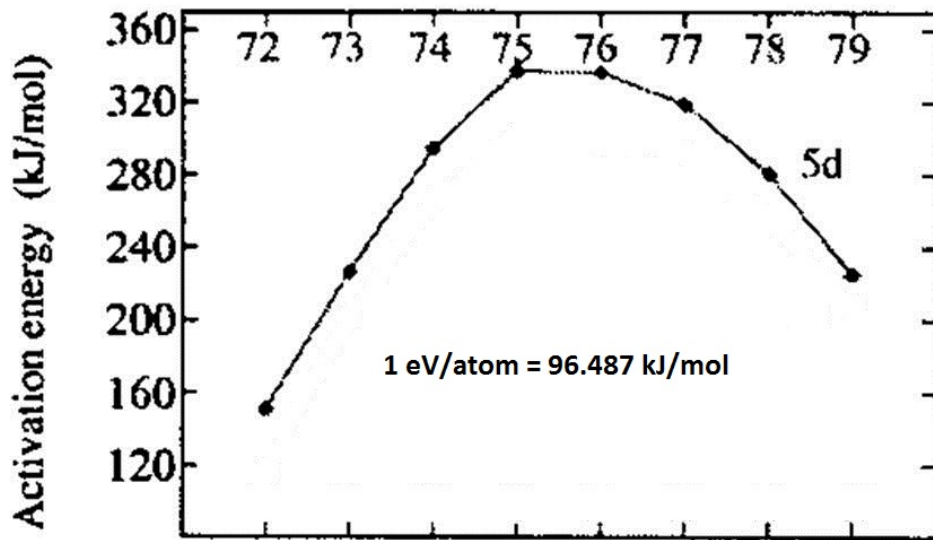
(b) Calculated activation energy barriers for the 5d transition metals in Ni [36]

Figure 1.16: Results from *ab initio* calculations of Janotti et al [36]
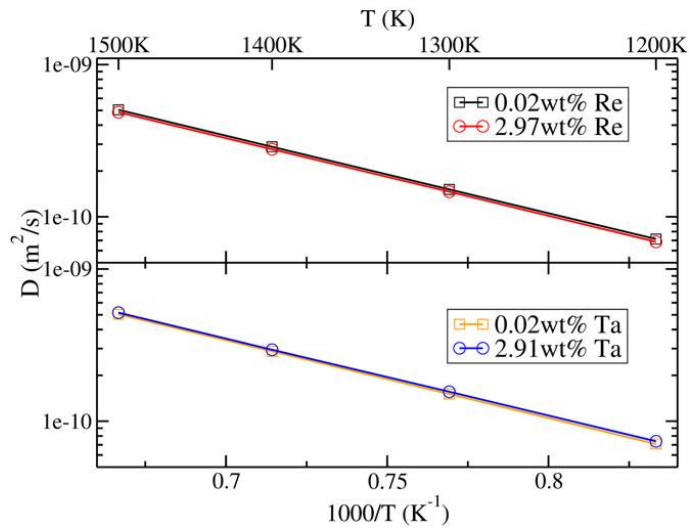
Figure 1.17: Vacancy diffusion coefficients for different concentrations of Re and Ta in Ni as calculated by Schuwalow et al [52]

especially given the partitioning behaviour of solutes within the γ-γ' structure.

CHAPTER 2

MODELLING DIFFUSION

The diffusion coefficient or diffusivity D is a phenomenological constant as defined from Fick's laws and is experimentally seen to follow the Arrhenius relationship,

$$D = D_0 \exp\left\{-\frac{Q}{k_{\mathrm{B}}T}\right\} \tag{2.1}$$

where D_0 and Q are the diffusion pre-factor and activation energy respectively, k_{B} is the Boltzmann constant and T is the absolute temperature.

However, diffusion is a stochastic process when looked at from an atomic level compared to a deterministic process in a continuum medium. Random walk experiments are developed to understand diffusion as an atomic scale process. For a sufficiently large number of independent random step sequences, the most probable or the root mean square displacement of an atom for a random walk in any dimension is given as [53],

$$< |L|^2 >^{1/2} = \sqrt{n}\lambda \tag{2.2}$$

where n is the number of steps and λ is the step length or the microscopic jump distance. For the continuum case, considering the example of the release of a cloud of diffusant particles from the origin, the most probable displacement as a function of time t is given by [53],

$$< R^2 >^{1/2}= \sqrt{6Dt} \tag{2.3}$$

where D is the diffusion coefficient. If the time t in Equation (2.3) is associated with the time required to execute n steps in Equation (2.2), we have,

$$D = \frac{1}{6}(\frac{n}{t})\lambda^2 \tag{2.4}$$

Here, n/t is the step rate equivalent to the atomic jumping frequency, Γ. Thus, we arrive at the Einstein's formula [53],

$$D = \frac{1}{6}\Gamma\lambda^2 \tag{2.5}$$

Thus, diffusion coefficient can be theoretically expressed in terms of microscopic parameters from solid-state principles [53]. The activation energy (Q_i) and pre-factor ($D_{0,i}$) in Equation (2.1) can be expressed analytically using formulations as described later in this chapter.

2.1   Modelling diffusion in dilute alloys

Analytical formulations are well established for the calculation of diffusion coefficients in the dilute regime. The assumption is that the solute concentration is small such that the solute atoms are always surrounded by the solvent (Ni) atoms and two solute atoms don't interact with each other in any way.

2.1.1   Calculation of self-diffusion and solute diffusion coefficients

In substitutional solid solutions, vacancy assisted diffusion is the dominant mechanism for the movement of atoms which requires exchange of a vacancy with one of its nearest neighbour atoms(see Figure 2.1). The solute diffusion coefficient (D_i) for a solute i in
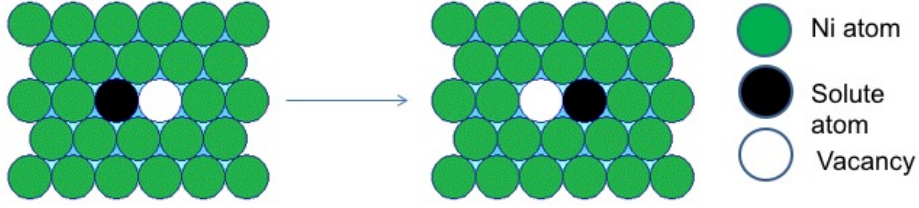
Figure 2.1: Vacancy assisted diffusion in a dilute *fcc* alloy

dilute binary alloys of Ni with *fcc* crystal structure is given by [54]

$$D_i = a^2 x_{\mathrm{v},i} \Gamma_i f_i \tag{2.6}$$

where a is the equilibrium Ni lattice parameter, $x_{\mathrm{v},i}$ is the probability of vacancy occurring beside an atom i, Γ_i is the solute-□ (vacancy) exchange frequency and f_i is the solute correlation factor. For self-diffusion, the Ni atom itself is the solute.

Vacancy formation

Since solute diffusion is mediated by vacancies, the solute atom has to have a vacant site in its 1st nearest neighbour (1NN) position to undergo a diffusion jump. The probability of a vacancy occurring beside an atom i is

$$x_{\mathrm{v},i} = \exp\left(\frac{\Delta S_{\mathrm{f}}^{\mathrm{vib}}}{k_{\mathrm{B}}}\right) \exp\left(-\frac{\Delta E_{\mathrm{f},i}}{k_{\mathrm{B}}T}\right) \tag{2.7}$$

where $\Delta E_{\mathrm{f},i}$ is the vacancy formation energy adjacent to a solute and $\Delta S_{\mathrm{f}}^{\mathrm{vib}}$ is the vibrational entropy of vacancy formation. $\Delta S_{\mathrm{f}}^{\mathrm{vib}}$ has been calculated previously but results from different theoretical approaches differ significantly [51]. We have assumed $\Delta S_{\mathrm{f}}^{\mathrm{vib}} = 1.4 k_{\mathrm{B}}$, computing an average of two values reported by Seeger et al [55] calculated by fitting the experimental Ni-self diffusion data. $\Delta E_{\mathrm{f},i}$ is given by,

$$\Delta E_{\mathrm{f},i} = \Delta E_{\mathrm{f,Ni}} - E_{\mathrm{bind}}^{\mathrm{1NN}} \tag{2.8}$$

where $\Delta E_{\mathrm{f,Ni}}$ is the vacancy formation energy in pure Ni. This is calculated from

$$\Delta E_{\mathrm{f,Ni}} = E(\mathrm{Ni}_{N-1}\square) - \frac{N-1}{N}E(\mathrm{Ni}_N) \tag{2.9}$$

where $E(\mathrm{Ni}_N)$ represents the total energy of a perfect supercell of Ni atoms and $E(\mathrm{Ni}_{N-1}\square)$ represents the energy when one of the atoms is replaced by a vacancy. N is the number of atoms used in the energy calculations. $E_{\mathrm{bind}}^{\mathrm{1NN}}$ is the binding energy for a solute i and a vacancy at 1st nearest neighbour position to each other while being surrounded by Ni atoms. This is given by[29],

$$E_{\mathrm{bind}}^{\mathrm{1NN}} = E(\mathrm{Ni}_{N-1}i) + E(\mathrm{Ni}_{N-1}\square) - E(\mathrm{Ni}_{N-2}(i-\square)^{\mathrm{1NN}}) - E(\mathrm{Ni}_N) \tag{2.10}$$

where $E(\mathrm{Ni}_{N-1}i)$ represents the total energy of the supercell with a single solute atom i, and $E(\mathrm{Ni}_{N-2}(i-\square)^{\mathrm{1NN}})$ represents the the total energy of the supercell with the solute atom and a vacancy at 1st nearest neighbour position to each other.

Jump frequency

The jump frequency for a successful atom-$\square$ exchange is defined as [56]

$$\Gamma_i = \nu_i^* \exp\left\{-\frac{\Delta E_{\mathrm{m},i}}{k_{\mathrm{B}}T}\right\} \tag{2.11}$$

where ν_i^* is the effective frequency associated with the vibration of the atom in the direction of the vacancy [56] and $\Delta E_{\mathrm{m},i}$ is the migration energy. For a successful atom-vacancy exchange to take place, the atom has to push through a window of other atoms in the vicinity, which requires local distortion of the lattice (see Figure (2.2)). The activation energy associated with this process is known as the migration energy. It is the difference between the energy at the saddle point (activated state) and the starting point of the transition.

Within harmonic transition state theory, the effective frequency ν^* is given as the
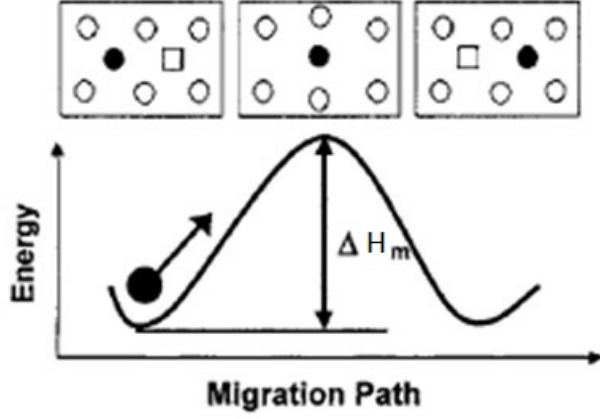
Figure 2.2: The atom-vacancy exchange showing an migration energy barrier

ratio of the product of $3N$ normal frequencies at the starting point of the transition to the $3N$-1 normal frequencies of the state constrained at the saddle point configuration, N being the number of atoms in the system [56, 57],

$$\nu^* = \frac{\displaystyle\prod_{j=1}^{3N} \nu_j}{\displaystyle\prod_{j=1}^{3N-1} \nu_j'} \qquad (2.12)$$

Each atom has 3 degrees of freedom and is associated with 3 normal frequencies. So, the entire crystal has $3N$ degrees of freedom x_1, x_2,..,x_{3N}. These normal frequencies are calculated from the second derivative matrix of energy or the force constant matrix β. β is a $3N \times 3N$ symmetric matrix (and hence is diagonalizable) whose ij^{th} element is given as[56],

$$\beta_{ij} = \frac{\partial^2 E}{\partial x_i \partial x_j} \qquad (2.13)$$

Under harmonic approximation, the normal frequencies are the roots of the characteristic equation[56] given as,

$$\det[X - (2\pi\nu)^2 I] = 0 \qquad (2.14)$$

where, I is the unit matrix and the ij^{th} element of X is $\beta_{ij}/\sqrt{m_i m_j}$ where m_i and m_j are

31
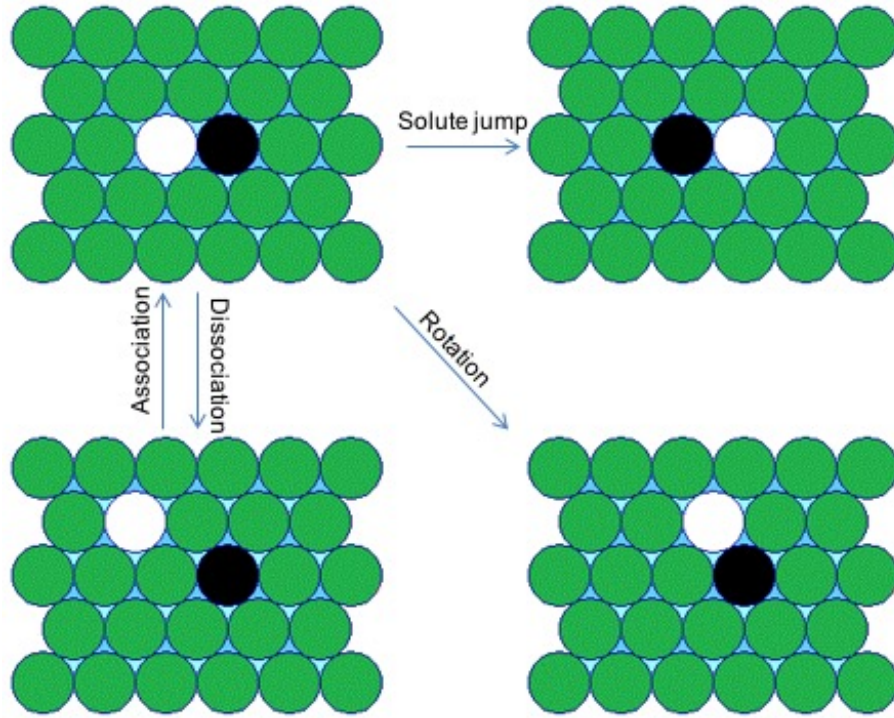
Figure 2.3: Various diffusion jumps in a dilute *fcc* alloy causing a vacancy-solute exchange, rotation and dissociation/association

the masses associated with the degrees of freedom x_i and x_j respectively.

Correlation factor

Correlation effects develop in a system as the atoms do not undergo a strict 'random walk'. The correlation factor f_i gives a measure of this reduced efficiency of diffusion. For self-diffusion in *fcc* crystals, a value of 0.78146 has been accurately determined using computer simulations [58]. In dilute binary *fcc* alloys, several different jumps are possible and f_i is estimated using Lidiard's model [59, 60, 61, 62]

$$f_i = \frac{2\Gamma_{\text{rot}} + 7\Gamma_{\text{dis}}}{2\Gamma_{\text{rot}} + 2\Gamma_i + 7\Gamma_{\text{dis}}} \tag{2.15}$$

where Γ_{rot} and Γ_{dis} are jump frequencies for the rotation and dissociation of the solute-□ pair respectively, and Γ_i is the solute-□ exchange frequency (see Figure 2.3).

Comparing the above Equations (2.6 - 2.15) with Equation (2.1), we can write

$$D_{0,i} = f_i a^2 \nu_i^* \exp \left\{ \frac{\Delta S_{\mathrm{f}}^{\mathrm{vib}}}{k_{\mathrm{B}}} \right\} \qquad (2.16)$$

$$Q_i = \Delta E_{\mathrm{f},i} + \Delta E_{\mathrm{m},i} \qquad (2.17)$$

. The values for the pre-factor ($D_{0,i}$) and exponential terms (Q_i) can be experimentally determined from the slope and intercept of a graph of the logarithm of diffusivity versus the inverse of temperature. These are commonly known as Arrhenius plots. Both $D_{0,i}$ and Q_i are assumed to be temperature independent. But while $D_{0,i}$ only affects the diffusivity linearly, Q_i has a much pronounced effect and thus even a small change in Q_i can have a big impact on diffusivity. It should be pointed out, however, that f_i is not strictly temperature independent, as it is in turn dependent on the values of Γ_i, Γ_{dis} and Γ_{rot} which are temperature dependent. However, variation of f_i with temperature is small in most cases [63].

2.1.2 Calculation of vacancy diffusion coefficients

In the case of pure metals, one can calculate the vacancy diffusion coefficients by dividing the self-diffusion coefficients by the equilibrium vacancy concentration at the same temperature. However, in the case of alloys, the direct determination of vacancy diffusion coefficients is less obvious using analytical formulations as other contributions come in. Manning's random alloy model [64] is the only available approximate method in the literature to our best knowledge. This model applies to alloys where the atoms and vacancies are distributed randomly with no energetically favoured sites. Using this model, the vacancy diffusion coefficient, D_{v} is given by

$$D_{\mathrm{v}} = a^2 \Gamma_{\mathrm{v}} f_{\mathrm{v}} \qquad (2.18)$$

where Γ_v is the average vacancy jump frequency and f_v is the vacancy correlation factor. The jump frequency of a vacancy is the same as the jump frequency of the atom exchanging with the vacancy. In a binary alloy, Γ_v can be approximated by a simple arithmetic average of the jump frequencies weighted by their respective atomic concentration,

$$\Gamma_\text{v} = x_i \Gamma_\text{i} + x_\text{Ni} \Gamma_\text{Ni} \tag{2.19}$$

This approach assumes that the jump frequency of a given atom i, Γ_i, depends only on i and not on the identity of other neighbouring atoms, and that the lattice site occupation surrounding a vacancy is not biased relative to the average composition of the binary alloy.

The vacancy follows a random walk in a pure crystal as all the vacancy jumps are equally probable and hence f_v is unity for the self-diffusion case. In a random alloy of Ni where x_i is the mole-fraction of solute i, f_v is given by [64]

$$f_\text{v} = \frac{x_i \Gamma_\text{i} f_\text{v}^i + x_\text{Ni} \Gamma_\text{Ni} f_\text{v}^\text{Ni}}{x_i \Gamma_\text{i} + x_\text{Ni} \Gamma_\text{Ni}} \tag{2.20}$$

where f_v^i is the partial vacancy correlation factor for i. Since the correlation effect for each component can differ, a partial vacancy correlation factor, f_v^i is defined for each individual component i. The partial vacancy correlation factor, f_v^i is related to the solute correlation factor, f_i by equating the vacancy flux, J_v to the sum of the atom fluxes J_i [64],

$$J_\text{v} = \sum_i J_i \tag{2.21}$$

The partial vacancy correlation factor, f_v^i enters into the direct calculation of J_v considering vacancy drift velocities, while the solute correlation factor, f_i enters into the calculation of J_i. Finally, f_v^i has been derived as [64]

$$f_v^i = \frac{f_i}{f_0} \tag{2.22}$$

where f_0 is the correlation factor for self-diffusion in *fcc* crystals and is equal to 0.78146 [58]. For a detailed derivation of the Equation (2.22), one must refer to Manning's work [64]. Further, the general expression for the solute correlation factor, f_i in any crystal system with sufficient symmetry is given as [65],

$$f_i = \frac{H_i}{2\Gamma_i + H_i} \tag{2.23}$$

where H_i is the effective escape frequency for the vacancies next to an atom of the component i and determines whether a vacancy would undergo a subsequent reverse exchange after a successful exchange with the atom i has taken place, thus introducing a correlation effect. For the case of an *fcc* Ni crystal, Equation (2.23) simplifies to [64],

$$f_0 = \frac{H_0}{2\Gamma_{\mathrm{Ni}} + H_0} \tag{2.24}$$

Since f_0 is a constant for pure *fcc* Ni crystals, this follows that the escape frequency H_0 would be directly proportional to Γ_{Ni},

$$H_0 = M_0 \Gamma_{\mathrm{Ni}} \tag{2.25}$$

where M_0 is a numerical constant. Substituting the value of H_0 from Equation (2.25) into Equation (2.24), M_0 is given as,

$$M_0 = \frac{2f_0}{1 - f_0} \tag{2.26}$$

Using a value of 0.78146 for f_0 [58], a M_0 value of 7.15 is obtained for *fcc* crystals. Again, the relationship between the escape frequency H_i in a random alloy and H_0 can be approximated as [64]

$$H_i = f_\text{v} H_0 \tag{2.27}$$

This is because the vacancy correlation is expected to affect the escape frequencies in the same proportion as the vacancy diffusion rates. Substituting Equation (2.27) in Equation (2.23), we get

$$f_i = \frac{f_\text{v} H_0}{2\Gamma_\text{i} + f_\text{v} H_0} \tag{2.28}$$

Substituting Equation (2.20) and Equation (2.22) for f_v and f_v^i, Equation (2.25) for H_0 and Equation (2.6) for D_i, the solute correlation factor, f_i for a random alloy can be derived as [64],

$$f_i = 1 - \frac{2D_i}{(M_0 + 2)(x_\text{Ni} D_\text{Ni} + x_i D_i)} \tag{2.29}$$

and the vacancy correlation factor, f_v for a random alloy can be derived as [64],

$$f_\text{v} = 1 - \frac{2}{M_0} \frac{(M_0 + 2)x_\text{Ni} x_i (D_\text{Ni} - D_i)^2}{(M_0 + 2)(x_\text{Ni} D_\text{Ni} + x_i D_i)^2 - 2D_\text{Ni} D_i} \tag{2.30}$$

Note that the Manning's random alloy model breaks down for dilute levels of solute atoms which diffuse faster than the solvent, and we get negative values for the correlation factors. This is because of the use of the various approximations in the model. Hence, for these solutes, we have alternatively calculated f_v from Equation (2.20), using Equation (2.22) for f_v^i. To a first approximation, the partial vacancy correlation factor for Ni, f_v^{Ni} is taken as unity for the case of dilute alloys.

2.2 Kinetic Monte Carlo simulations

Computer simulations are widely used to model materials at the atomic level. The modelled systems may contain up to many thousands of atoms, and hence it is possible to sample a wide configurational space. The exact positions of the atoms are tracked and

a statistical analysis of the trajectory can be used to predict material properties. Two general classes of simulations are the molecular dynamics (MD) and the Monte Carlo (MC) simulations.

In a MD simulation [66, 67] , the trajectories of atoms and molecules are determined by numerically solving Newton's equations of motion for a system of interacting particles, where forces between the particles are extracted from the corresponding potential energy surface. This is a deterministic approach to model the evolution of the system. On the other hand, MC methods [68] sample the configurational space of a system in a stochastic manner. These methods can be used, for *e.g.* to arrive at the thermodynamically most stable configuration for any given condition. However, the sequence of the generated configurations are not representative of the real-time evolution of the system.

Kinetic Monte Carlo (kMC) methods, however simulate the dynamical evolution of a system where the simulation time is related to the real time [69]. However, unlike MD simulations, only the state-to-state transitions are treated while the atomic vibrations about their equilibrium positions are suitably averaged. These state-to-state transitions are *rare events* as compared to the atomic vibrations, and the system spends a considerable amount of time in one state, before a successful transition to another state takes place [70]. This relative inactivity over long periods of time means the system loses its memory of how it got there. These sequence of states thus follow a Markov chain [71]. The probability of moving from a state σ' to another state σ is independent of the state that preceded σ'. The time evolution of this probability is given by the Master equation [72, 73],

$$\frac{\partial P(\sigma, t)}{\partial t} = \sum_{\sigma'} W(\sigma' \to \sigma) P(\sigma', t) - \sum_{\sigma'} W(\sigma \to \sigma') P(\sigma, t) \tag{2.31}$$

where σ' and σ are successive states of the system, $P(\sigma, t)$ is the probability that the system is in the state σ at time t, and $W(\sigma' \to \sigma)$ is the probability per unit time that the system will undergo a transition from state σ' to state σ. The kMC methods provide numerical solution to the master equation (Equation 2.31). At equilibrium, the time derivative in the master equation becomes zero, and the sum of all transitions from
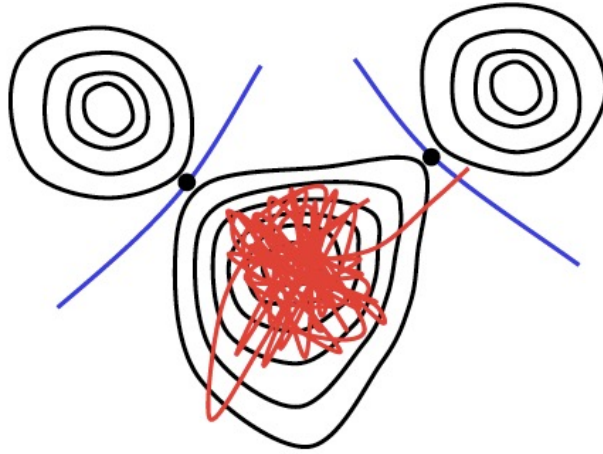
Figure 2.4: Contour plot showing an atom vibrating at its equilibrium position, and a rare diffusive jump by surmounting of the energy barrier [70]

σ' to σ equals the sum of all transitions from σ to σ' [72, 73],

$$W(\sigma' \to \sigma)P_{eq}(\sigma') = W(\sigma \to \sigma')P_{eq}(\sigma) \qquad (2.32)$$

where P_{eq} denotes the equilibrium probability. This is called the detailed-balanced criterion [72, 73], and this needs to be fulfilled for the system to attain thermal equilibrium.

Diffusive exchange between an atom and a vacancy is a typical example of a *rare event*. At a finite temperature, the atoms vibrate about their mean positions (typically once every 10^{-12} s) [69]. Occasionally an atom surrounding a vacancy can surmount the energy barrier and exchange its position with a vacancy (see Figure 2.4). However these diffusion jumps are rare, and happen on a higher time scale (typically $\approx 10^{-6}$ s) [69]. An accurate integration in an MD simulation would require time steps short enough to resolve atomic vibrations and hence the total simulation time is restricted. Thus, it is computationally unfeasible to study the problem of diffusion using MD simulations. This problem is solved using the kMC method, as it concentrates only on the *rare event* of diffusion. Thus, much larger time scales can be reached in a kMC simulation when compared to the MD simulations.

The algorithm for a kMC simulation to calculate the diffusion coefficients is as follows [74] :

1. Set up the *fcc* lattice and populate it with atoms leaving one site empty representing a vacancy. Fix the temperature at the desired value T and set time $t=0$.

2. Calculate all the jump frequencies $\Gamma_1, \Gamma_2, ..., \Gamma_{12}$ (see Equation (2.11)) corresponding to the possible vacancy jumps at this state. In an *fcc* crystal, a vacancy can exchange its position with atoms on its 12 nearest neighbour sites. Hence, the number of possible vacancy jumps is 12 at each state.

3. Calculate the cumulative sum $\Gamma^i = \sum_{j=1}^{i} \Gamma_j$ for each vacancy jump $i = 1, 2, ..., 12$.

4. Generate a uniform random number $\rho_1 \in (0,1]$.

5. Find the vacancy jump to carry out by finding the i for which
$\Gamma^{i-1} < \rho_1 \Gamma^{12} \leq \Gamma^i$.

6. Carry out the vacancy jump i.

7. Generate another uniform random number $\rho_2 \in (0,1]$.

8. Update time $t = t + \Delta t$ where $\Delta t = -\dfrac{\ln \rho_2}{\Gamma^{12}}$. This is because the kMC algorithm simulates a Poisson process, and a relationship with the real time can thus be established [73].

9. The system has moved to a new state after the vacancy jump. Repeat steps 2 through 8 for the desired number of vacancy jumps.

10. Track the atoms and the vacancy coordinates throughout the simulation. At the end of the desired number of vacancy jumps, calculate the vacancy diffusion coefficient D_{v} for a single vacancy using

$$D_{\mathrm{v}} = \frac{1}{6} \frac{\partial}{\partial t} \left\langle R_{\mathrm{v}}^2(t) \right\rangle \tag{2.33}$$

and the solute diffusion coefficient using

$$D_i = \frac{x_{\mathrm{v}}}{x_{\mathrm{v}}^{sim}} \times \frac{1}{6N} \frac{\partial}{\partial t} \sum_{i=1}^{N} \left\langle \left[R_i^2(t) \right] \right\rangle \tag{2.34}$$

where $\langle R^2(t) \rangle$ is the mean square displacement of the vacancy (or solute atoms) from the initial state, N is the number of i atoms and t is the time elapsed. x_{v} is the actual vacancy concentration at temperature $= T$ (see Equation (2.7)), while x_v^{sim} is the vacancy concentration used in the kMC simulation. $R^2(t)$ is calculated as

$$R^2(t) = |x(t) - x(0)|^2 + |y(t) - y(0)|^2 + |z(t) - z(0)|^2 \tag{2.35}$$

where the values on the right represent the coordinates of the vacancy(or solute atoms) at time $= t$ and time $= 0$.

The kMC simulation should be run for a sufficiently large number of steps such that the D values converge. To obtain better statistics, the kMC trajectory can be divided over a number of segments and D can be calculated from the time-weighted averages of the diffusion coefficients calculated from the various segments [52, 75].

2.3 Modelling diffusion in non-dilute alloys

Analytical methods for the rigorous calculation of diffusion coefficients in non-dilute alloys cannot be formulated given the complexity of the problem, however some approximate models do exist in the literature [51, 76, 77, 78] . For the case of dilute alloys, only a few activation energy barriers are needed to describe the system. However in the case of non-dilute alloys, atoms can be arranged in a number of configurations. This means a number of activation energy barriers corresponding to these atomic configurations need to be calculated, which is difficult. Further, to calculate these energy barriers, one needs to calculate both the energy of the activated state and the energy of the end states. This problem is made simpler by using the cluster expansion method which is described below. We have dealt with the binary Ni-Re system in the non-dilute regime.
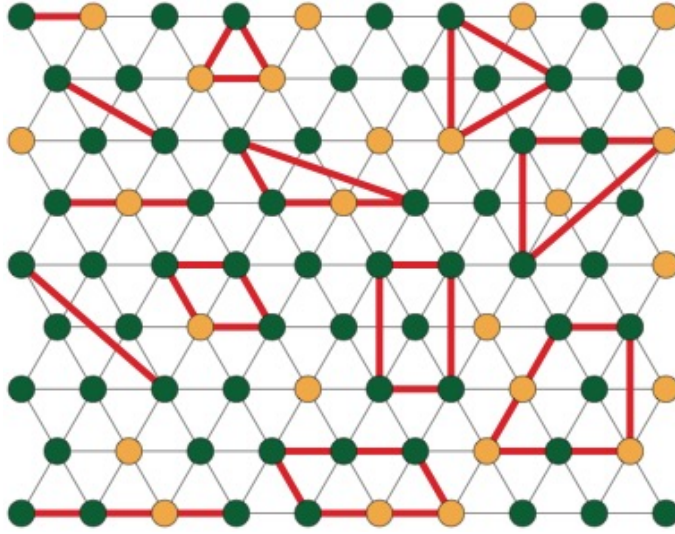
Figure 2.5: A 2D lattice showing some possible clusters

2.3.1 Cluster expansion method

The cluster expansion can be seen as a generalised Ising Model [79] . The lattice of a binary alloy such as Ni-Re can be represented using occupation variables (σ_i) [80, 81, 82]. A value of +1 represents a Ni atom, while -1 represents a Re atom. The vector of the occupation variables $\vec{\sigma}$ would then uniquely describe the configuration of the system. The energy of the alloy E for a configuration $\vec{\sigma}$ can be expanded using polynomials ϕ_α of (σ_i)

$$E(\vec{\sigma}) = V_0 + \sum_\alpha V_\alpha \phi_\alpha(\vec{\sigma}) \tag{2.36}$$

where ϕ_α is simply the product of occupation variables belonging to a particular cluster of sites α , *i.e.* $\phi_\alpha = \prod_{i \in \alpha} \sigma_i$. These clusters could be point clusters, pairs, triplets, quadruplets... etc (see Figure 2.5). The expansion of this equation to an infinite number of clusters theoretically should describe the energy exactly. However, the expansion is usually truncated up to a few clusters which can describe the energy to a reasonable precision. V_α are the Effective Cluster Interaction (ECI) coefficients and are calculated by fitting energy calculated from first principles (see Chapter 3) for a number of configurations [83]. Thus, from a relatively small first principles dataset, the energy for any given configuration can be cluster expanded using this technique.
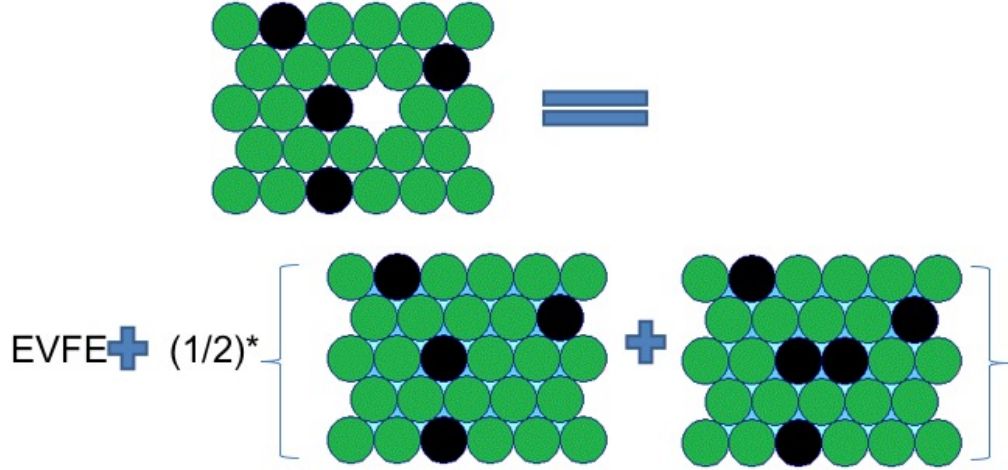
Figure 2.6: The physical representation of the effective vacancy formation energy

Description of the effective vacancy formation energy

Since the diffusion process is mediated by vacancies, we have to include vacancies in our simulation. A Cluster Expansion is needed to account for the energy difference owing to the inroduction of a vacancy into the binary alloy. The concentration of vacancies in an alloy is small even at high temperatures, hence it can be assumed that vacancies do not interact with one another. Thus, instead of treating the problem as a ternary one, vacancies can be treated as a perturbation to the binary cluster expansion.

In a pure system, the vacancy formation energy can be defined. However, in a binary alloy one does not know if the solute or the solvent occupied the vacant site initially. So, we define an effective vacancy formation energy (EVFE) (see Figure 2.6) for a vacancy at site i as [84],

$$\Delta E_i^{\text{eff}} = E_i^{\text{v}}(\vec{\sigma}) - \frac{1}{2}\left[E_i^{\text{Ni}}(\vec{\sigma}) + E_i^{\text{Re}}(\vec{\sigma})\right] \tag{2.37}$$

This EVFE can be parametrised using a local cluster expansion using coefficients which only depend on the local Ni-Re configuration. It must be noted that EVFE, unlike the vacancy formation energy is not a physical quantity and it has only been defined in order to calculate the total energy for a configuration of atoms and a vacancy easily using the cluster expansion. $E_i^{\text{v}}(\vec{\sigma})$ is the desired energy of the alloy with a vacancy and is obtained

by rearranging Equation (2.37). $E_i^{\text{Ni}}(\vec{\sigma})$ and $E_i^{\text{Re}}(\vec{\sigma})$ are the energies when the vacancy is replaced by a Ni atom or a Re atom, and these can be calculated from the usual binary cluster expansion.

Calculation of kinetically resolved activation energy barriers

The activation energy barriers not only depend on the surrounding configuration, but also on the direction of the jump. Hence to get around this, kinetically resolved activation (KRA) barriers are defined as [85],

$$\Delta E_{\text{KRA}} = E_s - \frac{1}{2}\left(E_i + E_f\right) \qquad (2.38)$$

where E_s is the energy of the activated state (saddle point), while E_i and E_f are the energy of the initial state and the final state (2 end points) of the jump (see Figure 2.7). ΔE_{KRA} is thus independent of the direction of the hop, and can be cluster expanded locally using a formalism similar to EVFE,

$$\Delta E_{KRA} = K_0 + \sum_{\alpha} K_{\alpha}\phi_{\alpha} \qquad (2.39)$$

where K_{α} are Kinetic Effective Cluster Interaction coefficients (KECIs) to describe KRAs as a function of configuration. Once the KRAs and the energies of the end states are available, the activation energy barriers ΔE_a can be calculated as,

$$\Delta E_a = E_s - E_i = \Delta E_{KRA} + \frac{1}{2}\left(E_f - E_i\right) \qquad (2.40)$$

Thus the cluster expanded energy of the binary alloy, the EVFE and the KRAs together would describe the Ni-Re system completely. These numbers are then fed into the kMC simulation to calculate the vacancy diffusion coefficients in the non-dilute regime.
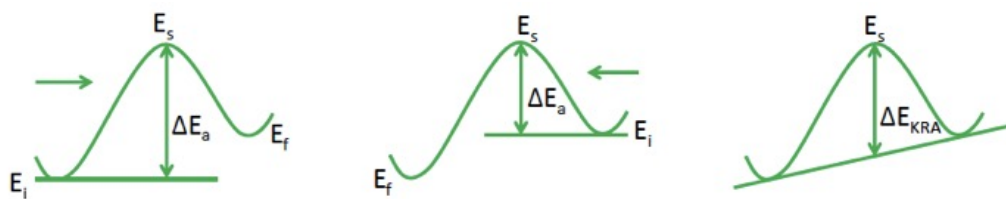
Figure 2.7: A schematic diagram illustrating the meaning of the kinetically resolved activation energy barriers

CHAPTER 3

COMPUTING ENERGIES

It follows from the previous chapter that diffusivity in dilute and non-dilute binary systems can be modelled using different methods, provided that the energetics of the system are known. Density functional theory (DFT) [86, 87] is currently the best technique to obtain the defect and migration energies required for this work accurately and within reasonable computational time. This chapter will cover some background of DFT, details of the calculations carried out, and methods used to calculate the migration barriers.

3.1 Density functional theory

DFT is often referred to as belonging to the group of first principles or *ab initio* techniques. *Ab initio* calculations are named so because they are completely based on quantum mechanical theoretical principles and use no input from experiments. In this context, DFT is a feasible approach to finding solutions to the Schrödinger equation, the fundamental equation that describes the quantum behaviour of atoms and molecules. Solving the Schrödinger equation for a complex system such as the ones treated within this work is computationally impossible, and DFT provides a way to make the problem tractable. In order to do this, DFT employs several approximations, which are described within this section.

The first approximation, which is common to many first-principles methods, separates

the description of the motion of the nuclei from the description of the motion of the electrons (the *Born−Oppenheimer* approximation) [88]. This approximation is applicable because of the large mass difference between the nuclei and the electrons. Due to this difference in mass, the nuclei move much slower than the electrons which means they can be considered stationary when solving the electronic part of the Schrödinger equation. As a result, the Schrödinger equation can be written as

$$\left[\frac{-\hbar^2}{2m} \sum_{i=1}^{N} \nabla_i^2 + \sum_{i=1}^{N} V(r_i) + \sum_{i=1}^{N} \sum_{j<i} U(r_i, r_j) \right] \psi = E\psi \tag{3.1}$$

where, the first term on the LHS represents the kinetic energy of each electron, the second term represents the interaction energy between each electron and the collection of nuclei, and the third term represents the interaction energy between different electrons. E is the ground state energy of the electrons and $\psi(r_1, r_2, ..., r_N)$ is the electronic wave function, where $r_1, r_2, ..., r_N$ are the spatial coordinates of each of the N electrons. Thus, solving for ψ becomes a many-body problem, as the individual wave function $\psi_i(r)$ cannot be determined without simultaneously considering the individual wave functions associated with all the other electrons and it becomes more and more difficult to solve the equation as the size of the system increases.

This is where the theorems formulated by Hohenberg and Kohn can help us find a solution to the many-body Schrödinger equation. The first theorem by Hohenberg and Kohn [86] states that the electronic ground state energy could be expressed as a functional of the electron density, $n(r)$. This can be summarised as

$$E = E[n(r)] \tag{3.2}$$

where,

$$n(r) = 2 \sum_i \psi_i^*(r)\psi_i(r) \tag{3.3}$$

The second theorem states that the electron density which minimises the energy func-

tional is the electron density that corresponds to the full solution of the Schrödinger equation.

Thanks to these two theorems, the problem of solving the many-body Schrödinger equation is reduced from one involving $3N$ variables (3 spatial variables for each of the electrons) to a problem of only 3 variables which define how the electron density changes in space. Yet, the problem still remains unsolvable as the form of the energy functional, $E[n(r)]$ is unknown. At this point, the Kohn-Sham ansatz [87] can be adopted to simplify the problem further. Kohn and Sham proposed that the energy functional for a system of interacting particles, which is unknown, can be written as the sum of the energy functional for a system of non-interacting particles and an exchange and correlation functional. Whereas the energy functional for a system of non-interacting particles is known (see later), the exchange and correlation functional is not.

This is where an additional approximation is required, and different approximations are available to obtain values for the exchange and correlation functional. The two most common approximations are the Local Density Approximation (LDA) and the Generalised Gradient Approximation (GGA). The LDA is the simplest approximation for E_{XC} which sets the exchange and correlation functional at a position with local density $n(r)$ to that for a uniform electron gas with the same electron density. The GGA for the exchange and correlation functional takes into account the local gradient of the electron density in addition to the local electron density. Both schemes to obtain the exchange and correlation functional rely on fitting the approximate functional to known data rather than finding the true form of the functional, which is why DFT using the local density or generalised gradient approximations for the exchange and correlation functional is not, strictly speaking, a first principles technique. Despite this, DFT is still an effective method to obtain accurate energies for a system of atoms.

Following from the above, the electron density of any system can be expressed in a way that involves solving a set of equations in which each of the equations only involves

47

a single electron [87].

$$\left[\frac{-\hbar^2}{2m}\nabla^2 + V(r) + V_{\mathrm{H}}(r) + V_{\mathrm{XC}}(r)\right]\psi_i(r) = \varepsilon_i\psi_i(r) \qquad (3.4)$$

In Equation (3.1), the potential V defines the interaction between an electron and the collection of atomic nuclei and V_{H}, or the Hartree potential, represents the Coulombic repulsion between the electron being considered and the net electron density [88]. This latter term also includes a self- interaction, as the electron being considered is also a part of the net electron density. This interaction is unphysical and the correction for it is one of the several effects which are lumped together in the potential term V_{XC}. V_{XC} can be formally expressed as a functional derivative of the exchange and correlation energy.

Now, to solve the Kohn-Sham equations, we need to define the Hartree potential, and to define the Hartree potential we need to know the electron density. But to find the electron density, we must know the single-electron wave functions, and to know these wave functions we must solve the Kohn-Sham equations. To break this circle, the problem is usually treated in an iterative way where an initial trial electron density is defined. Progressively, this trial density is updated until it matches the calculated electron density. Thus, this iterative method leads to a solution that is self-consistent.

The Kohn-Sham equations [87] can be solved using plane wave basis sets. However the disadvantage is that we require large number of plane waves to expand the wave functions in the core region, because the wave functions of the core electrons are highly localized and oscillating. This problem can be solved by the usage of pseudopotentials [89, 90]. Here the numerical problems associated with the electron-ion interaction are eliminated. The chemically inert core electrons are not considered in the calculations and since only the valence electrons are involved, the problem is simpler. Pseudopotentials are often described by their softness, or the kinetic energy cutoff value required to achieve accurate results. Several schemes have been formulated to increase the softness of pseu-

dopotential, leading to ultra-soft pseudopotentials (USPPs). These schemes, however, rely on parameters which render the USPPs less portable across different systems. Some of these issues are solved using the projector augmented wave (PAW) method [91]. PAW pseudo-potentials are often considered superior to USPPs due to the fact they are more transferable and lead to more accurate spin-polarised calculations.

3.2   Nudged elastic band method

The Nudged Elastic Band method [92] was employed to identify the saddle points for the atom-□ exchanges and to calculate the activation energy barriers. The transition from one stable configuration to another takes place along the minimum energy path (MEP) and the difference in the saddle point energy or the energy maximum along the MEP and the initial energy is the activation energy barrier. If one considers the multidimensional energy landscape (see Figure 3.1), a stable configuration is a local minimum, while a saddle point refers to a 'minimax' (maximum along the MEP). Mathematically, the second derivative of a local minima has all positive eigenvalues, while that for a saddle point has exactly one negative eigenvalue. Thus, from the second derivative test, the saddle point can be traced. However, this method would require the evaluation and diagonalization of the second derivative of energy at each step which for a large system with many dimensions (degrees of freedom) is exceedingly difficult.

The plain elastic band method [93] on the other hand requires only the first derivative of the energy. Several states (or 'images') are interpolated between the known end states and these are connected by imaginary spring forces. The object function is defined as,

$$S^{PEB}(\vec{R}_1, \ldots, \vec{R}_{P-1}) = \sum_{i=0}^{P} V(\vec{R}_i) + \sum_{i=1}^{P} \frac{Pk}{2}(\vec{R}_i - \vec{R}_{i-1})^2 \qquad (3.5)$$

where $i = 0, 1, \ldots, P$ represent the images, R_i represent the position coordinates, k_i represent the spring constants and V represents the potential energy. The force acting on an image i is given as the sum of the gradient of the potential energy and the spring
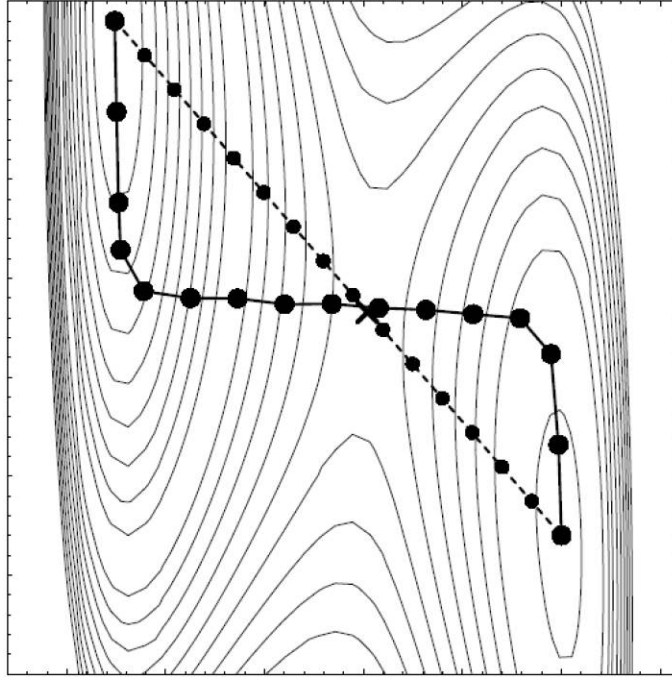
Figure 3.1: The initial and final configurations in a 2-D energy landscape using NEB method with 16 images. The initial linearly interpolated configuration finally converges to the MEP [93]

force,

$$\vec{F}_i = -\vec{\nabla}V(\vec{R}_i) + \vec{F}_i^S \tag{3.6}$$

where

$$\vec{F}_i^S \equiv k_{i+1}(\vec{R}_{i+1} - \vec{R}_i) - k_i(\vec{R}_i - \vec{R}_{i-1}) \tag{3.7}$$

The initial configuration of images is updated according to the forces acting on the images. However, the plain elastic band also fails in certain cases as shown in Figure 3.2. A higher spring constant holds the image too tightly and hence results in corner cutting or an overestimate of the barrier energy. While, if the spring constant is low, the images slide down towards the end points and hence decrease the resolution near the saddle point. The corner cutting is caused by the perpendicular component of the spring force, while the sliding down is caused by the component of the true force $\vec{\nabla}V(R_i)$ in the direction of the path. These forces are projected out in a nudged elastic band method[93], and hence
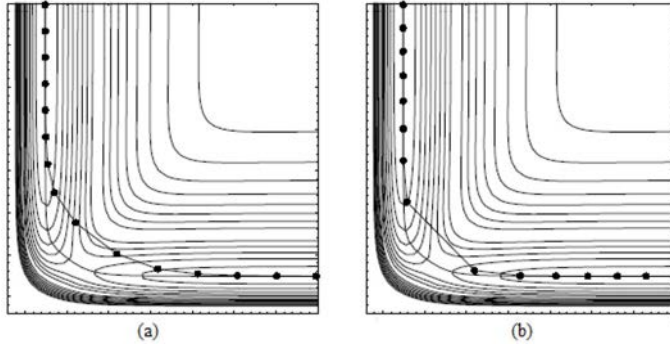
Figure 3.2: The plain elastic band results for a case with a curved path near the saddle point (a) k=1.0, and (b) k=0.1. The result for a NEB is shown by a solid line which goes through the saddle point [93].

the force on an image becomes the sum of the perpendicular component of the true force and the parallel component of the spring force,

$$\vec{F}_i^0 = -\vec{\nabla}V(R_i)|_\perp + \vec{F}_i^S.\hat{\tau}_\parallel\hat{\tau}_\parallel \tag{3.8}$$

Here $\hat{\tau}_\parallel$ is the unit tangent along the path. This action is known as 'nudging' and the method always converges to the MEP, provided sufficient number of images are used in the calculations. Since the spring force only decides the separation between the images, the choice of a spring constant becomes arbitrary[93]. The NEB method can be efficiently run on parallel system of computers with each node handling a single image. A 'climbing image' NEB [92] is a small modification to the NEB where one of the images is pushed to the exact saddle point, thus making the identification of the saddle point easier.

3.3 Settings for calculations

All input data were calculated from first principles, using DFT [86, 87] as implemented in the Vienna *Ab initio* simulation package (VASP) 5.3.2 [94]. The projector augmented wave (PAW) method [91, 95] was used to describe the electron-ion interactions, and the generalized gradient approximation (GGA) parameterised by Perdew, Burke and Ernzerhof [96] was used as E_{XC}. The PAW method was adopted due to its transferability, and

the fact that it has been shown to be more accurate in spin-polarised systems [88]. The GGA was used to approximate the exchange and correlation functional as it has been shown to estimate migration barriers and lattice parameters more accurately [88].

All calculations were spin-polarized. Pure Ni is ferromagnetic below $627\,\mathrm{K}$. As a result, it was deemed appropriate for all calculations used in this work to be spin-polarized. Test calculations were carried out both with and without spin-polarization. It was revealing to see a dramatic difference in Re-Re binding energy within the Ni *fcc* lattice depending on whether calculations were spin-polarized or non-spin-polarized. This will be discussed in the context of the results in Chapter 5.

The electronic self-consistent loops were stopped when the total energy converged to within $10^{-6}\,\mathrm{eV}$ and ionic positions were relaxed until all forces fell below $10^{-2}\,\mathrm{eV/\mathring{A}}$. The conjugate-gradient algorithm was used to relax the atoms in to their instantaneous ground states. A Methfessel-Paxton smearing width [97] of $0.1\,\mathrm{eV}$ was used. The migration barriers were calculated using the 'climbing image' nudged elastic band method [98, 92] using a maximum of 5 images. A spring constant value of $5\,\mathrm{eV/\mathring{A}^2}$ was used. The effective frequencies were calculated within the harmonic approximation as supported by VASP.

The cluster expansion was performed using the CASM code (Cluster-Assisted Statistical Mechanics) developed by the Van der Ven Research Group at the University of Michigan [81, 82].

3.4 Convergence tests

In each numerical approximation within DFT, it is possible to find a solution that is closer to the exact solution by using more computational resources. As computational time is not unlimited, however, we must ensure we restrict ourselves to our required accuracy. A 'well-converged' solution is one where we get accurate results, but not at the expense of unnecessarily high computational time. In DFT calculations, computational parameters, most notably the quality of plane wave basis sets (defined by the energy cutoff) and the
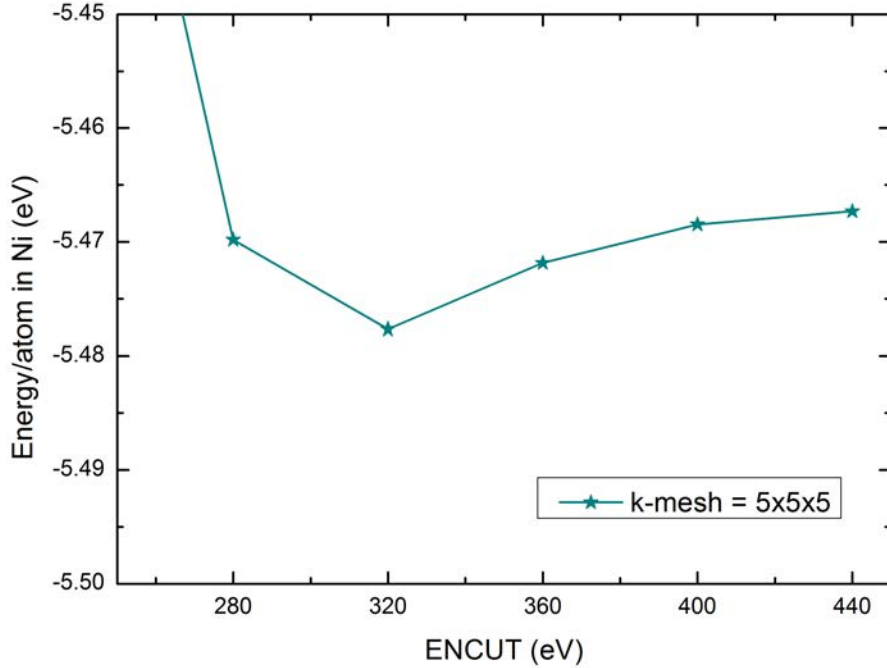
Figure 3.3: The convergence of energy per atom in Ni at different values of energy cutoffs

density of k-meshes for integrations in reciprocal space need to be optimized for achieving the desired level of accuracy in calculations of materials properties [88].

Total energies of 108-atom supercells of pure Ni, Re, W and Ta were computed using a variety of k-point meshes and energy cutoffs. Figure 3.3 shows the energy values per atom for the pure Ni system at different values of energy cutoffs (for a fixed k-point mesh). The results for the convergence tests in Re, W and Ta have been presented in Figures 3.5, 3.6 and 3.7. Considering the results of convergence tests for all the other elements considered in this work, it was decided that an energy cutoff of 400 eV would be appropriate. The total energy is expected to be accurate within 1 meV for an energy cutoff of 400 eV.

Figure 3.4 shows the energy values per atom for the pure Ni system calculated using different k-point meshes (while using a fixed energy cutoff). We can see that the total energy converges to within 1 meV for a $5 \times 5 \times 5$ k-point mesh made using the Monkhorst-Pack scheme [99]. It should be pointed out that most errors within DFT calculations
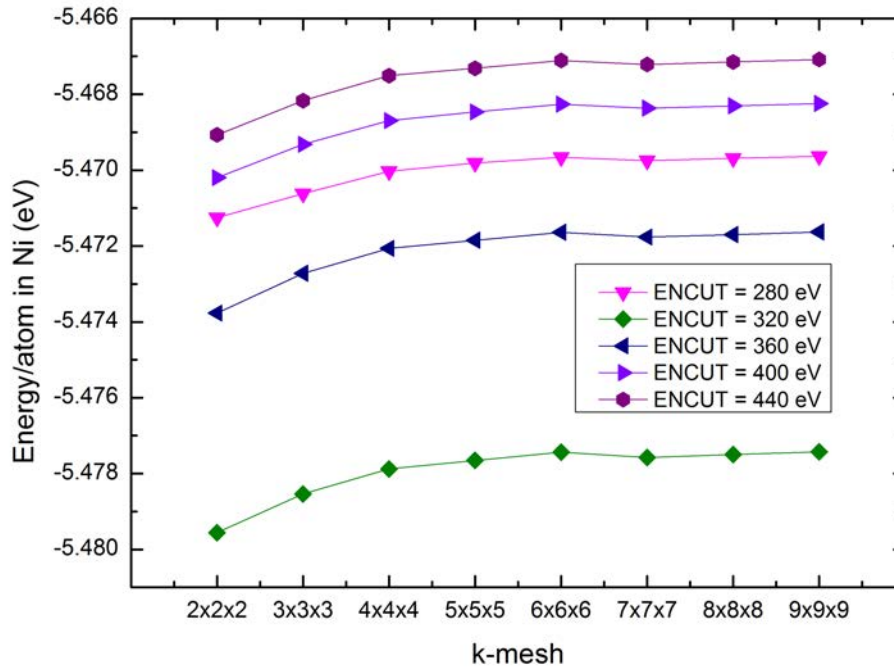
Figure 3.4: The convergence of energy per atom in Ni with different k-point densities

are systematic, and that energy differences converge faster with respect to the precision adopted for the various numerical approximations.

Further discussion on the convergence of NEB calculations particularly with respect to the supercell size has been presented in Section 4.1.4.
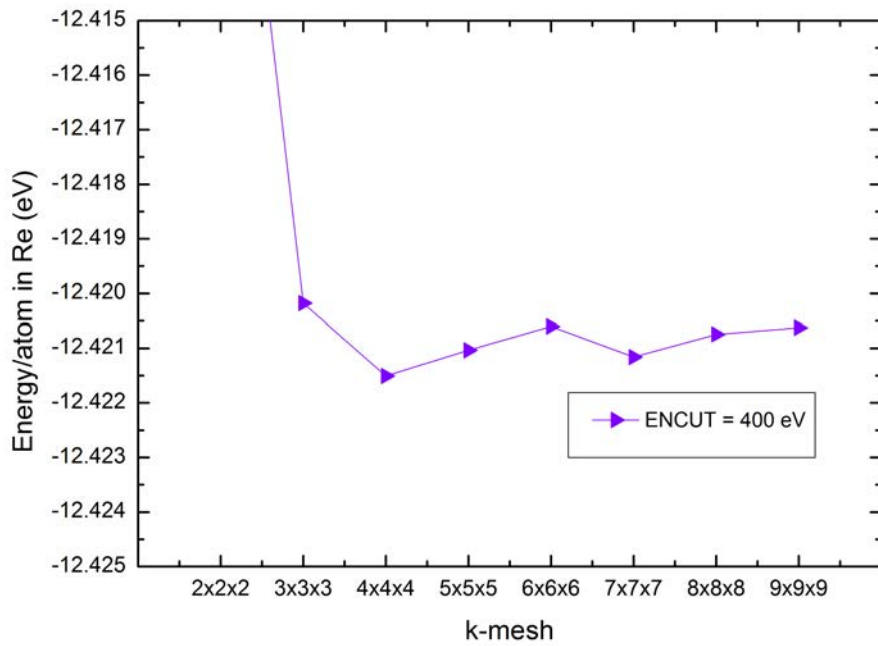
(a) Energy per atom in Re versus k-point densities
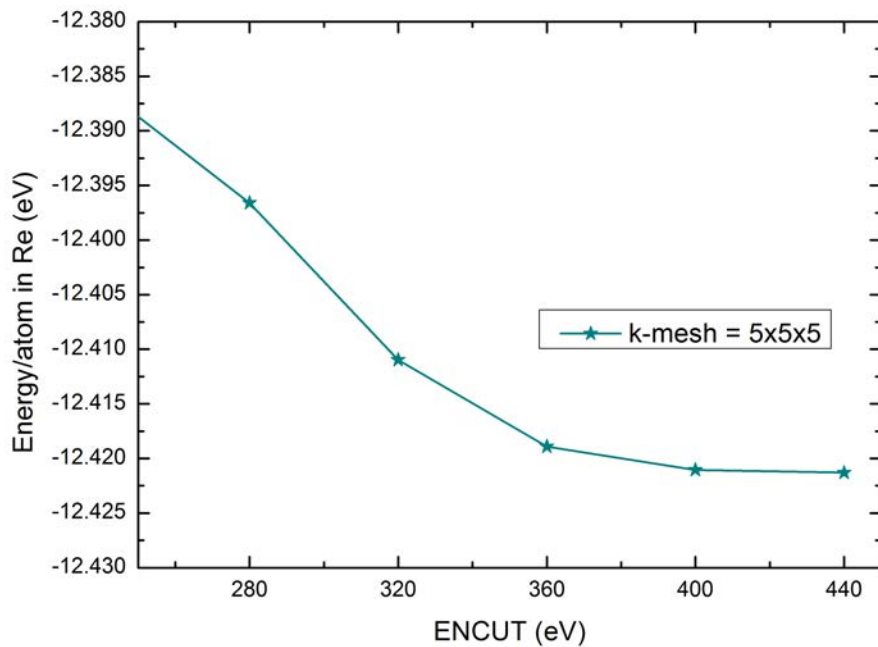
(b) Energy per atom in Re versus energy cutoffs

Figure 3.5: Results for convergence tests in Re
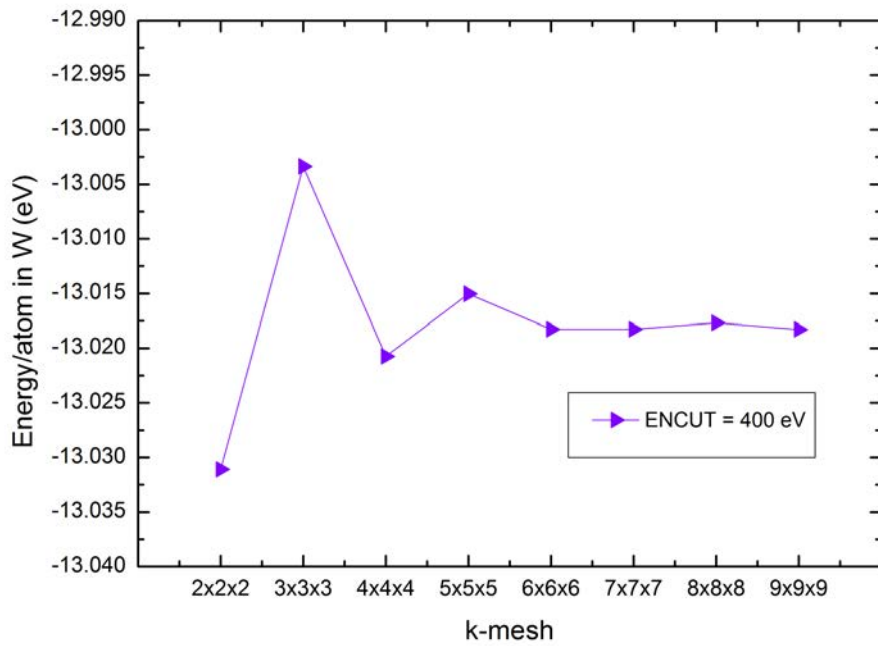
(a) Energy per atom in W versus k-point densities
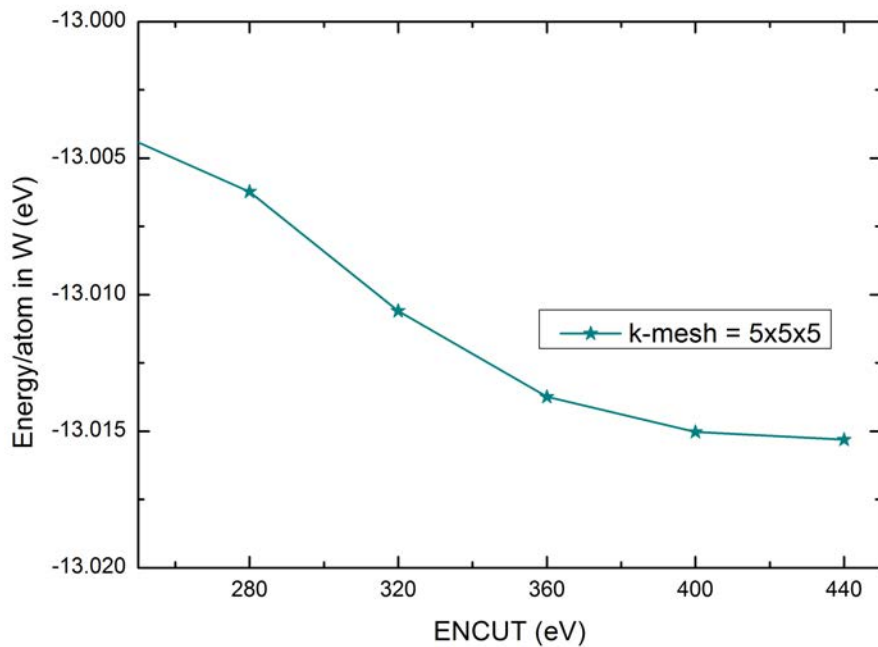
(b) Energy per atom in W versus energy cutoffs

Figure 3.6: Results for convergence tests in W
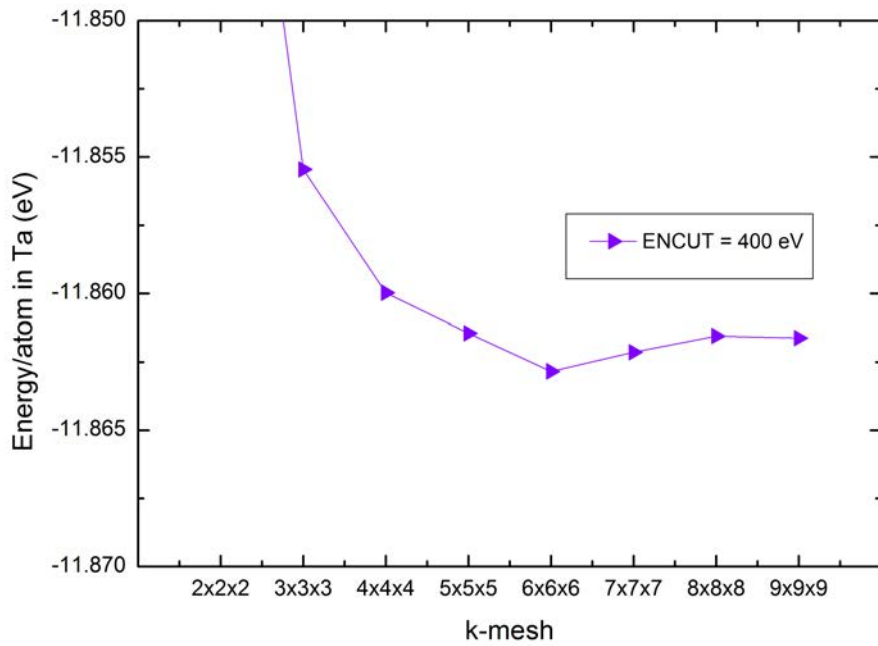
(a) Energy per atom in Ta versus k-point densities
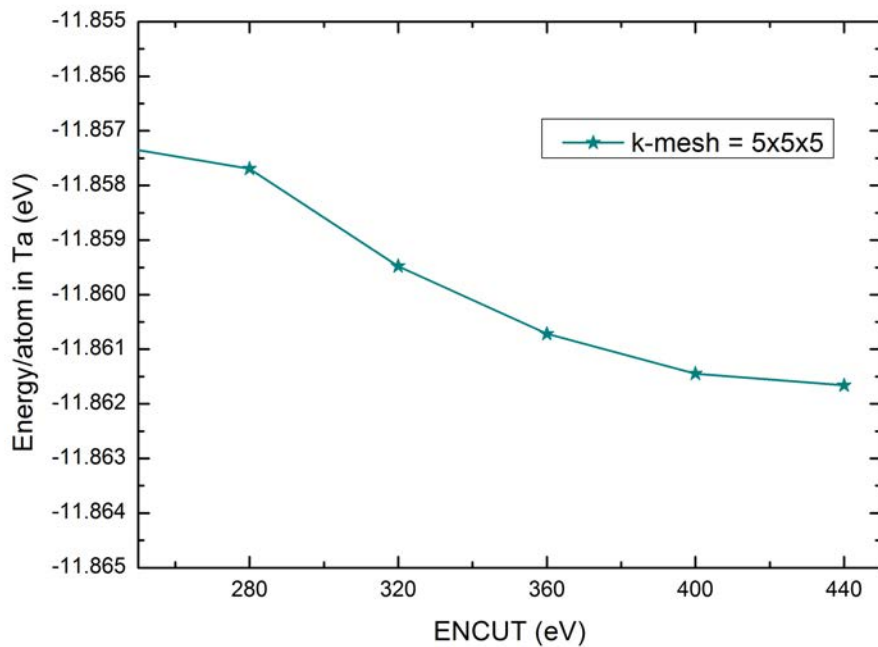
(b) Energy per atom in Ta versus energy cutoffs

Figure 3.7: Results for convergence tests in Ta

CHAPTER 4

DIFFUSION IN DILUTE ALLOYS

4.1 Results from analytical expressions

All the calculated values from Equation (2.6) have been presented in the following sections. For nudged elastic band calculations, only the internal degrees of freedom of the supercells were relaxed and the supercell size was fixed to that calculated for pure Ni. The total energies change only by about $\pm$ 0.03 eV when the supercell volume and shape relaxations were taken into account. For all other calculations, besides the internal degrees of freedom of the supercells, the volume and the shape of the supercells were relaxed as well. Most of the remaining details of the computational setup are mentioned in Section 3.3. Further details about particular calculations have been discussed in their respective sections.

4.1.1 Lattice parameters and local relaxation around defects

The relaxed volume for a $3 \times 3 \times 3$ supercell of pure Ni corresponded to a lattice parameter value, a of 3.52 Å, which fits well with the experimental Ni lattice parameter of 3.524 Å [100]. In order to calculate the change in the macroscopic lattice parameter (Δa) on the introduction of a defect, the corresponding defect was introduced in the $3 \times 3 \times 3$ supercell of Ni, replacing one of the Ni atoms. For a vacancy, a decrease of 0.005 Å was calculated for the macroscopic lattice parameter, while for the cases of Re, W and Ta an increase

Table 4.1: The calculated change in the macroscopic lattice parameter (Δa) and the percentage local relaxation for a vacancy and for Re, W and Ta in Ni

Defect	Δa (Å)	% relaxation
Vacancy	-0.005	-1.56
Re	0.002 0.0036 [101]	0.37 0.27 [29]
W	0.003 0.0038 [101]	0.70 0.63 [29]
Ta	0.005 0.0054 [101]	1.80 1.51 [29]

of 0.002 Å, 0.003 Å and 0.005 Å respectively was calculated for the same. These values were consistent with the theoretical work of Wang et al [101] (see Table 4.1).

The results for the introduction of the defect on the local relaxation in the 1st nearest neighbour distance between the defect and a Ni atom in reference to the 1st nearest neighbour distance between two Ni atoms in a pure Ni supercell have been tabulated in Table 4.1. For the case of a vacancy, the 1st nearest neighbour distance reduces to 1.56 %. This is because the 1st nearest neighbour shell of Ni atoms around a vacancy will be pushed inwards owing to the net compressive stress from the Ni atoms surrounding the shell. On the other hand, the introduction of all the solute atoms tend to push the 1st nearest neighbour shell of atoms outwards thereby producing a positive local strain. The calculated values were 0.37 % for Re, 0.70 % for W and 1.80 % for Ta respectively, and these values match well with the results of Mottura et al [29]. This is expected given the atomic radii of Re, W and Ta are 1.97 Å, 2.02 Å and 2.09 Å respectively when compared to 1.62 Å for Ni [29]. However, the size misfit does not completely describe the magnitude of local relaxation and the electronic effects must also be considered. It can be inferred that Re, in comparison to W and Ta, forms a stronger directional bond with the Ni atoms, thus leading to a smaller expansion in nearest neighbour distance.
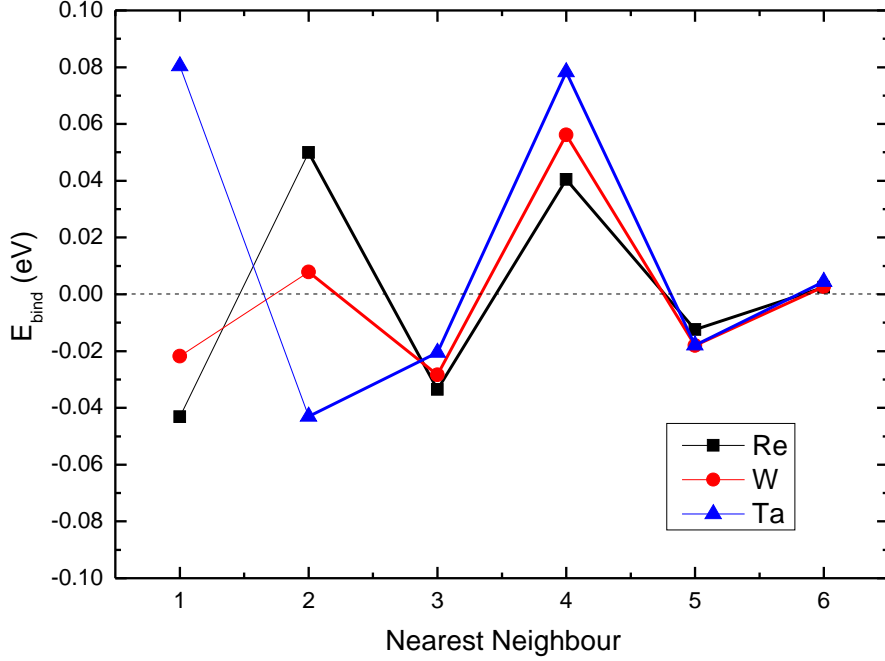
Figure 4.1: The binding energies of solute-□ pairs at various distances in the Ni lattice [63]

4.1.2 Vacancy formation energy

The vacancy formation energy in pure Ni, $\Delta E_{\mathrm{f},Ni}$ was calculated as 1.44 eV. This is in agreement with the value of 1.42 eV from other first principles work using GGA functionals [52]. However, the value is lower when compared to experiments (see Table 4.3). This is generally expected that the first principles vacancy formation energy is an underestimation of the experimental value [102]. As mentioned previously, we have assumed $\Delta S_{\mathrm{f}}^{\mathrm{vib}} = 1.4k_{\mathrm{B}}$, computing an average of two values reported by Seeger et al [55] calculated by fitting the experimental Ni-self diffusion data.

For the calculation of the vacancy formation energy in solute i, $\Delta E_{\mathrm{f},i}$, we calculated the binding energies for the i-□ pairs for the 1st nearest neighbour position and also extended the calculations to the 2nd, 3rd, 4th, 5th and 6th nearest neighbour positions (see Figure 4.1).

From the definition [29], a negative binding energy means a repulsion between the

vacancy and the solute atom. We can see that the binding energies differ greatly between the three solutes in the first two nearest neighbour positions. For the 1st nearest neighbour position, Re and W show values of -0.04 eV and -0.02 eV respectively for the binding energy, while Ta shows a value of +0.08 eV. This means that Ta prefers a vacancy on its 1st nearest neighbour position, while Re and W do not. The presence of the vacancy affects the bonding between the solute and the Ni atoms. This can be referred to as the electronic effect and it is stronger when the vacancy is relatively close to the solute atom. The change from an attractive binding energy in Ta to repulsive binding energies in W and Re can be attributed to the increased band filling from Ta to W and Re. The results agree with the work of Schuwalow et al [52]. However, these interactions are weak, considering their magnitude. Also, one can see that from 3rd nearest neighbour position onwards, the behaviour of all the three solutes become similar and finally the binding energies vanish at the 6th nearest neighbour position. Here the elastic effects due to the size mismatch of the solute and host Ni dominate the electronic effects and hence all the solutes show similar behaviour. The $\Delta E_{f,Ni}$ value and the $\Delta E_{f,i}$ values for Re, W and Ta are tabulated in Table 4.3.

4.1.3 Effective frequencies

The lattice dynamics, as supported by VASP allows to calculate the Hessian matrix, or the second derivative of the energy with respect to the atomic positions and hence the vibrational frequencies of a system. The calculation of the full Hessian of all the atoms in the supercell is computationally intensive. Hence, these calculations were performed for a single Ni, Re, W and Ta atom which undergo a vacancy exchange at the initial and the saddle point of the transition. This simplification has been used previously [36, 103] as well. Each atom is displaced in x, y and z directions by a small positive and negative displacement (0.015 Å) and from the forces, the Hessian matrix is calculated.

Table 4.2 shows the three normal frequencies calculated at the initial point of the transition, the two normal frequencies at the saddle point (one frequency at the saddle

Table 4.2: The calculated effective frequencies for Ni, Re, W and Ta

Solute	Vibrational frequencies at the initial point(THz)			Vibrational frequencies at the saddle point(THz)		ν_i^* (THz)
Ni_{self}	6.03	5.99	5.10	10.14	7.06	2.57 4.48 [103]
Re	4.30	4.14	3.53	7.25	5.17	1.67
W	4.52	4.36	3.78	6.74	4.69	2.36
Ta	4.48	4.38	3.70	6.18	4.59	2.56

point is imaginary (see Equation (2.12)) and the calculated effective frequency ν^*. It must be noted that the calculated effective frequencies are in the range of tera Hertz (10^{12} Hz), showing how vigorously the atoms vibrate about their mean positions in a crystal lattice. A ν^* value of 2.57 THz was calculated for the case of Ni, as compared to a value of 4.48 THz calculated by Tucker et al [103] from their first principles work. The ν^* values of Re, W and Ta differ slightly, but are in the same approximate range. Given the similar masses of the three solutes, the differences in their calculated frequencies are related almost entirely to the calculated Hessian matrix (see subsection 2.1.1), which in turn is related to the energy landscapes at the initial and the saddle points of the transition. All the three solutes are expected to have similar energy landscapes at the initial points of the transition as implied from the calculated vibrational frequencies at the initial points. However, at the saddle point, Re exhibits higher vibrational frequencies compared to W and Ta, leading to a smaller ν^* value. This implies that a small displacement of a Re atom from its saddle point would lead to a higher penalty in the energy as compared to that of a W or a Ta atom. The ν^* values of Re, W and Ta have been calculated by Janotti et al [36] but have not been explicitly reported, and hence a comparison was not possible.

4.1.4   Migration energy barriers

A 3×3×3 supercell of Ni atoms containing 1 solute atom and 1 vacancy was used for the calculations. The solute atom and the vacancy were positioned next to each other and the energy of the supercell was calculated. This represents the initial state. The

final state is when the solute has exchanged its position with the vacancy. The migration energies $\Delta E_{\mathrm{m},i}$ were calculated using the 'climbing image' nudged elastic band method (Section 3.2). A $3\times3\times3$ supercell was considered large enough for these calculations as the jumping atom and the vacancy were beyond 6th nearest neighbour positions to their respective images across the periodic boundaries. From Figure 4.1 , it can be seen that the solute-□ binding energies become negligible at 6th nearest neighbour positions, and hence the solute atom is not expected to interact with the vacancy beyond this distance. It is noteworthy that all NEB calculations described in the present work are 1st nearest neighbour vacancy jumps. Furthermore, in all the supercells considered, the vacancy and the solute atoms were at a maximum of 4th nearest neighbour distance to each other. The use of a larger supercell was thus not necessary for the NEB calculations, besides being computationally intensive.

Given the simple energy landscape for a 1st nearest neighbour vacancy jump, only one NEB image between the initial and final states was sufficient for the calculation of $\Delta E_{\mathrm{m},i}$. The obtained results were also compared to NEB calculations using 5 images and the results were found to converge within $\pm$ 0.01 eV. Figure 4.2 shows the end states and the minimum energy path traced by 5 images for Ni-□, Re-□, W-□ and Ta-□ exchanges. The energies have been normalized by subtracting the energy of the initial state from the energies of all the images. At the end of the NEB calculations, one of the images is nudged to the saddle point along the minimum energy path, and this corresponds to the activated state. $\Delta E_{\mathrm{m},i}$ is given as the difference between the energies of the activated state and the initial state. These values have also been tabulated in Table 4.3.

The $\Delta E_{\mathrm{m},i}$ value calculated for Ni is 1.08 eV, as compared to 1.24 eV [36] from the results of Janotti et al [36]. The observed differences can be attributed to the use of $2\times2\times2$ supercells and LDA functionals in their calculations, as compared to $3\times3\times3$ supercells and GGA functionals in the present work. They had argued that $2\times2\times2$ supercells produce similar results for $\Delta E_{\mathrm{m},i}$ as compared to larger supercells, but this is not true as concluded by Schuwalow et al [52]. This is expected given the interaction of the solute atom/vacancy

with their respective images across the periodic boundaries in a smaller supercell would be stronger. Amongst the solutes considered, Re shows the highest $\Delta E_{\mathrm{m},i}$ value of 1.51 eV, and Ta shows the lowest $\Delta E_{\mathrm{m},i}$ value of 0.77 eV, while W has a $\Delta E_{\mathrm{m},i}$ value of 1.27 eV. These results match well with the results of Schuwalow et al [52], also using $3\times3\times3$ supercells and GGA functionals. The small differences could be attributed to the use of 350 eV as the energy cutoff in their calculations as compared to 400 eV used in the present work.
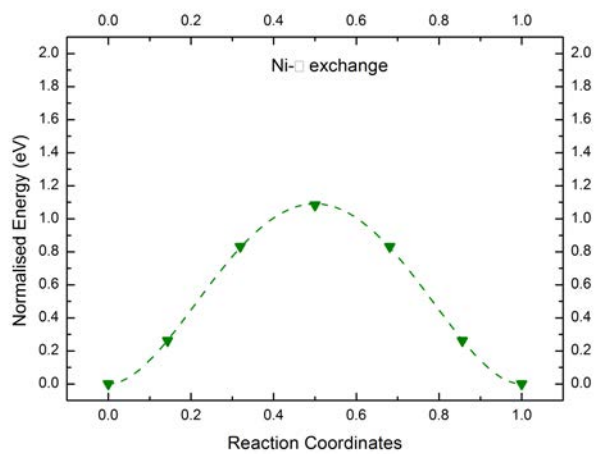
(a) Ni
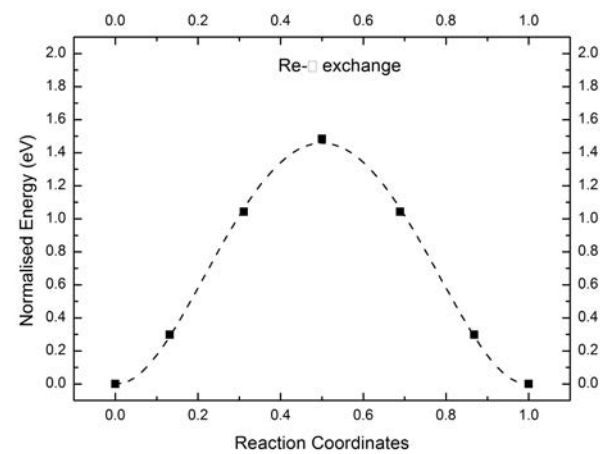
(b) Re
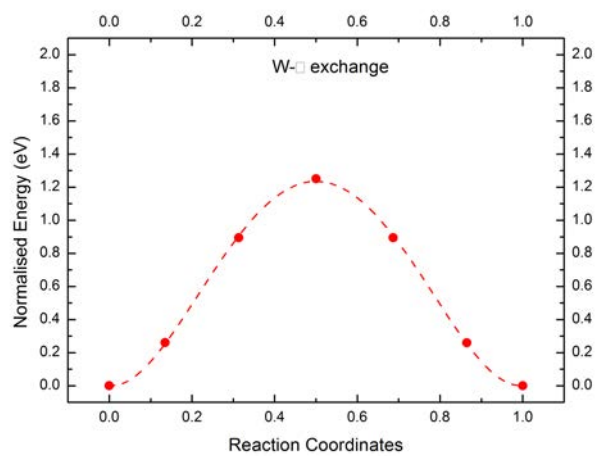
(c) W
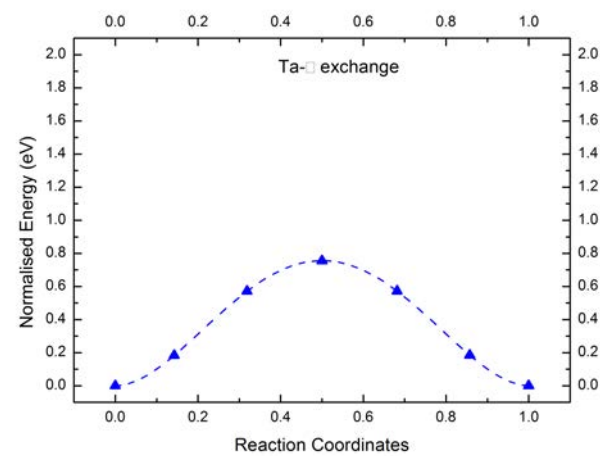
(d) Ta

Figure 4.2: The minimum energy path connecting the initial and final end states for various solute-□ jumps

4.1.5 Solute correlation factors

The migration energy barriers for the rotation, dissociation and association of the solute-□ pairs were similarly calculated. Only a single image was used in the NEB calculations, as described in Section 4.1.4. The explicit calculations have been depicted in Figure 4.3. The vacancy is located at a 1st nearest neighbour position to the solute atom. Thus, a vacancy jump from its position to another 1st nearest neighbour position will cause the solute-□ pair rotation. A vacancy jump to a 3rd nearest neighbour position will cause the solute-□ pair dissociation, while a reverse jump would cause the solute-□ pair association. The solute-□ pair exchange corresponds to the vacancy exchanging its position with the solute atom.

It must be noted that there are other possible rotational as well as dissociative jumps for a solute-□ pair, however, the Lidiard's model [59] only allows a single value for each of these jumps (see Equation (2.15). The number of possible dissociative jumps to take the vacancy to a 2nd, 3rd and 4th nearest neighbour positions are 2, 4 and 1 respectively (see Figure 4.9). Hence, the dissociative jump to a 3rd nearest neighbour position is the most common one and is used in the calculations here. On the other hand, the solute-□ pair rotation from a 1st nearest neighbour position to another 1st nearest neighbour position is the only relevant rotational jump in the Lidiard's model [59]. Section 4.2.1 has a more elaborate description of the various vacancy jumps around the solute atom.

Table 4.3 shows the calculated values for $\Delta E_{\mathrm{rot},i}$, $\Delta E_{\mathrm{dis},i}$ and $\Delta E_{\mathrm{ass},i}$ from the present work. All these values for Re are very similar to the $\Delta E_{\mathrm{m},i}$ value of 1.08 eV for the self-diffusion in Ni suggesting that these jumps are almost independent of the presence of the Re atom in the neighbourhood. On the other hand, for the case of Ta, these jumps produce different results, with a value of 1.37 eV for $\Delta E_{\mathrm{rot},i}$, 1.00 eV for $\Delta E_{\mathrm{dis},i}$ and only 0.91 eV for $\Delta E_{\mathrm{ass},i}$. The results have been compared to that of the first principles work of Schuwalow et al [52] and the agreement is very good. However, there was a systematic decrease of the values by approximately 0.05 eV. This can be attributed to the slightly different calculation settings used by Schuwalow et al [52], particularly the energy cutoff
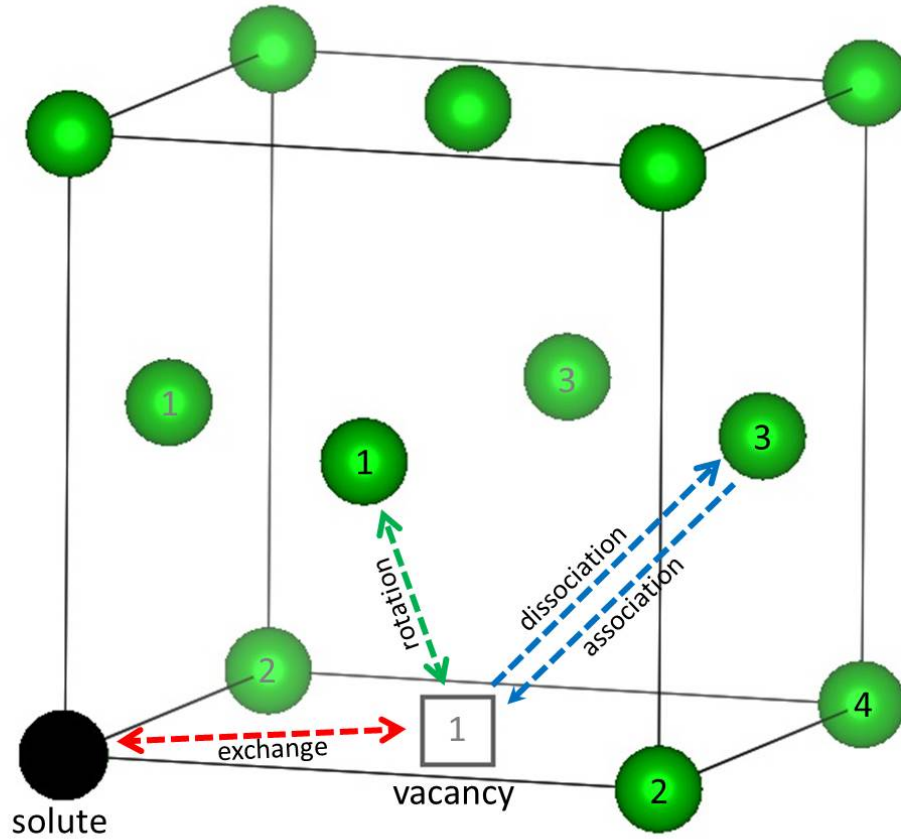
Figure 4.3: An *fcc* cell showing a solute atom (black), a vacancy (empty square), the Ni atoms (green) and their nearest neighbour relationship to the solute atom and the various vacancy jumps corresponding to the calculated migration barriers. There are more than one symmetrically equivalent atoms, but only one case of solute-□ pair rotation and solute-□ pair dissociation/association has been shown for clarity.

values.

The solute correlation factors, f_i were calculated according to Equation (2.15) and the values in the temperature range of 1173 K - 1573 K have been shown in Figure 4.4. The choice of the temperature range was made in order to compare the results for the calculated diffusion coefficients to previous works in the literature [37, 36], besides covering the intermediate and high temperature creep regime in Ni-based superalloys. For all jumps, except for the solute-□ exchange, a ν_i^* of 2.57 THz was used. It was seen that the correlation factor varies only slightly for all solute atoms in the temperature range considered. For the case of Re and W, $\Delta E_{\mathrm{rot},i}$ and $\Delta E_{\mathrm{dis},i}$ values were found to be much
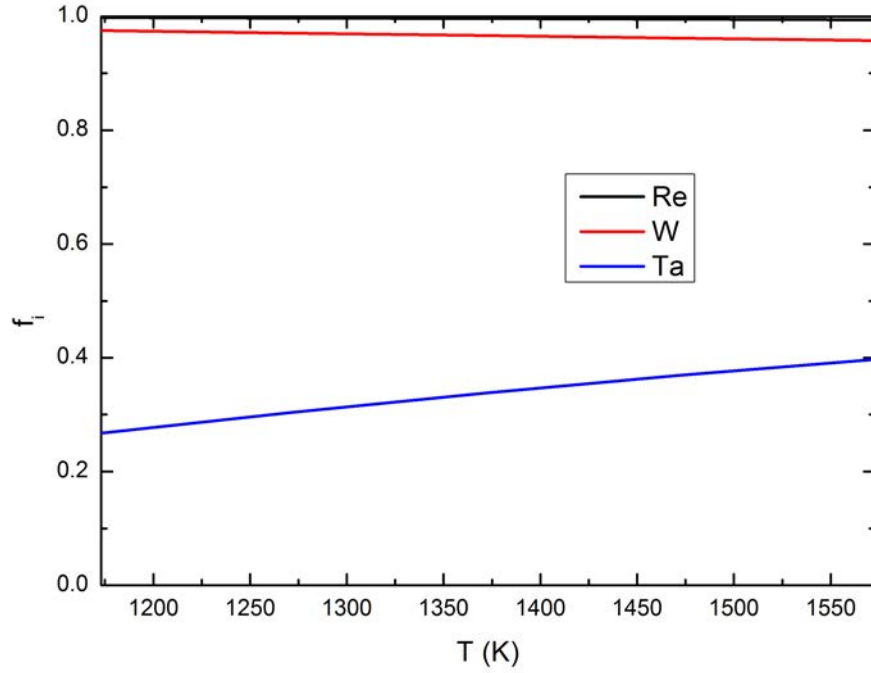
Figure 4.4: The solute correlation factors f_i calculated in the temperature range of 1173 K to 1573 K.

lower than $\Delta E_{\mathrm{m},i}$, thus yielding a value of $f_i \approx 1$. Thus, Re and W are expected to perform a random walk in a dilute alloy of Ni. On the contrary, for the case of Ta, $\Delta E_{\mathrm{rot},i}$ and $\Delta E_{\mathrm{dis},i}$ values were much higher than $\Delta E_{\mathrm{m},i}$. This results in a higher Ta-□ exchange frequency and thus a reverse exchange between a Ta atom and a vacancy would be the most probable event following a successful exchange, which means correlation effects are strong for Ta diffusion. A f_i value of 0.338 was calculated for Ta at 1373 K, in comparison to a f_i value of 0.996 for Re and 0.966 for W.

Table 4.3: The calculated terms for self-diffusion and solute diffusion in Ni

Solute	ν_i^* (THz)	f_i (1373K)	D_0^i (x10^{-7}m^2/s)	$\Delta E_{f,i}$ (eV)	$\Delta E_{\mathrm{m},i}$ (eV)	Q_i (eV)	$\Delta E_{\mathrm{rot},i}$ (eV)	$\Delta E_{\mathrm{dis},i}$ (eV)	$\Delta E_{\mathrm{ass},i}$ (eV)
Ni$_{\mathrm{self}}$	2.57 4.48 [103]	0.781	10.1 920 [48],1770 [49], 1900 [106], 920 [108], 400 [109], 3360 [110], 5120 [111]	1.44 1.54 [104], 1.73 [105], 1.58-1.63[107] 1.7[36],1.42 [52]	1.08 1.24 [36] 1.01 [52]	2.52 2.88 [48], 2.955 [49], 2.90 [106], 2.88 [108], 2.77 [109], 3.03 [110], 3.08 [111], 2.65-2.82 [112]	-	-	-
Re	1.67	0.996	8.37 8.2 [37], 10.4 [52]	1.48	1.51 1.46 [52]	2.99 2.64 [37], 3.50 [36], 2.91 [52]	1.13 1.05 [52]	1.07 1.00 [52]	1.08 1.02 [52]
W	2.36	0.966	11.44 80 [37],11.0 [52], 1130 [113], 2200 [114]	1.46	1.27 1.22 [52]	2.73 2.74 [37], 3.08 [113], 3.14 [114], 3.05 [36], 2.66 [52]	1.20 1.16 [52]	1.04 0.98 [52]	1.04 0.98 [52]
Ta	2.56	0.338	4.35 219 [37], 15.4 [52]	1.36	0.77 0.75 [52]	2.13 2.60 [37] 2.34 [36], 2.28 [52]	1.37 1.33 [52]	1.00 0.96 [52]	0.91 0.86 [52]

4.1.6 Ni-self diffusion coefficient and solute diffusion coefficients in Ni

Using Equations (2.16) and (2.17), calculations were initially done on the pure Ni system to obtain the self-diffusion coefficient in Ni, using a value of $3.52\,\text{Å}$ as lattice parameter. A $D_{0,\text{Ni}}$ value of $10.1 \times 10^{-7}\,\text{m}^2/\text{s}$ was obtained, while Q_{Ni} was computed at $2.52\,\text{eV}$ (or $243\,\text{kJ/mol}$). The calculated values produce a self-diffusion coefficient (see Figure 4.5) which agrees with available data in the literature in the intermediate temperature regime [48] and is within an order of magnitude in the high temperature regime [49]. The experimental values for $D_{0,\text{i}}$ and Q_i are commonly obtained by fitting the diffusion data to the Arrhenius relationship. As a result, these values may not be necessarily expected to match the pre-factor and activation energy values obtained from first principles. Indeed, a large scatter is observed in the experimental values for $D_{0,\text{Ni}}$ and Q_{Ni} reported in the literature(see Table 4.3). We chose to compare only to data obtained from single-crystal Ni samples tested over a range of temperature[48, 49] .
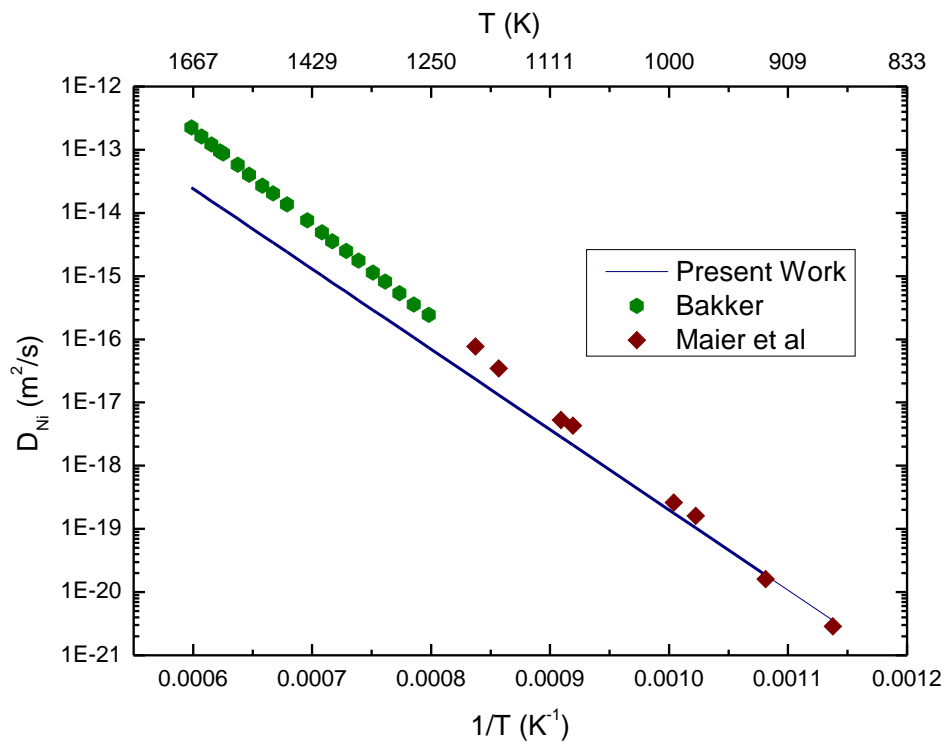
Figure 4.5: The self-diffusion coefficient of Ni calculated from first principles[63] compared to experimental values (Bakker [49] and Maier et al [48]) .
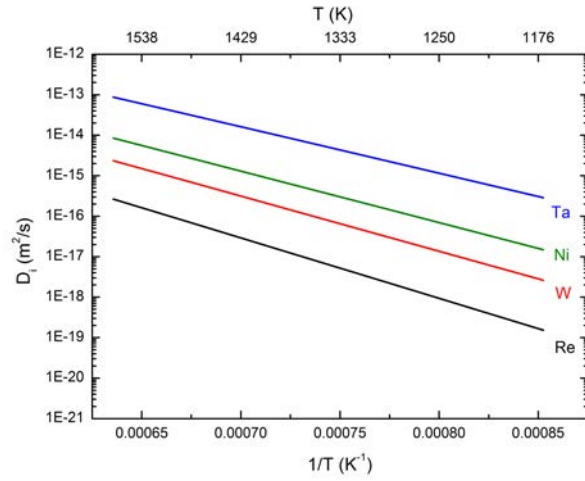
(a) D_i for all solutes and D_{Ni}^{self}
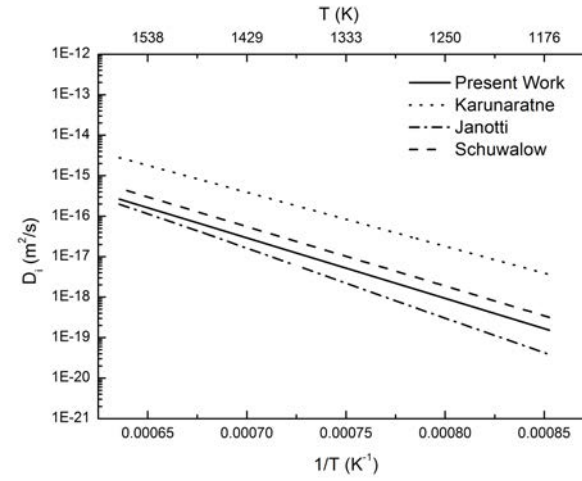
(b) D_{Re} - comparison
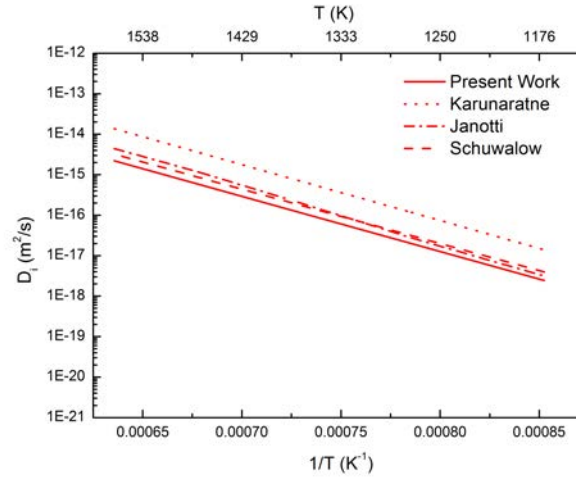
(c) D_W - comparison
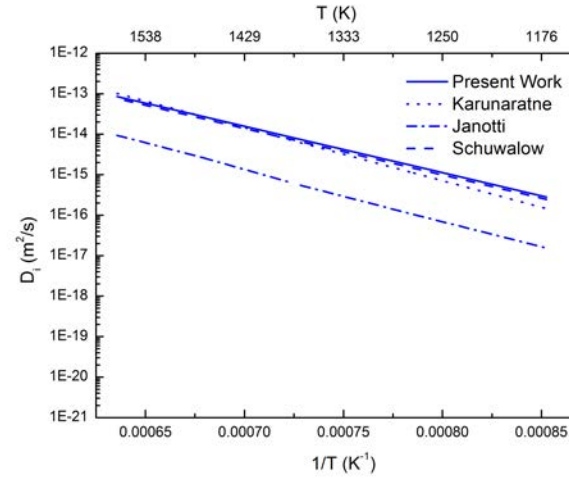
(d) D_{Ta} - comparison

Figure 4.6: (a)The solute diffusion coefficients in Ni as a function of temperature. Ni-self diffusion coefficient has been included as well for comparison. (b)-(d) Comparison of the solute diffusion coefficients to previous works in the literature [37, 36, 52].

Calculations were then run for Re, W and Ta as solute atoms in 108-atom supercells. All the terms in the pre-factors ($D_{0,i}$) and activation energies (Q_i) have been tabulated in Table 4.3. The resulting diffusion coefficients for Re, W and Ta are shown in Figure 4.6, and agree with both experimental and theoretical data available in the literature (see Table 4.3). The diffusivity of Re and W are respectively roughly two orders and one order of magnitude lower than the diffusivity of the host Ni. In contrast, Ta is expected to diffuse an order of magnitude faster than Ni. The solute diffusion coefficients calculated from the present work have also been plotted along with the results from the experimental work of Karunaratne et al [37] and the first principles work of Janotti et al [36] and Schuwalow et al [52]. While the results are in excellent agreement with those of Schuwalow et al [52] for all the solutes in Ni, there is a difference of about an order of magnitude for the case of Ta when compared to the results of Janotti et al [36]. Similar to the present work, Schuwalow et al [52] have used the generalized gradient approximation (GGA) to perform their first principles calculations on $3 \times 3 \times 3$ supercells, while the results of Janotti et al [36] were obtained using local density approximation (LDA) on $2 \times 2 \times 2$ supercells.

A comparison with the experimental work of Karunaratne et al [37] shows a good match for the case of Ta, but a difference of approximately an order of magnitude for the cases of W and Re. It must be noted that the reported experimental data was determined from the interdiffusion coefficients $\tilde{D}$ in these systems. However, experiments were conducted by these authors over a range of composition in the dilute regime ($<$ 3.5 at.%), and it was observed that $\tilde{D}$ remained independent of composition in all the three systems in the dilute regime. Assuming the thermodynamic factor in the Darken's second equation [43] to be equal to unity, the interdiffusion coefficients $\tilde{D}$ in the dilute regime should be approximately equal to (within an order of magnitude) the solute diffusion coefficients D_i.

4.1.7 Vacancy diffusion coefficients in Ni

Before applying Manning's random alloy model, its validity for the current system must be ensured. First, Manning's model assumes for the binary alloy to be random and for the solute atoms to have negligible binding energies with vacancies (*i.e.* vacancy distribution must also be random). The distribution of Re, W and Ta in Ni has been the subject of several studies [28, 27, 29], all confirming using a variety of techniques that the distribution of dilute amounts of these solute atoms in Ni should be expected to be random at elevated temperatures. The binding energies for solute-□ pairs have also been calculated from first principles (see Figure 4.1). These values are small relative to the vacancy formation and migration energy, and the distribution of vacancies can be assumed to be random. Second, Manning's model assumes that the exchange frequency of an atom-□ pair is only dependent on the atom exchanging places with the vacancy, and unbiased by the identity of neighbouring atoms. In other words, the migration barriers for solute-□ rotation, dissociation and association should be similar to the migration barrier of the solvent. This is approximately the case for Re and W (see Table 4.3), but not the case for Ta, which is not the primary focus of the present study. We can therefore conclude that, at least for Re and W, Manning's model for estimating vacancy diffusion is valid to a first approximation.

Using the values for diffusion coefficients obtained above, we can calculate the vacancy correlation factor (f_v) using in Equation (2.30) as a function of temperature and composition for Re and W additions. As discussed in Section 2.1.2, Equation (2.30) breaks down when the solute atoms diffuse faster than the solvent. Therefore, for Ta, we use the vacancy correlation factor calculated according to Equation (2.20). The use of Equation (2.20) for Re and W does not produce substantially different results when compared to the correlation factors obtained from Equation (2.30). The change of f_v with solute concentration at 1373 K is shown in Figure 4.7. For a pure metal, the vacancy correlation factor is unity and remains close to unity with small additions (up to 5 at.%) of Re and W. The addition of a fast-diffusing solute atom, on the other hand, results in a drop in
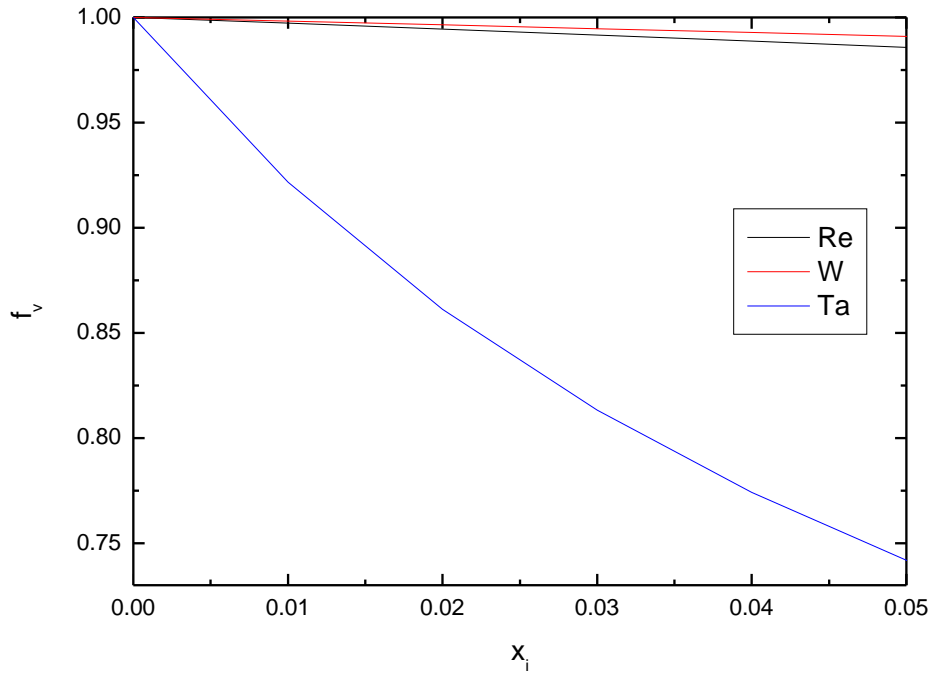
Figure 4.7: Vacancy correlation factors in Ni at 1373 K[63]

f_v due to the fact that reverse solute-□ exchanges are more likely than Ni-□ exchanges.

Finally, the vacancy diffusion coefficient in a dilute binary alloy, D_v, can be estimated. The results for 1373 K in binary Ni alloys with up to 5 at.% Re, W and Ta are shown in Figure 4.8. Also in this case, Re and W are seen to decrease the vacancy diffusion coefficient, albeit the effect is small. The addition of 5 at.% Re and W results in a reduction of vacancy diffusion coefficient of less than 10% when compared to vacancy diffusion in pure Ni. The addition of Ta, as expected, increases the vacancy diffusion rate. The lower vacancy correlation factor in the presence of Ta additions does not negate the effects of the higher Ta-□ exchange frequency on the overall vacancy diffusion rate.
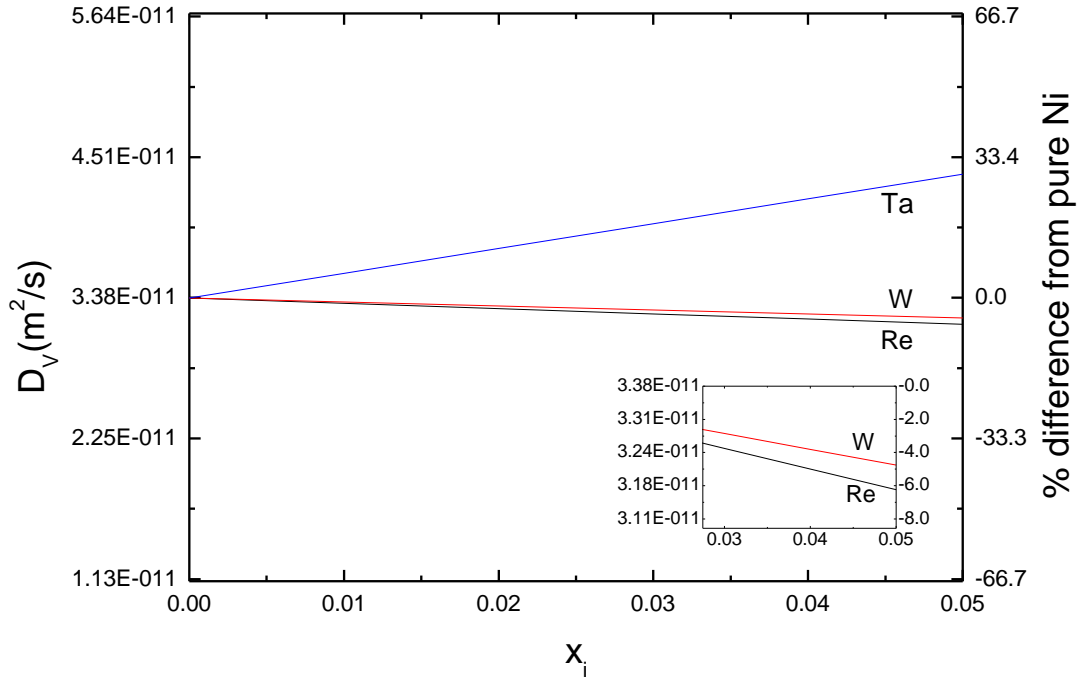
Figure 4.8: Vacancy diffusion coefficients in Ni as a function of solute concentration at 1373 K[63]

4.2 Results from kinetic Monte Carlo Simulations in dilute alloys

The Manning's random alloy model is marred by a number of simplifying assumptions, especially in the calculation of the vacancy correlation factors. On the other hand, the kinetic Monte Carlo method simulates the vacancy movement through the lattice and hence inherently includes the effect of correlation. The validity of the results obtained from kMC simulations depend on the diffusion barriers used, which for the present work has been described in subsection 4.2.1.

The kMC code used for dilute alloys in Ni was provided by Dr. Sergej Schuwalow of the Interdisciplinary Centre for Advanced Materials Simulation at the Ruhr-Universität, Bochum, Germany. Possible atomic positions were mapped onto an *fcc* lattice with periodic boundary conditions and the system evolved by atoms/vacancies hopping between first nearest neighbour lattice sites. Only one solute atom was placed in the system

to model the dilute alloys. Also, only one vacancy was placed in the system to avoid vacancy-vacancy interactions. This is a good approximation as the vacancy concentration in metallic alloys like Ni tend to be small even at high temperatures.

4.2.1 Migration energy barriers for extended vacancy jumps

A number of migration barriers have been included to model the system to a greater accuracy. Under dilute approximation, only one solute atom has been included in the system, hence migration barriers for a solute-□ exchange in the presence of another solute atom has not been considered. We expect the results to be valid in the dilute limits of less than 1 at. %.

All the vacancy jumps up to the 4th nearest neighbour distance to the solute atom have been considered. These have been depicted in Figure 4.9 and consist of a solute-□ exchange (red dashed line), three instances of solute-□ pair dissociation/association (blue dashed lines), one solute-□ pair rotation and five other extended rotation jumps within the fourth neighbour shell of the solute atom (green dashed lines)[52]. Jumps beyond the 4th nearest neighbour shell of the solute atom were unaffected by the presence of the solute atom, and hence the $\Delta E_{\mathrm{m},Ni}$ value was used for these jumps. The activation energy barriers have been calculated from first principles using $3\times3\times3$ supercells and the results tabulated in Table 4.4. As an example, jump $2\rightarrow3$ means a vacancy jumping from a 2nd nearest neighbour position of the solute atom to a 3rd nearest neighbour position of the solute atom.

A value of 2.57 THz was used as the effective frequency ν^* for all jumps. The kMC simulations were performed as described in 2.2. All the atoms and the vacancy were tracked over time to calculate the diffusion coefficients.
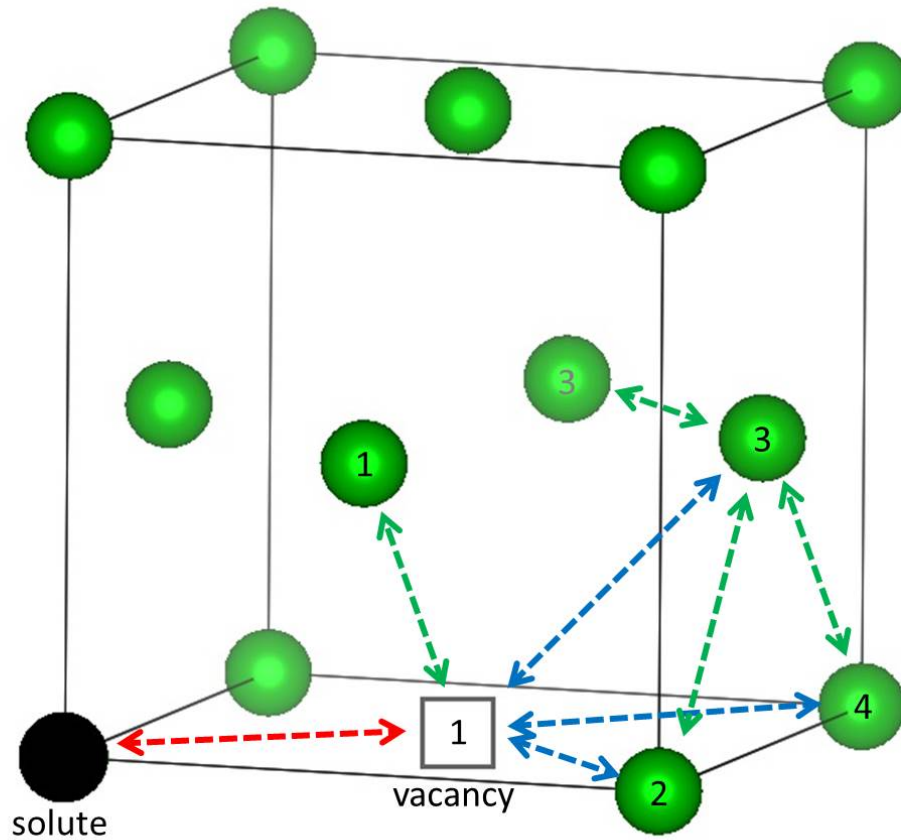
Figure 4.9: Possible jumps within 4th nearest neighbour distance of the solute atom (Image recreated from Schuwalow et al [52]). The green atoms are Ni atoms, the black atom is the solute atom and the square box represents the vacancy. The numbers on the atoms/vacancy represent their nearest neighbour distance with respect to the solute atom. Symmetrically equivalent jumps have not been shown.

Table 4.4: The migration barriers for solute-□ exchange and solute-□ extended rotation, dissociation and association used in the kinetic Monte Carlo simulations for dilute alloys

Solute	$\Delta E_{\mathrm{m},i}$(eV)	$\Delta E_{\mathrm{rot},i}$ (eV)						$\Delta E_{\mathrm{dis},i}$ (eV)			$\Delta E_{\mathrm{ass},i}$ (eV)		
	0→1	1→1	2→3	3→2	3→3	3→4	4→3	1→2	1→3	1→4	2→1	3→1	4→1
Ni$_{\mathrm{self}}$	1.08	-	-	-	-	-	-	-	-	-	-	-	-
Re	1.51	1.13	1.12	1.04	1.07	1.07	1.15	0.95	1.07	1.06	1.05	1.08	1.14
W	1.27	1.20	1.11	1.08	1.06	1.07	1.16	0.97	1.04	1.05	1.00	1.04	1.13
Ta	0.77	1.37	1.10	1.12	1.05	1.08	1.18	1.01	1.00	1.02	0.89	0.91	1.02

4.2.2 Ni-self diffusion coefficient and solute diffusion coefficients in Ni

The results for the Ni-self diffusion coefficient and solute diffusion coefficients in Ni for the temperature range 1173 K to 1573 K have been shown in Figure 4.10. These kMC simulations were run on 15×15×15 supercells, with 13500 lattice sites containing 1 solute atom and 1 vacancy. The kMC trajectory was divided into segments of 2000 jumps, and the diffusion coefficients obtained from kMC simulations were averaged over these segments. The results converged after approximately 10^7 jumps. Five different trials were run for each temperature and the arithmetic means of the diffusion coefficients from those trials were reported. The vacancy concentration of the simulation cell was 0.0074 at.% and hence the obtained diffusion coefficients were corrected as described in Equation (2.34) with the actual vacancy concentration in Ni at the temperature T given according to Equation (2.7). A $\Delta E_{f,i}$ value of 1.44 eV was used in all the cases.

Figure 4.10 also shows a comparison of the kMC results (symbols) to those previously obtained by Lidiard's model (lines). The diffusion trend was the same with Ta being the fastest diffuser, and Re being the slowest. The results for Ni and W almost overlap, while the results for Re and Ta are very close. Some of the differences can be attributed to the fact that the Lidiard's model (Equation 2.15) assumes a single value each for the $\Delta E_{rot,i}$ and $\Delta E_{dis,i}$ (or $\Delta E_{ass,i}$). However, the results in Table 4.4 show that there are considerable variations depending on which nearest neighbour position the vacancy is jumping to. For example, $\Delta E_{dis,Re}$ value for 1→2 dissociation is only 0.95 eV, while that for a 1→3 dissociation is 1.07 eV.

Since a number of diffusion barriers were considered in the kMC simulations, a decomposition of the solute diffusion coefficient D_i into the diffusion pre-factor, D_0^i and activation energy, Q_i terms could be non-trivial. These values were extracted from the kMC data in Figure 4.10 and have been tabulated in Table 4.5. A comparison to the data obtained from Lidiard's model, however shows a very good match for all the solutes. This shows that the application of the Lidiard's model in the investigated systems produces

Table 4.5: The D_0^i and Q_i terms extracted from the kMC data for self-diffusion and solute diffusion in Ni compared to the previously calculated results from Lidiard's model (LM) in the present work

Solute	Method	D_0^i (x10⁻⁷m²/s)	Q_i (eV)
Ni$_{\text{self}}$	kMC	11.33	2.53
	LM	10.1	2.52
Re	kMC	12.77	2.99
	LM	8.37	2.99
W	kMC	15.18	2.74
	LM	11.44	2.73
Ta	kMC	18.44	2.35
	LM	4.35	2.13

results of the same level of accuracy as the kMC simulations. The results were also in excellent agreement to those obtained by Schuwalow et al [52] from their kMC studies (see Table 4.3).

However, a small deviation was found in the case of Ta when compared to the results from Lidiard's model. This can be explained as follows. The solute correlation factor, f_i was included in the diffusion pre-factor term D_0^i as shown in Equation (2.16), however f_i is expected to affect the exponential term, Q_i as well, given its dependence on the various diffusion barriers. For Re and W, the solute correlation factor, f_i was found to be nearly unity for the temperature range considered, while for the self-diffusion of Ni, the correlation factor is a constant. For Ta, however, the f_i value varied between 0.3 to 0.4 in the temperature range considered (see Figure 4.4). Thus, a lower value of D_0^i was obtained for Ta from Lidiard's model. However, as seen from the kMC results, the contributions of f_i for the case of Ta have mostly entered the Q_i term and hence we have a higher Q_i value for Ta. It must be noted that a higher value of Q_i has the same effect on the solute diffusion coefficient as a lower value of D_0^i.

81
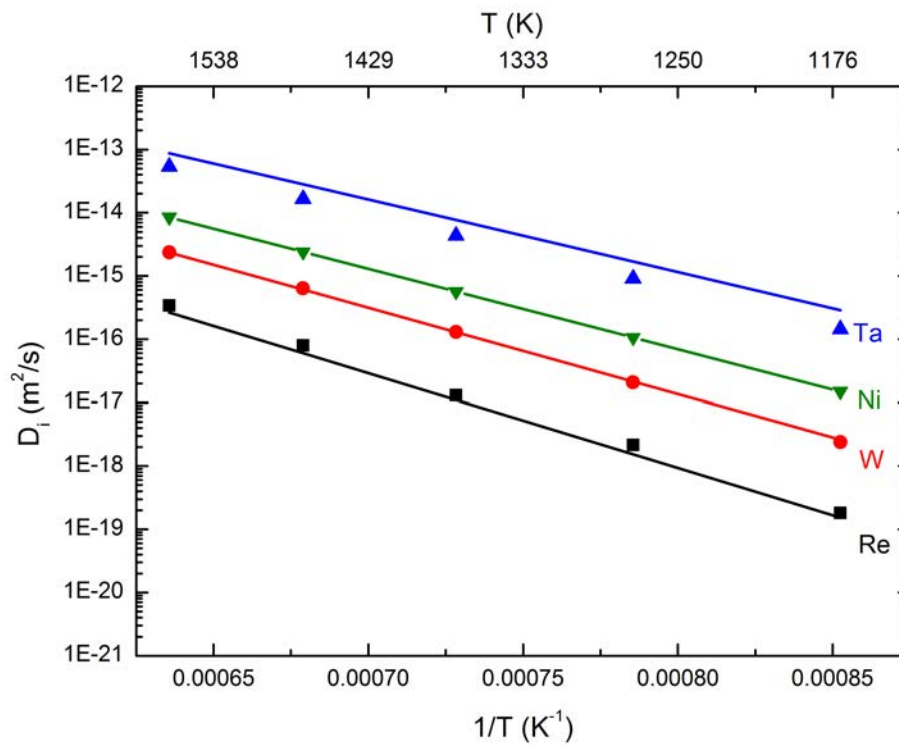
Figure 4.10: The self-diffusion coefficient in Ni and solute diffusion coefficients in Ni as a function of temperature. The symbols represent the results from kMC simulations, while the lines represent the results calculated from Lidiard's model

4.2.3 Vacancy diffusion coefficients in Ni

Similarly, the vacancy diffusion coefficients were also calculated in pure Ni and binary alloys of Ni under dilute limits. The solute concentration was varied by changing the size of the supercells used in the kMC simulation. The smallest kMC cell size was $3\times3\times3$, limiting the maximum solute concentration to about 0.9 at.%. Other cell sizes used were $3\times3\times4$, $3\times4\times4$, $4\times4\times4$, $5\times5\times5$, $6\times6\times6$ and $15\times15\times15$ yielding solute concentrations of 0.7 at.%, 0.5 at.%, 0.4 at.%, 0.2 at.%, 0.1 at.% and 0.0074 at.% respectively. Five kMC simulation runs were performed at 1373 K and the mean D_v was calculated. The results have been plotted in Figure 4.11. A D_v value of 3.46×10^{-11} m^2/s was obtained in pure Ni at 1373 K which matches exactly with the value predicted from analytical formulations (D_v^{Ni} is simply equal to $a^2\Gamma_{Ni}$). When compared to the results on D_v from Manning's model (see Figure 4.8), we can see that both predict that D_v for Re and W almost overlap, however the magnitude of the decrease in D_v is much greater from the kMC simulations. If we extrapolate the kMC results, a 5 at.% addition of Re or W should reduce the D_v by almost 30%. Similarly, a 5 at.% addition of Ta is expected to increase the D_v by about 20%.

4.2.4 Discussion

The analytical model for vacancy diffusion developed by Manning [64] indicated that small additions of slow-diffusing atoms in a host *fcc* lattice do not reduce the diffusion rate of vacancies substantially. In the case of slow diffusing solute atoms, the correlation factor for vacancy diffusion from Manning's formulation remains close to unity, and the decrease in Γ_v is minor. Manning's model suggests that vacancies would rarely have to exchange with the slow-diffusing solute atom, and even in the case the solute atoms were to be absolutely immobile due to a very high activation energy barrier for solute-$\square$ exchange, the resulting effect would only be as big as the percentage of solute content.

However, Manning's model was based on a number of simplifying assumptions and,
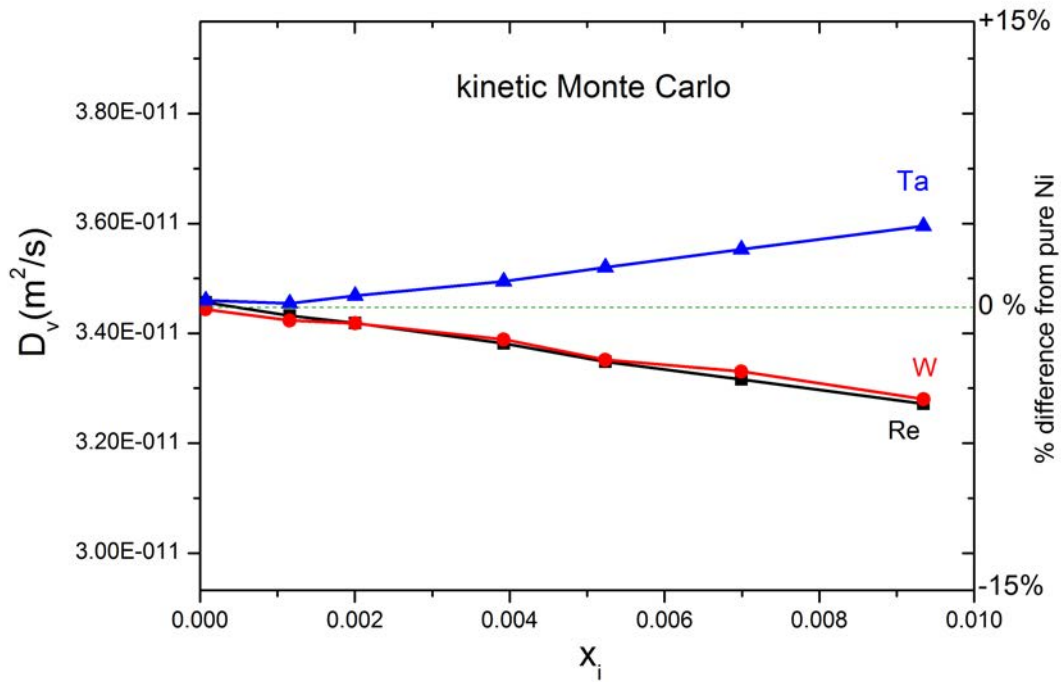
Figure 4.11: Vacancy diffusion coefficients in Ni as a function of solute concentration at 1373 K as calculated from the kMC simulations in dilute alloys

to get a more accurate description, kMC simulations were run to model the binary alloys in Ni. In the dilute regime, different migration barriers around a solute atom up to the 4th nearest neighbour distance were considered. Results from kMC simulations on dilute alloys showed a much greater impact of the solute atoms on the vacancy diffusion coefficients.

It was noteworthy that both the Manning's model as well as kMC simulations in the dilute regime predicted additions of Re and W to have the same effect on vacancy diffusion. While Re diffusion in Ni is almost an order of magnitude slower than W, it is more important to understand how they affect the Ni jump barriers in their vicinity, as the vacancy is more likely to exchange with Ni atoms. Indeed, looking at the extended jump barriers considered for the kMC simulations (see Table 4.4), it is clear that Re and W both have similar effects on the Ni jump barriers. In the seminal work of Giamei et al [11] on Re-effect, the observed improvements in creep lives of their model alloy was attained

by substituting W with Re. Thus, one would expect significantly different effects of these two solutes on D_v in Ni. However, it must also be noted that unlike W, Re partitions strongly to the γ phase, and thus the observed difference in creep strengthening could be simply a result of its higher concentration in the γ phase. It is therefore important to investigate how non-dilute alloys of Re in Ni affect the D_v. In non-dilute alloys, the solute - solute interactions will have to be taken into account to properly describe the diffusion processes.

CHAPTER 5

BINARY CLUSTER EXPANSION IN NICKEL-RHENIUM

The CASM (Cluster-Assisted Statistical Mechanics) code developed by Anton Van der Ven and coworkers [81, 82] was used for the cluster expansion of the configurational energy in the Ni-Re binary. A primitive *fcc* cell with configurational degree of freedom was given as the input to generate Ni-Re configurations in the entire binary composition space for maximum 10 atom supercells. 87 *fcc* supercells with a total of 2146 symmetrically distinct configurations were generated. Among these 2146 configurations, all possible configurations for supercells containing up to 4 atoms were selected while for bigger supercells, the configurations with Re concentration $\leq$ 20 at.% were selected. This was done to bias the cluster expansion to predict energies more accurately in the Ni-rich region. Thus, a total of 144 configurations were selected and their first principles energy was calculated. The cell volume, shape and all the internal degrees of freedom were relaxed. All calculations were spin-polarized. The electronic self-consistent loops were stopped when the total energy converged to within 10^{-6} eV and ionic positions were relaxed until all forces fell below 10^{-2} eV/Å. A $37 \times 37 \times 37$ k-point mesh was used for the primitive *fcc* cell. This has the same k-spacing in the reciprocal lattice [100] as a $5 \times 5 \times 5$ k-point mesh for a 108 atom *fcc* supercell which has been used for the calculations in the previous chapter. To maintain the same k-spacing, the k-mesh was automatically adjusted for the different configurations depending on their lattice vectors. Other details for the calculations were

same as given in subsection 3.3. On re-running the code, the formation energy per atom E_{form} of these 144 configurations were calculated according to the equation,

$$E_{\text{form}} = \frac{E_{\text{Ni}_x\text{Re}_y} - xE_{\text{Ni}} - yE_{\text{Re}}}{(x + y)} \tag{5.1}$$

where $E_{\text{Ni}_x\text{Re}_y}$ is the energy of the configuration Ni_xRe_y, x and y being the number of Ni and Re atoms respectively. E_{Ni} and E_{Re} are the energy of pure Ni and pure Re (calculated from first principles) used as reference states (see Table 5.2). Since all the configurations used in the present work were *fcc*, the energy for *fcc* Re was used as the reference. It must be noted that pure Re exhibits an *hcp* structure, however, in the Ni-rich regions, Re is expected to be present in an *fcc* solution of Ni. The formation energies of these configurations are shown in Figure 5.1. Amongst all the 144 configurations considered in Figure 5.1, the stoichiometric compound Ni$_4$Re at 20 at.% Re with a $D1_a$ structure was the lowest energy configuration with a formation energy of -0.073 eV. 101 of these configurations were used to fit the ECIs for the cluster expansion. Configurations with a formation energy greater than 0.03 eV were discarded as their formation is less likely energetically. Also, configurations towards the Ni-rich side were preferred. Specifically, the configurations with a Re concentration greater than 33 at.% were discarded. This was partly because the concentration of Re in the γ phase even in the third generation of Ni-based superalloys never goes beyond 10 at.% [115]. It is unlikely that even the local composition in the γ phase due to statistical fluctuations would go beyond 33 at.%. The calculation of the ECIs will be discussed in detail in the next section.

There have been previous investigations on the binary Ni-Re system using cluster expansion [32, 31]. Maisel et al [32] used the UNCLE package [116] to predict formation energies of 213,061 symmetrically inequivalent *fcc* structures of up to 20 atoms with 0 - 33 at.% Re by fitting their ECIs to a first principles database of 155 of those structures. The calculations were spin-polarized. Apart from pure Ni, $D1_a$-Ni$_4$Re with a formation energy of -0.058 eV was predicted to be a dominant ground-state structure, with a sizeable gap in its energy compared to all the other configurations used in their cluster expansion.

However, the calculated ECIs have not been reported. Monte Carlo simulations suggested the precipitation of $D1_a$-Ni$_4$Re in a lattice of Ni at low temperatures and remnant short range ordering at high temperatures.

He et al [31] have calculated two types of ECIs. The first were called 'fully renormalized interactions' and had a formulation similar to binding energies, while the other ECIs were dependent on composition, temperature and magnetism. The ECIs generated in the present work are composition independent and hence a comparison was again not possible. Formation energies > 0 were calculated for random alloys of Re in Ni in the dilute range with spin-polarized calculations indicating phase separation. However, with non spin-polarized calculations, formation energies < 0 were calculated indicating ordering in the Ni-Re system. They calculated the formation energy of $D1_a$-Ni$_4$Re as -0.062 eV using spin-polarized calculations and -0.106 eV using non spin-polarized calculations. It must be noted that *fcc* Ni and *hcp* Re were used as the reference states in their work. Other ordered compounds with compositions Ni$_{15}$Re and Ni$_8$Re were also found to be stable using non spin-polarized calculations, and hence a simple separation into *fcc* Ni and $D1_a$-Ni$_4$Re would not be expected. It can be argued that the non-magnetic state is representative of the high temperature behaviour in these alloys, given that Ni loses its ferromagnetic property above its Curie temperature. However, as mentioned in subsection 1.3.3, a complete consideration should also include the thermal magnetic excitations [31]. Thus it remains inconclusive whether spin-polarized or non spin-polarized calculations represent the Ni-Re system better.

Levy et al [117] used high-throughput first principles calculations to predict the formation of stable ordered compounds in Ni-Re alloys amongst other binary alloys of Re. Apart from $D1_a$-Ni$_4$Re, whose formation energy was calculated as -0.064 eV they also found the stable $D0_{19}$-NiRe$_3$ structure with a formation energy of -0.115 eV using spin-polarized calculations. However, $D0_{19}$ is an *hcp* based structure in the Re-rich side of the Ni-Re binary, and hence could not be accounted in the cluster expansion described in the present work.
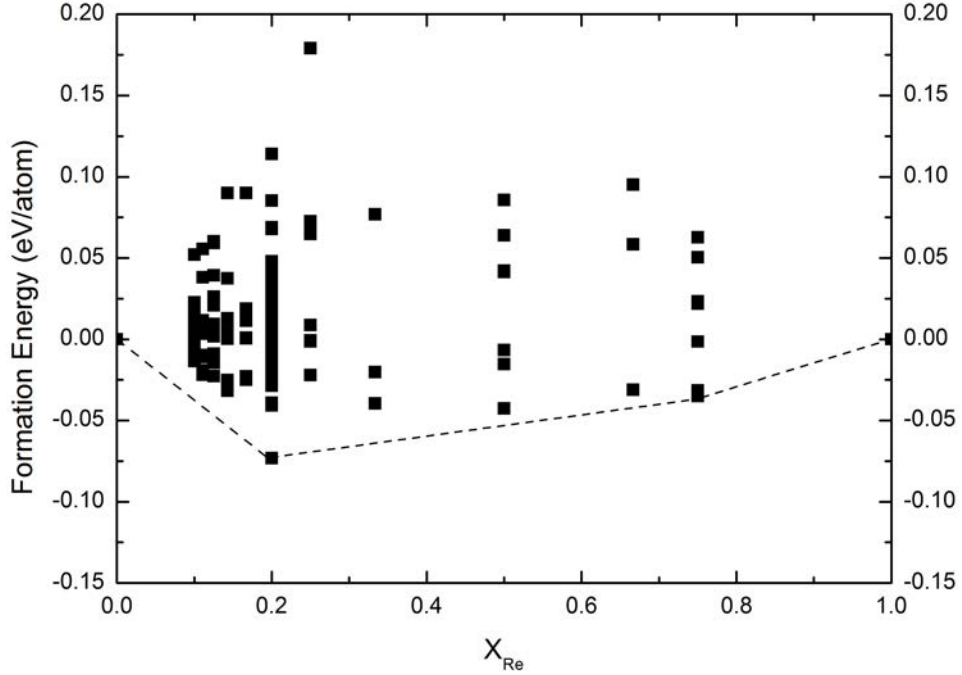
Figure 5.1: The formation energy calculated for the 144 Ni-Re configurations. 101 of these configurations were used in the cluster expansion to get the ECIs.

5.1 Effective cluster interaction coefficients

Clusters of maximum 3 atoms within a sphere radius of 6 Å were considered in the fitting of the effective cluster interaction coefficients. This meant a total of 27 possible clusters (1 empty cluster (V_0), 1 point cluster (V_α), 5 pair clusters (V_β) and 20 triplet clusters (V_γ)) were available for fitting the ECIs to the formation energy of the 101 configurations in the dataset. The fitting was done using the ecifit code incorporated within CASM. The ecifit code is a least squares fitting script combined with an implementation of a genetic algorithm [118] for determining the optimal set of clusters to include. Several genomes (set of clusters to include) were selected and their fitness was calculated using the cross validation score, CV [83] given as,

$$CV = \frac{1}{N} \sum_{i=1}^{N} (\tilde{E}_i - E_i)^2 \tag{5.2}$$
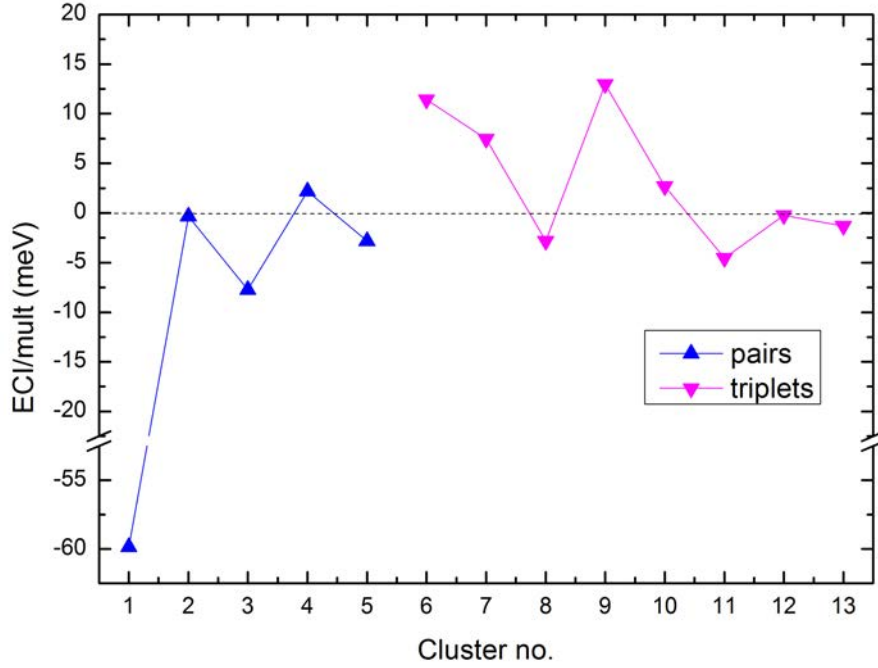
Figure 5.2: ECI/multiplicity for pair and triplet clusters

where E_i is the formation energy of configuration i, and $\tilde{E}_i$ is the energy predicted for configuration i by the least squares fit obtained with configuration i excluded. N is the number of configurations in the dataset. Genetic algorithm is inspired by the rule of evolution. The low performing genomes are culled and the high performing genomes are mated to produce new generation of genomes.

The ECIs were optimised after about 20 such generations. Sufficient accuracy was obtained when using a total of 15 clusters. The root mean square error between first-principles energies and cluster expanded energies for all 101 structures used in the fit was 5.7 meV per atom and the CV score was 7.3 meV per atom. This is a good fit considering the fact that an rms error value of 5.6 meV per atom was obtained by Van der Ven et al [84] using their ECIs calculated for Al-Li alloys.

Table 5.1: The calculated effective cluster interaction coefficients (ECIs)

Clusters		ECIs (meV)	multiplicity	ECIs/multiplicity (meV)
empty (V_0)		-59.561888	1	-59.561888
point (V_α)		286.882444	1	286.882444
pairs(V_β)	1	-359.116693	6	-59.852782
	2	-0.975073	3	-0.325024
	3	-92.888637	12	-7.74072
	4	13.122478	6	2.18708
	5	-33.982001	12	-2.831833
triplets(V_γ)	6	91.405618	8	11.425702
	7	89.353006	12	7.446084
	8	-22.588647	8	-2.823581
	9	77.833137	6	12.972189
	10	128.563476	48	2.678406
	11	-54.525616	12	-4.543801
	12	-11.071775	48	-0.230662
	13	-31.095871	24	-1.295661
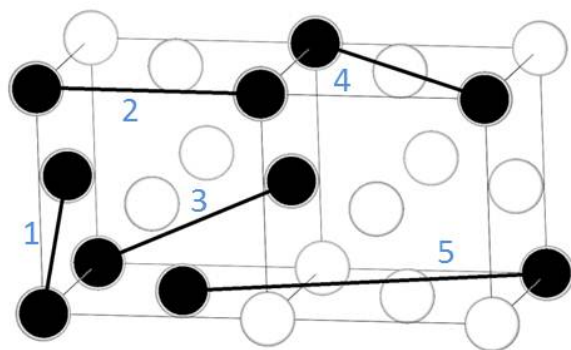
(a) pair clusters 1 to 5
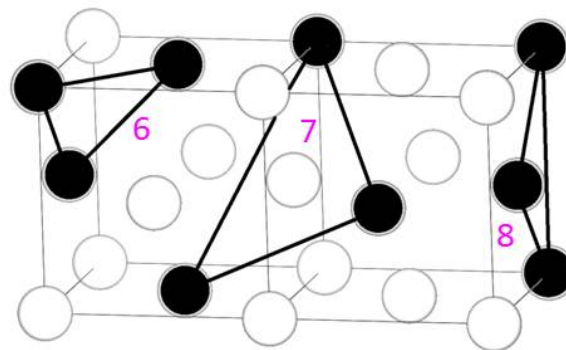
(b) triplet clusters 6 to 8
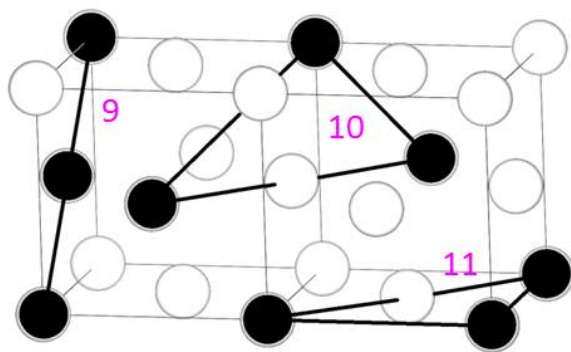
(c) triplet clusters 9 to 11
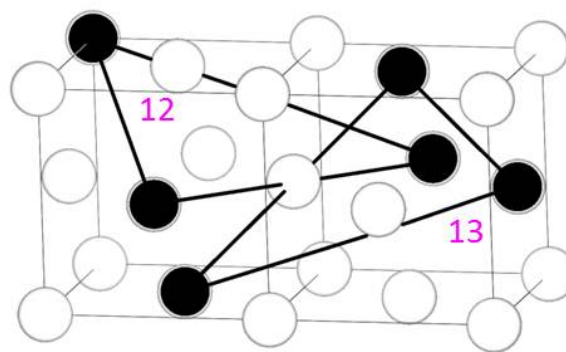
(d) triplet clusters 12 and 13

Figure 5.3: The pair and triplet clusters used in the ECI fitting

Table 5.1 shows the fitted ECIs for the Ni-Re case. Five pair clusters (V_β) include the 1st five nearest neighbour pairs. Eight triplet clusters (V_γ) have also been included. These pair and triplet clusters have been numbered 1 to 13 and Figure 5.3 represents these clusters. The empty cluster (V_0) is just a constant term used in the fitting while the point cluster (V_α) is the single atom cluster. Table 5.1 also shows the multiplicity of these clusters. For example, the pair cluster number 1 has a multiplicity of 6, meaning there are 6 symmetrically equivalent clusters in different orientations. This is expected as an atom in an *fcc* lattice is paired to twelve 1st nearest neighbours, and each of these pairs is shared by 2 atoms. Hence, the multiplicity is 6. The ECIs/multiplicity (see Figure 5.2) have also been calculated as this is more suitable in our kinetic Monte Carlo code to model the energy of the Ni-Re alloys. As described earlier, an occupation variable (σ_i) value of +1 represents a Ni atom, while -1 represents a Re atom. It must be noted that the CASM code cluster expands the formation energy and not the total configurational energy. One can calculate the formation energy first from the obtained ECIs, and then the configurational energy can be deduced by rearranging the Equation (5.1).

The pair cluster (V_β) number 1 has a significantly larger value compared to the rest. A large negative value also indicates that the energy predicted for a Ni-Re system will lower significantly when there are two Ni atoms or two Re atoms as 1st nearest neighbour pairs. When a Ni atom is surrounded by Re atoms in its 1st nearest neighbour shell, or vice-versa, there is an increase in the total energy. All other pair clusters except number 4 have negative values. Thus most of the other Re-Re pairs also lower the overall energy of the system, albeit to a lesser degree. This should mean that two Re atoms would prefer to sit next to one another in a 1st nearest neighbour position compared to any other configuration. On the other hand, the triplet cluster (V_γ) number 6 has a positive value. Thus, if there is a Re 1st nearest neighbour triplet, the occupation vector ($\vec{\sigma}$) becomes -1, and the energy of the system is lowered again. However, if the cluster consists of a pair of Re atoms, and a single Ni atom, then ($\vec{\sigma}$) becomes +1, and the energy of the system increases. Thus, strictly speaking, the ECIs cannot be evaluated separately, as the value

Table 5.2: The first principles energy and energy predicted from cluster expansion of Ni-Re by the CASM code for pure Ni and pure Re

Reference state	FP energy (eV)	CE predicted energy (eV)
Ni	-5.46864	-5.4473
Re (fcc)	-12.3403	-13.4285

of one depends on the others.

Table 5.2 presents a comparison of the first principles energy and the energy predicted from cluster expansion using the above ECIs for pure Ni and pure Re (fcc). One can see that the match is very good for Ni, while there is a deviation of about 1 eV in the case of Re. This can be explained as only Ni-rich configurations were used to fit the ECIs. Nevertheless, we expect accurate prediction of the configurational energies in the composition range of interest (< 10 at. % Re). It must be clarified that the first principles energies for pure Ni and Re have been used to calculate the formation energies in Equation (5.1).

The generated ECIs in the present work were used to calculate the Re-Re pair binding energies as a function of distance and were compared to the binding energies calculated directly from first principles with spin-polarization. This has been shown in Figure 5.4. The results differ by a magnitude of about 0.2 eV, but the predicted trend is very similar up to 5th nearest neighbour position. Considering that the maximum separation of atoms in the clusters included in the fit was 5th nearest neighbours, this is expected. The match improves from Re nearest neighbour pairs to triplets to quadruplets, as shown in Table 5.3. This means that the generated ECIs are expected to predict the energies for higher concentration of Re in Ni with a higher accuracy.

Also shown are the results of Mottura et al [29] for non-spin polarized calculations. It is noteworthy how the binding energy becomes more repulsive with the increase in the number of Re atoms in the cluster, which contradicts the results from spin-polarized calculations. This effect was also observed previously by He et al [31]. This means that the inclusion of magnetism in the calculations can have dramatic consequences to the
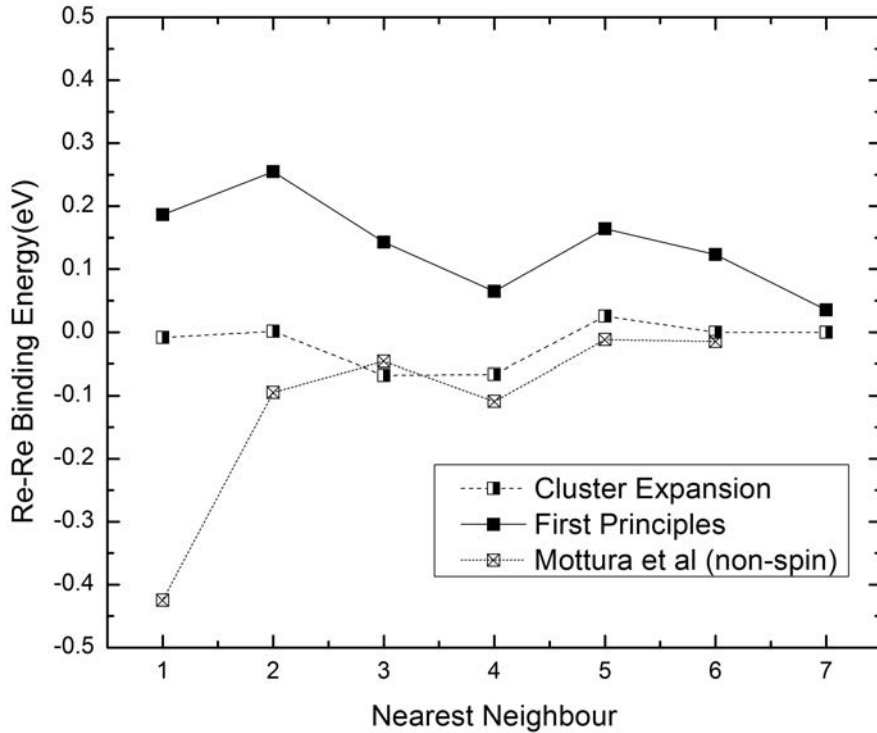
Figure 5.4: Comparison of the Re-Re binding energies from first principles, predictions from cluster expansion and non-spin polarized results from Mottura et al [29]

phase equilibrium in Ni-Re alloys. While the work of Mottura et al [29] suggests that Re should be distributed randomly in a solution with Ni, the present work suggests that a phase separation should be the likely scenario. The results from the cluster expansion performed by Maisel et al [32] including spin-polarization in their calculations however predict ordering in the Ni-Re system with the precipitation of $D1_a$-Ni$_4$Re.

Table 5.3: Comparison of the binding energies for different Re clusters from first principles, predictions from cluster expansion and non-spin polarized results from Mottura et al [29]

Re cluster	FP energy (eV)	CE predicted energy (eV)	Mottura et al [29]
pair	0.186	-0.008	-0.425
triplet	0.306	0.066	-1
quadruplet	0.379	0.315	-1.65

95
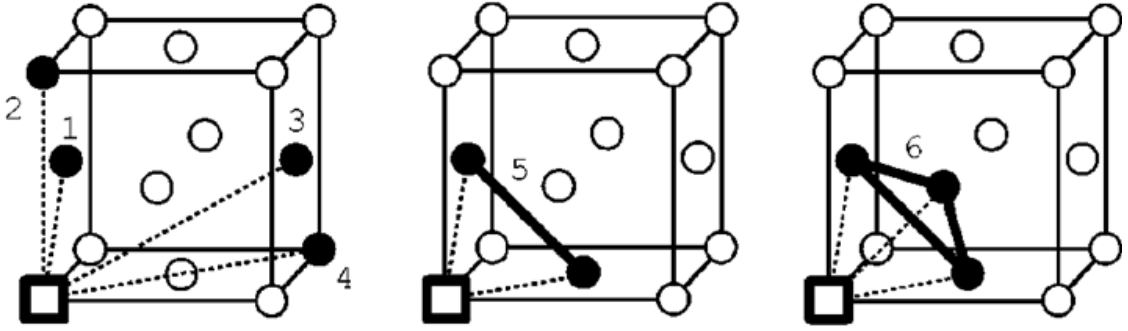
Figure 5.5: The clusters used for expansion of the effective vacancy formation energy (adopted from Van der Ven et al [84])

5.2 Effective vacancy formation energy

The presence of vacancies was accounted by the effective vacancy formation energy as described in subsection 2.3.1. A local cluster expansion of the EVFE was done around one vacancy. Unlike the binary cluster expansion, where supercells of maximum 10 atoms were used, here first principles energy calculations were run on $3\times3\times3$ supercells to avoid the vacancy-vacancy interaction across the periodic images. 26 different configurations were used and three calculations were performed on each of them, one with a vacancy at a lattice site $(E_i^v(\vec{\sigma}))$ and two others with a Ni $(E_i^{Ni}(\vec{\sigma}))$ and a Re $(E_i^{Re}(\vec{\sigma}))$ atom each replacing that site. Thus 78 different calculations were performed in total. Configurations with upto 36 Re atoms (33 at.%) were considered in the calculations. For some of the non-dilute compositions considered, the ionic relaxation was terminated when the forces fell below 0.02 eV/Å. Also, a $4\times4\times4$ k-mesh was used for these calculations.

The selection of clusters and the fitting of the corresponding ECIs for binary cluster expansion of the configurational energy in Ni-Re was performed using a genetic algorithm as incorporated in the CASM code. However, the option of local cluster expansion for the prediction of EVFE was not available with CASM. Hence, in this case, clusters as shown in Figure 5.5 were adopted from the work of Van der Ven et al [84]. Four point clusters up to the 4th nearest neighbour distance, and the 1st nearest neighbour pair and triplet clusters around a vacancy were considered. LECIs corresponding to these clusters were fit using multiple regression and the results are shown in Figure 5.6 and also
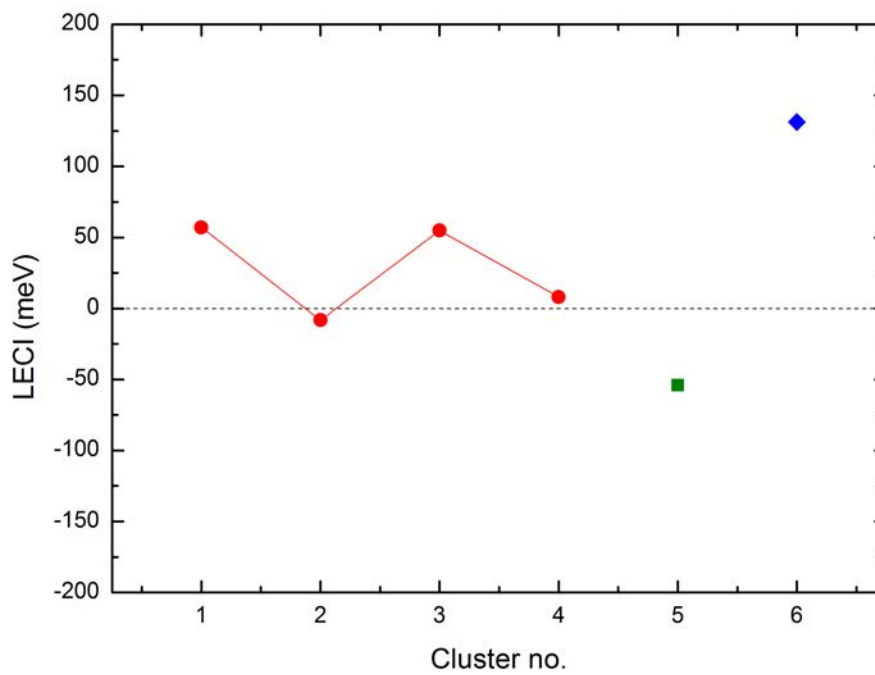
Figure 5.6: The calculated local effective cluster expansion coefficients for cluster numbers 1 - 6. The corresponding clusters have been shown in Figure 5.5. Red, green and blue symbols represent point, pair and triplet clusters around a vacancy

Table 5.4: The calculated local effective cluster expansion coefficients (LECIs)

Cluster No.	LECIs (meV)
1	57.14
2	-8.23
3	54.88
4	8.06
5	-54.13
6	131.21

tabulated in Table 5.4. LECIs representing different clusters have been given different colours in Figure 5.6, with red, green and blue symbols representing point, pair and triplet clusters around a vacancy respectively. It must be noted that the treatment of the cluster expansion is slightly different here, and instead of considering the occupation variables for all the atoms around a vacancy, the EVFE was fit to the number of Re atoms, Re pairs and Re triplets around a vacancy. The constant term was set as 10.2413 eV, which was the EVFE in pure Ni. A root mean square error of 0.083 eV was obtained. This is clearly higher when compared to the rms error for the binary CE. In order to assess the quality of the obtained fit, the calculated LECIs have been used to predict the Re-□ binding energies as shown in Figure 5.7. The predicted values match well with the Re-□ binding energies calculated directly from first principles. A discrepancy in the trend was observed after the 4th nearest neighbour distance. This was expected since interactions only upto 4th nearest neighbours were included in the EVFE fit. However, given the reproducibilty of the binding energies otherwise, we expect good results for the EVFE predictions.

5.3 Kinetically resolved activation energy barriers

The kinetically resolved activation barriers were calculated for a number of vacancy pathways with different atomic environments. On top of the barriers considered for the dilute
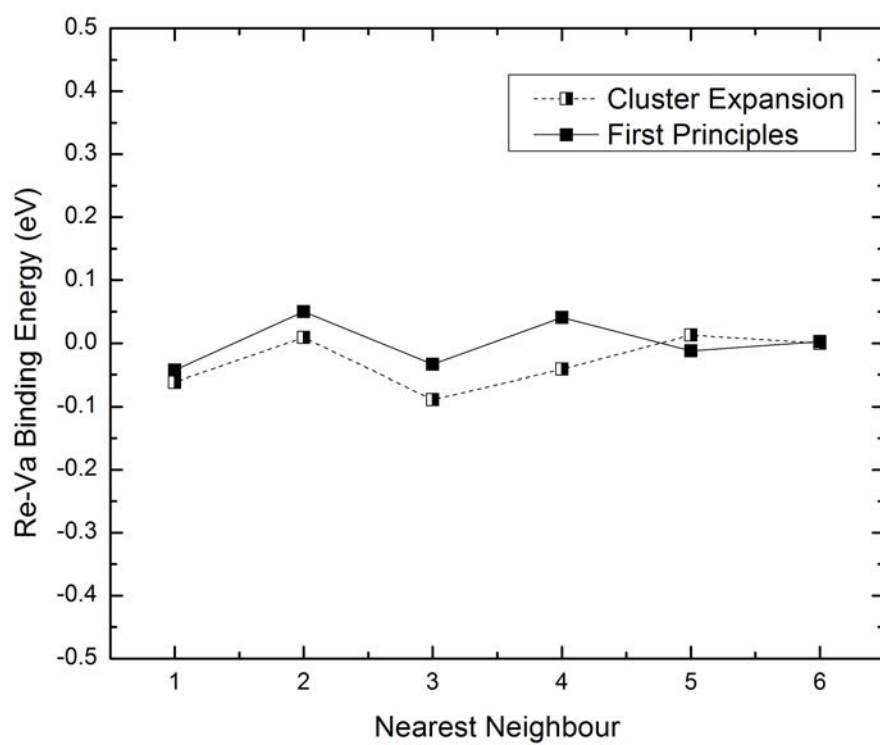
Figure 5.7: Comparison of the Re-□ binding energies from first principles with predictions from local cluster expansion. The scale is kept similar to Figure 5.4.

Table 5.5: KRAs calculated for the various Re jumps

Type of Re jump	ΔE_{m}(eV)	ΔE_{KRA} (eV)
S+R	1.604	1.604
S+D	1.463	1.512
S+A	1.560	1.512

alloys of Ni-Re in Section 4.2.1, other barriers based on the fourteen-frequency model [51] were considered. These have been illustrated in Figures 5.8, 5.9 and 5.10 (S stands for vacancy-solute exchange, while R, D and A stand for vacancy-solute pair rotation, dissociation, and association respectively). The barriers were calculated using the climbing image nudged elastic band method for the forward and the reverse jumps and the KRA was deduced from the two (see Tables 5.5 and 5.6).

Re jumps
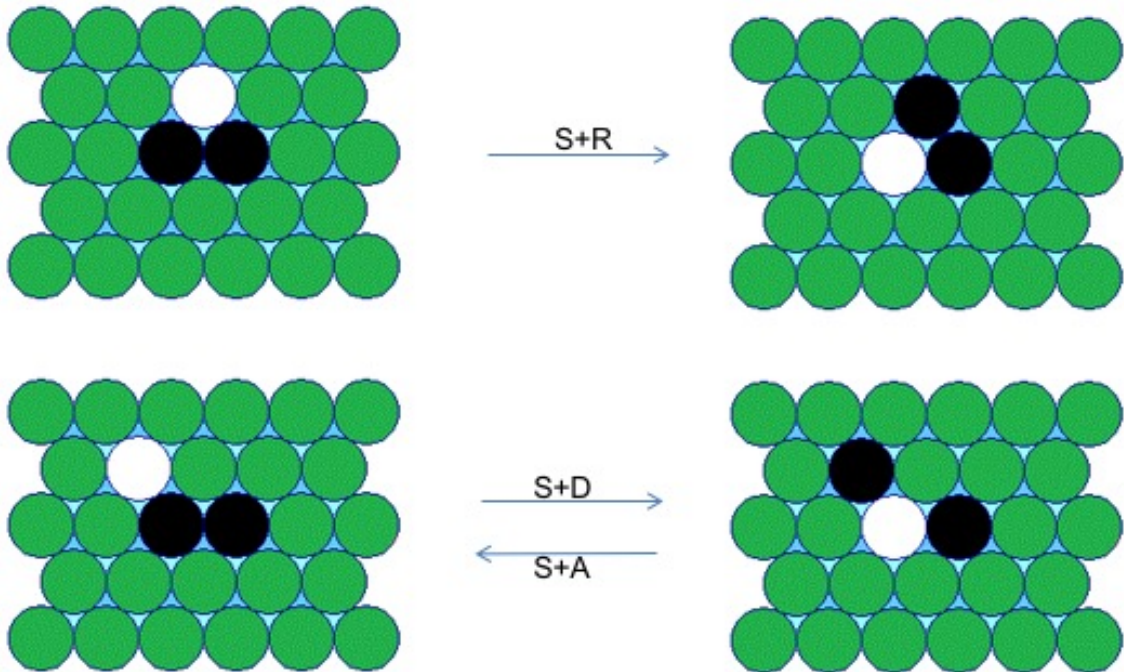
Figure 5.8: Configurations used for Re jumps

Ni jumps

When the Re atoms are paired
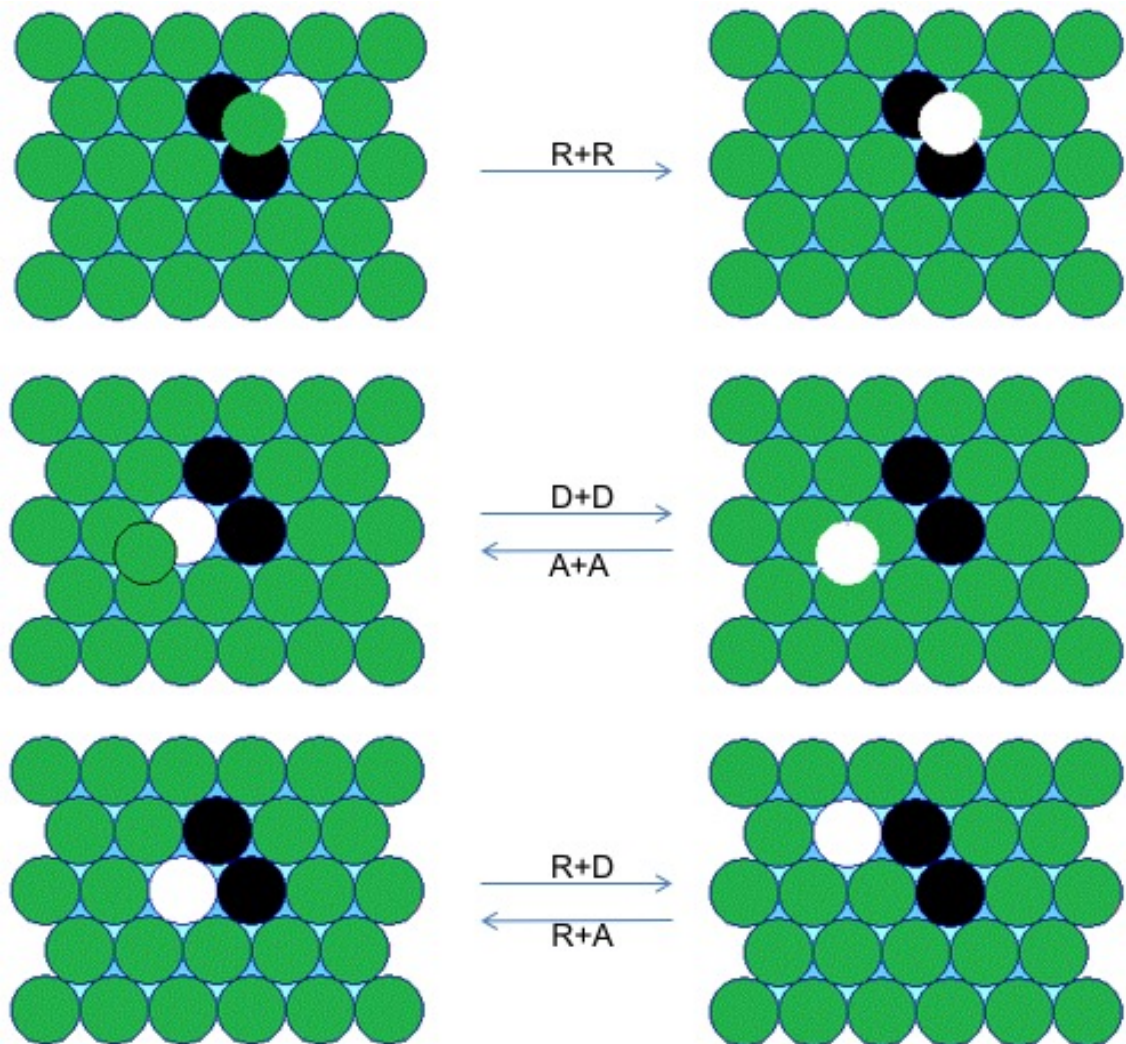
Figure 5.9: Configurations used for Ni jumps when the Re atoms are paired

When the Re atoms are unpaired
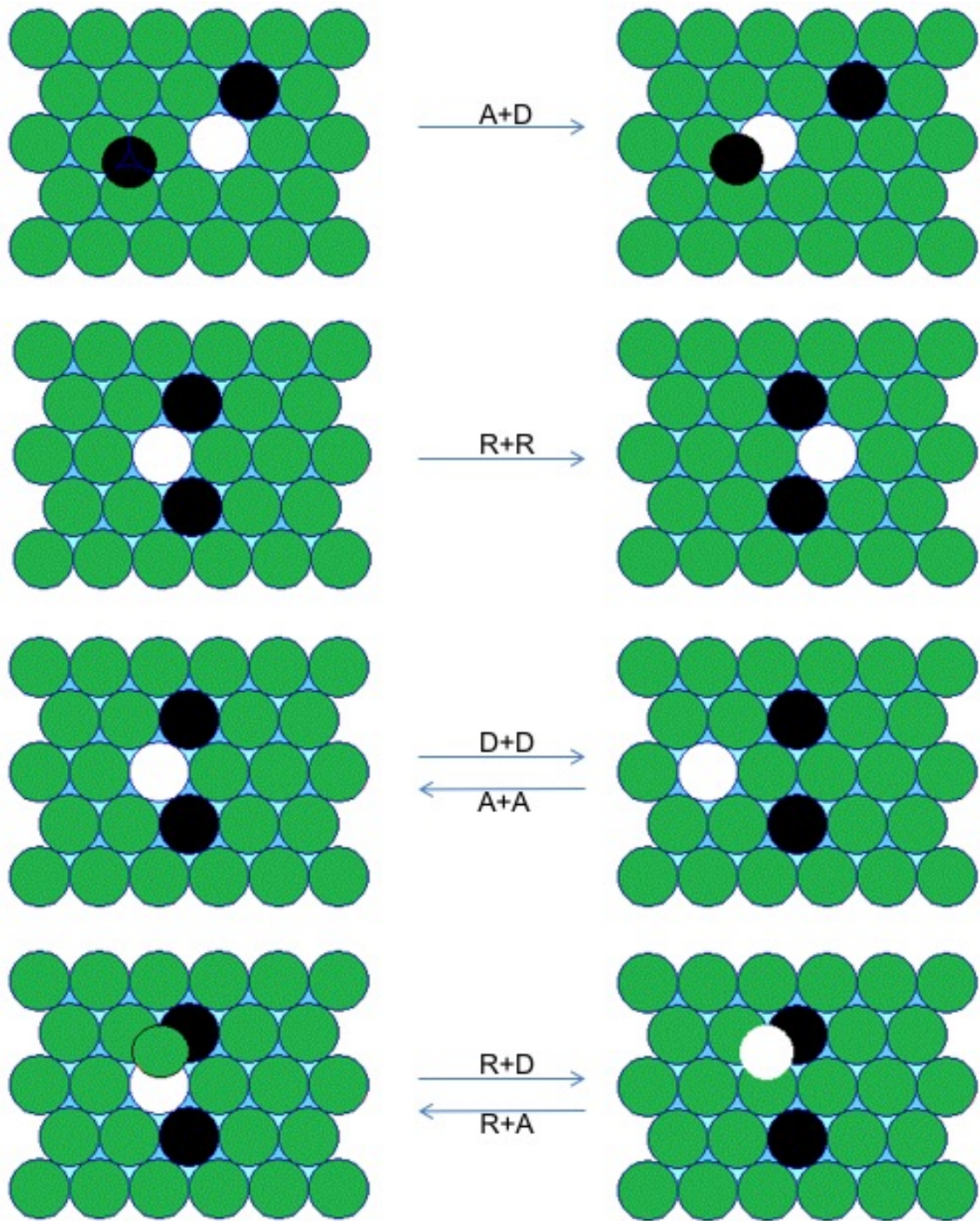
Figure 5.10: Configurations used for Ni jumps when the Re atoms are unpaired

Table 5.6: KRAs calculated for the various Ni jumps

	Type of Ni jump	ΔE_m(eV)	ΔE_KRA (eV)
paired Re atoms	R+R	1.287	1.287
	D+D	1.046	1.067
	A+A	1.088	1.067
	R+D	1.189	1.169
	R+A	1.150	1.169
unpaired Re atoms	A+D	1.067	1.067
	R+R	1.361	1.361
	D+D	1.069	1.105
	A+A	1.141	1.105
	R+D	1.112	1.147
	R+A	1.181	1.147

KRAs were also described using a local cluster expansion according to Equation (2.39). From definition, KRAs are independent of the direction of the jumping atom and they represent the saddle point energy normalised to the arithmetic mean of the energies of the two end points. Thus the occupation variables defined for the local cluster expansion for KRAs should be centred about the saddle point, in contrast to the local cluster expansion of EVFE, where the occupation variables were defined in relation to their distance from the vacancy. However, the saddle point does not overlap on a lattice site and lies approximately halfway between the hopping atom and the vacancy. Thus, the set of lattice positions at a certain distance from the hopping atom, and the set of lattice positions at the same distance from the vacancy are considered equivalent and are clubbed together. For example, the lattice positions which are 1st nearest neighbours to either the hopping atom or the vacancy are considered equivalent.

For simplification, the KECIs in the present work were fit to the number of Re atoms

around a saddle point instead of considering the occupation variables of all the atoms. It was assumed that the presence of Re atoms in the combined 1st nearest neighbour shell of the hopping atom and the vacancy affect the barriers, while those beyond have no role to play. Four different point clusters were included in the present case. For a Ni atom performing a jump, the KRA was given by,

$$\Delta E_{KRA}^{Ni} = 1.08 + 0.108 \times N_{Re}^{1,1} - 0.080 \times N_{Re}^{1,2} - 0.004 \times N_{Re}^{1,3} + 0.022 \times N_{Re}^{1,4} \quad (5.3)$$

To explain this, Figure 5.11 should be referred which shows an fcc {111} plane with an atom (black) about to perform an exchange with a vacancy (□). There are a combined total of 18 atoms which are 1st nearest neighbour to either the atom or the vacancy. $N_{Re}^{1,1}$ represents the number of Re atoms which are 1st nearest neighbours to both the hopping atom or the vacancy (blue positions), $N_{Re}^{1,2}$ represents the number of Re atoms which are 2nd nearest neighbours to either the hopping atom or the vacancy (yellow positions), $N_{Re}^{1,3}$ represents the number of Re atoms which are 3rd nearest neighbours to either the hopping atom or the vacancy (red positions) and $N_{Re}^{1,4}$ represents the number of Re atoms which are 4th nearest neighbours to either the hopping atom or the vacancy (green positions). Thus depending on which of these categories the Re atoms in the 1st nearest neighbour shell belong to, we describe our KRA. If there are no Re atoms surrounding the jumping Ni atom, the KRA value is 1.08 eV from Equation (5.3), which is also the expected energy barrier in pure Ni. Using the KECIs given in Equation (5.3), an rms error of 0.048 was calculated which was similar to the rms error calculated for EVFE.

For a Re atom performing a jump, the KRA was simply given by,

$$\Delta E_{KRA}^{Re} = 1.505 + 0.099 \times N_{Re}^{1,1} + 0.007 \times N_{Re}^{1,2} + 0.007 \times N_{Re}^{1,3} + 0.007 \times N_{Re}^{1,4} \quad (5.4)$$

This completes our list of input parameters required for the kinetic Monte Carlo
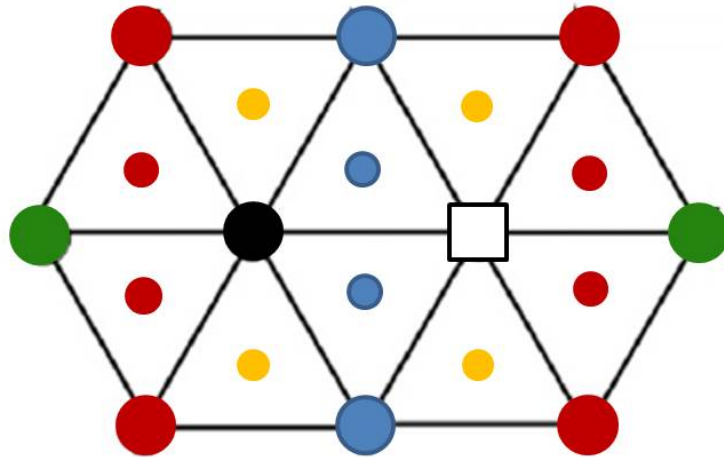
Figure 5.11: The *fcc* {111} plane showing an atom in black next to a vacancy surrounded by other atoms in the 1st nearest neighbour shell. The colour of these atoms represent their relationship to the black atom and the vacancy. Atoms out of the plane have been shown smaller in size.

simulation to study the Ni-Re alloy in the non-dilute regime.

CHAPTER 6

DIFFUSION IN NON-DILUTE NICKEL-RHENIUM ALLOYS

The vacancy diffusion coefficients in non-dilute Ni-Re alloys based on the input parameters in Chapter 5 was calculated using the kMC code. The Ni as well as the Re tracer diffusion coefficients were also calculated. The code is capable of handling an *fcc* simulation cell of size $\geq 4 \times 4 \times 4$ with one vacancy for any desired composition, temperature and duration of kMC simulation.

On running the code, the required simulation cell is generated and the lattice sites are randomly populated with Ni and Re atoms and a vacancy according to the given composition. Occupation variables (σ_i) +1, -1 and 0 represent a Ni atom, a Re atom and the vacancy respectively. Periodic boundary condition is applied to the simulation cell and the nearest neighbour relationships are calculated for each lattice position. The initial energy of the simulation cell is calculated according to the Cluster Expansion method as described in section 2.3.1 using the ECIs and the EVFE values in Chapter 5, while for every subsequent kMC step, the energy of the simulation cell is adjusted according to the changes in the nearest neighbour environment of the vacancy and the jumping atom.

Given the initial configuration of the system, the activation energy barriers ΔE_m corresponding to the 12 possible 1st nearest neighbour vacancy jumps are obtained using the KRAs calculated in Chapter 5. One of these 12 possible jumps is carried out (see section 2.2) according to the magnitude of a generated random number, after which the

atomic positions are readjusted and the time is updated. The vacancy diffusion coefficient is calculated according to Equation (2.33). It is noteworthy that instead of tracking the atomic coordinates throughout the simulation, only the displacements are calculated for every individual atom and the vacancy from their initial and final position within a kMC segment. The mean squared displacements are calculated over all the Ni atoms and Re atoms to obtain their diffusion coefficients according to Equation (2.34). The actual vacancy concentration, x_{v} in pure Ni, corresponding to a $\Delta E_{\mathrm{f},Ni}$ value of 1.44 eV (see Table 4.3) has been used in Equation (2.34) for simplicity.

The results presented in this chapter have been calculated for $15 \times 15 \times 15$ supercells for five different temperatures (1173 K - 1573 K).

6.1 Error propagation in the calculated diffusivities

The predicted results for diffusivities in the non-dilute systems include the error in the energy data that are fed as input to the kMC simulations. An analysis of the error propagation is therefore necessary to understand the impact of these errors on the final results. Combining Equation (2.37) and Equation (2.40), the activation energy barrier ΔE_a can be given as,

$$
\begin{aligned}
\Delta E_a &= \Delta E_{KRA} + \frac{1}{2} \left(E_f - E_i \right) \\
&= \Delta E_{KRA} + \frac{1}{2} \left[\left(\Delta E_f^{\mathrm{eff}} + \frac{1}{2} \left[E_f^{\mathrm{Ni}}(\vec{\sigma}) + E_f^{\mathrm{Re}}(\vec{\sigma}) \right] \right) - \left(\Delta E_i^{\mathrm{eff}} + \frac{1}{2} \left[E_i^{\mathrm{Ni}}(\vec{\sigma}) + E_i^{\mathrm{Re}}(\vec{\sigma}) \right] \right) \right]
\end{aligned}
\tag{6.1}
$$

where ΔE_{KRA} is the Kinetically Resolved Activation Barrier, while E_f and E_i are the energy of the final and the initial state of the jump. Also, ΔE^{eff} is the effective vacancy formation energy and $E^{\mathrm{Ni}}(\vec{\sigma})$ and $E^{\mathrm{Re}}(\vec{\sigma})$ are the energies when the vacancy is replaced by a Ni atom or a Re atom, and are calculated from the binary Cluster Expansion. Again a

careful examination of Equation (6.1) tells us that in case of a Ni jump, $E_i^{\mathrm{Ni}}(\vec{\sigma}) = E_f^{\mathrm{Ni}}(\vec{\sigma})$ and in the case of a Re jump, $E_i^{\mathrm{Re}}(\vec{\sigma}) = E_f^{\mathrm{Re}}(\vec{\sigma})$ and hence these terms get cancelled. Furthermore, the remaining $E_f^{\mathrm{Re}}(\vec{\sigma})$ - $E_i^{\mathrm{Re}}(\vec{\sigma})$ term (or $E_f^{\mathrm{Ni}}(\vec{\sigma})$ - $E_i^{\mathrm{Ni}}(\vec{\sigma})$ term in the case of a Re jump) signify the change in energy due to a Ni-Re swap, while the position of every other atom remains unchanged. Root mean square errors of 0.048 eV and 0.083 eV were calculated for the KRAs and EVFEs respectively, while a value of 0.0057 eV/atom was calculated for the formation energies in the binary CE. This would mean that for a $15 \times 15 \times 15$ *fcc* supercell with 13500 atoms, the uncertainty in the total energy predicted by the CE can be of the order of 77 eV. However, given the terms in the initial and final states in Equation (6.1) remains the same except for a Ni-Re swap, the systematic errors get cancelled and the uncertainty in the predicted energy from the CE should be negligible, given its small rms error when compared to the rms errors for KRA and EVFE. Thus, to a first approximation, the uncertainty in ΔE_a can be given as [119],

$$\sigma_{(\Delta E_a)} = \sqrt{(\sigma_{(\Delta E_{KRA})})^2 + 2 \times 0.5^2 \times (\sigma_{(\Delta E^{eff})})^2} = \pm 0.076\mathrm{eV} \qquad (6.2)$$

According to Equation (2.11), this should translate to a relative uncertainty in jump frequency Γ of [119]

$$\frac{\sigma_{(\Gamma)}}{\Gamma} = \left\{ \frac{\sigma_{(\Delta E_a)}}{k_{\mathrm{B}}T} \right\} \qquad (6.3)$$

Thus, the relative uncertainty in jump frequency is a function of temperature alone. This relative uncertainty in jump frequency is mostly random in nature and one would expect its effect on the calculated diffusivities to become smaller if the kMC simulations are run for a long time, as is the case in the propagation of random errors under any experimental setup. However, analysis of error propagation in the present case is not straightforward. In addition, one should point out that there might be a component of systematic error in the evaluation of the barriers, which might have a considerable effect on the results as resulting inaccuracies would not reduce with longer simulation times.

Looking at Equation (2.33), error propagation in the calculated diffusion coefficients

is a combination of the error propagation in t (time elapsed) and the error propagation in $\langle R^2(t) \rangle$ (squared displacement). The cumulative jump frequency for the 12 possible vacancy jumps enter as the reciprocal term in the time step Δt of the kinetic Monte Carlo simulation. The relative uncertainty in the time step can be given as [119],

$$\frac{\sigma_{(\Delta t)}}{\Delta t} = \sqrt{12}\frac{\sigma_{(\Gamma)}}{\Gamma} \tag{6.4}$$

The kMC simulations in the present work for the case of non-dilute alloys have been run for 15 million steps and if one were to look at the relative uncertainty in the diffusivity coming from the error in time elapsed alone, these are expected to get smaller with the duration of the kMC simulation.

However, the errors in jump frequency would also mean that there is a degree of uncertainty in the selection of the vacancy pathway in each kMC step. This implies that the calculated trajectories of the atoms and vacancies and also their calculated displacements have a degree of uncertainty. It is difficult to determine if this error is random in nature and is expected to fade out over the course of a kMC simulation or if the error is expected to accumulate. To the best knowledge of the author, there were no previous works in the literature calculating the error propagation in kMC simulations. This is a problem in vector mathematics and is beyond the scope of this work.

6.2 Results in pure Ni

The pure Ni energy was calculated as -5.4778 eV per atom (pure Re energy was calculated as -13.39795 eV per atom) from the implementation of the cluster expansion in the kMC code. This value was constant and did not vary with the simulation cell size. However, this is 0.0305 eV lower than that calculated by the CASM code (see Table 5.2). We believe that this difference was due to the difference in the levels of accuracy used in the two calculations. We used double precision numbers in our kMC code and used the ECIs (see Table 5.1) without rounding off any digits. The effective vacancy formation

Table 6.1: The calculated total energies and vacancy formation energies in pure Ni, $\Delta E_{\mathrm{f},Ni}$ for different simulation cell sizes (see Equation (2.9))

Simulation cell size	Energy (eV) (w/o vacancy)	Energy/ atom (eV)	Energy (eV) (with vacancy)	$\Delta E_{\mathrm{f},Ni}$ (eV)
$4 \times 4 \times 4$	-1402.3140	-5.4778	-1395.5598	1.276
$10 \times 10 \times 10$	-21911.1565	-5.4778	-21904.4023	1.276
$15 \times 15 \times 15$	-73950.1547	-5.4778	-73943.4044	1.272
$20 \times 20 \times 20$	-175289.2521	-5.4778	-175282.4940	1.280

energy was 10.2413 eV. A vacancy formation energy of 1.28 eV was predicted from a combination of the binary Ni-Re cluster expansion and EVFE. This is not very different from the $\Delta E_{\mathrm{f},Ni}$ value of 1.44 eV (see Table 4.3). These numbers have been tabulated for 4 different simulation cell sizes (see Table 6.1). Also $\Delta E_{\mathrm{m},i}$ value for Ni was 1.08 eV from Equation (5.3) on KRAs, same as the results from the first principles calculations.

Given that all these numbers were fairly accurate, we calculated D_{v} in pure Ni by running kMC simulations for a total of 10^9 (1 billion) vacancy jumps. To obtain better statistics, the kMC trajectory should be divided over a number of segments and D_{v} calculated from the time-weighted average of the diffusion coefficients calculated from the various segments. In order to optimise the kMC segment length, we calculated the D_{v} in pure Ni by considering segment lengths of 10, 100, 1000 ..., 10^8 and 10^9 jumps . This corresponds to a total number of 10^8, 10^7, 10^6,..., 10 and 1 segments respectively. The results are presented in Table 6.2 for the temperature range (1173 K - 1573 K). Also presented in the table are the results for D_{v} in pure Ni from analytical formulations using $\Delta E_{\mathrm{m},Ni}$ of 1.08 eV. We observe that the results from using a segment length of 10000 jumps matched best with the results of the analytical formulations. Hence, we used a segment length of 10000 in all the following calculations. It was concluded that the kMC code works correctly as it was successful in replicating a vacancy correlation factor ≈ 1 in the case of pure Ni. It means the vacancy did indeed undergo a 'random walk' in our kMC simulation.

The self diffusion coefficient in Ni was also calculated and this has been plotted in

Figure 6.1 as a function of temperature. The results completely overlap with the previous results in this work from analytical formulations as well as the kMC code for dilute alloys. Also, a correlation factor of 0.781 was reproduced in pure Ni reaffirming the validity of the code. Similarly, the solute diffusion coefficient of Re in Ni was also calculated for the dilute case using a single Re atom in a $15 \times 15 \times 15$ supercell or an equivalent Re concentration of 0.0074 at.%. This has been shown as open circles in Figure 6.1. The results match very well with the results from analytical formulations as well as the kMC code for dilute alloys.

Table 6.2: The calculated D_v in pure Ni for various kMC segment lengths (total number of jumps is 1 billion in each case) compared to the D_v calculated from analytical formulation with $\Delta E_{m,i}$ of 1.08 eV (see Equation (2.6))

Temperature (K)			1173	1273	1373	1473	1573
		Analytical formulation	7.288E-12	1.687E-11	3.456E-11	6.423E-11	1.103E-10
D_v (m²/s)	kMC segment length	10	8.097E-12 ± 6.781E-17	1.875E-11 ± 1.527E-15	3.840E-11 ± 6.619E-16	7.136E-11 ± 2.237E-15	1.226E-10 ± 1.957E-15
		100	7.361E-12 ± 4.801E-16	1.705E-11 ± 7.934E-15	3.491E-11 ± 1.021E-14	6.485E-11 ± 4.397E-14	1.114E-10 ± 3.573E-14
		1000	7.298E-12 ± 1.925E-15	1.689E-11 ± 1.734E-14	3.461E-11 ± 2.035E-14	6.423E-11 ± 1.069E-13	1.103E-10 ± 2.839E-13
		10000	7.295E-12 ± 7.317E-15	1.690E-11 ± 5.663E-14	3.457E-11 ± 3.314E-14	6.428E-11 ± 8.393E-14	1.103E-10 ± 2.733E-14
		100000	7.233E-12 ± 3.076E-14	1.692E-11 ± 1.636E-13	3.466E-11 ± 6.367E-13	6.413E-11 ± 1.556E-13	1.114E-10 ± 1.232E-12
		1000000	7.395E-12 ± 1.457E-13	1.717E-11 ± 6.389E-13	3.543E-11 ± 9.790E-13	6.580E-11 ± 3.224E-12	1.115E-10 ± 2.847E-12
		10000000	7.645E-12 ± 1.531E-13	1.735E-11 ± 4.009E-13	3.549E-11 ± 2.151E-12	6.459E-11 ± 3.081E-12	1.130E-10 ± 5.014E-12
		100000000	1.040E-11 ± 1.401E-12	2.281E-11 ± 3.741E-12	2.338E-11 ± 6.459E-12	5.393E-11 ± 6.090E-12	1.344E-10 ± 1.667E-11
		1000000000	1.219E-11 ± 2.907E-12	2.184E-11 ± 1.277E-11	6.332E-12 ± 7.885E-12	7.792E-11 ± 1.416E-11	1.519E-10 ± 1.813E-11
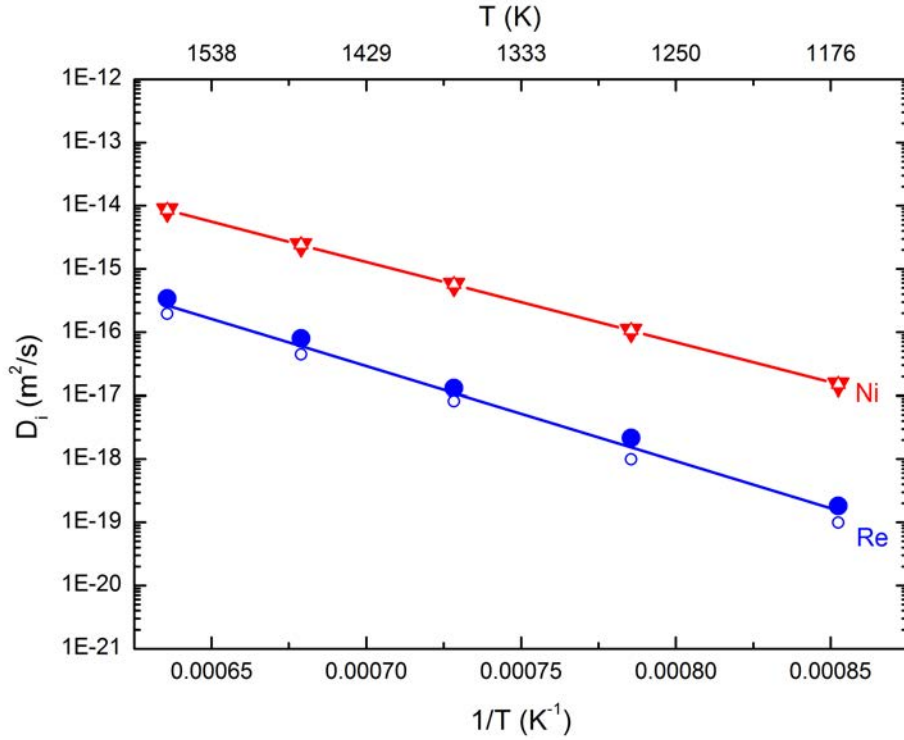
Figure 6.1: The self-diffusion coefficient in Ni and Re diffusion coefficient in Ni as a function of temperature. The open symbols represent the results from the kMC simulations using our code for non-dilute alloys, the filled symbols represent the results from the kMC simulations using the code provided by Dr. Sergej Schuwalow for dilute alloys and the lines represent the results calculated from Lidiard's model

6.3   Results in non-dilute Ni-Re alloys

It must be pointed out that the kMC simulations performed in pure Ni only took a few minutes to complete 1 billion vacancy jumps. This was because the energy of the simulation cell and the $\Delta E_{\mathrm{m},Ni}$ both remain fixed. However in the case of non-dilute alloys of Ni-Re, the energy and the $\Delta E_{\mathrm{m},i}$ have to be calculated at each step.

kMC simulations were run for the non-dilute Ni-Re alloys for 15 million vacancy jumps. These simulations running on single processors took 36 hours on an average to complete. The compositions probed were 1 at.%, 2 at.%, 3 at.%, 4 at.%, 5 at.%, 6.25 at. %, 7.5 at.%, 8.75 at. % and 10 at.% Re in binary alloys with Ni. This was because the concentration

113

of Re in the γ phase even in the third generation of most Ni-based superalloys does not exceed 10 at.% [115]. Multiple trials were run for each of these compositions for better statistics. The segment length chosen was 10000 vacancy jumps as deduced from the results on pure Ni.

6.3.1   Monte Carlo simulations

In order to arrive at the thermodynamically most stable configurations for the non-dilute Ni-Re systems, Monte Carlo simulations using the Metropolis algorithm [68] were run. An initial random configuration was chosen for the system and its energy calculated. At each step of the Monte Carlo simulation, an atom was swapped with another dissimilar atom in the system chosen at random and the energy of the system was recalculated. If the swap led to a decrease in the energy of the system, the new configuration was accepted. If the swap led to an increase in the energy of the system, a random number R, where $0<R<1$ was generated and the new configuration was accepted if

$$R < \exp\left(-\frac{\Delta U}{k_{\mathrm{B}}T}\right) \tag{6.5}$$

where ΔU is the difference in energy of the system due to the swap, k_{B} is the Boltzmann constant and T is the absolute temperature of the system. If this was not the case, the old configuration was kept. In one Monte Carlo cycle, the simulation run through each atom in the system, and several such cycles were run until the energy of the system converged.

Figure 6.2 shows the results obtained for a Ni alloy containing 5 at.% Re at 1373 K. Figure 6.2a shows the initial random distribution of Re atoms in the $15 \times 15 \times 15$ *fcc* supercell of Ni, while Figure 6.2b represents the configuration after 100 Monte Carlo cycles showing that almost all of the Re atoms have clustered together. The cluster of Re atoms appears as fragments, but they can be visualized together as a single cluster considering images of the supercell across periodic boundaries. The results from Figure 6.3 show that the energy of the system has converged in less than 100 Monte Carlo cycles. Similar

results were obtained for Monte Carlo simulations performed at different temperatures as well as for different compositions. In all the cases, the Re atoms clustered together at the end of the Monte Carlo simulations, suggesting that Re would completely phase separate in an alloy with Ni.

The magnitudes of the ECIs obtained in the present work did in fact indicate the formation of Re clusters, and it was also seen that the binding energies increased from Re pairs to triplets to quadruplets. From the available Ni-Re phase diagrams [25], clustering can be expected at lower temperatures as the solubility of Re in Ni significantly falls down, however at higher temperatures Re is expected to be present in the solution with Ni. Results from previous Monte Carlo works [32] have however indicated the presence of short range ordering at lower temperatures, but the ordering again vanishes at higher temperatures. Results from 3D atom probe analysis [26, 27] have also shown that Re atoms are randomly distributed in Ni and neither clustering or ordering is present at high temperatures. Similarly, results from EXAFS experiments [28] show that Re is coordinated by 12 Ni atoms. All this is in contrast to the findings of the present work where Re is not randomly distributed in Ni even at high temperatures. The cluster expansion in the present work found $D1_a$-Ni$_4$Re to be the most stable phase amongst the configurations considered in the first principles dataset. However, unlike the results of Maisel et al [32], the Monte Carlo simulations failed to predict the formation of this phase. This brings out the limitations of the calculated ECIs in the present work. However, it must be noted that the first principles dataset used in the work of Maisel et al [32] was larger than used in the present work. Also, they performed high-throughput calculations on supercells of up to 20 atoms to fit their ECIs. In comparison, supercells of only up to 10 atoms were used in the present work due to the limitations of the available computational resources.

However, while Re clustering was observed in the case of MC simulations, this is highly unlikely to occur over the course of a typical kMC simulation of 15 million jumps as used in the present work and it is expected that the Re distribution would not change

(a) Random distribution of Re atoms at the beginning of the Monte Carlo simulation
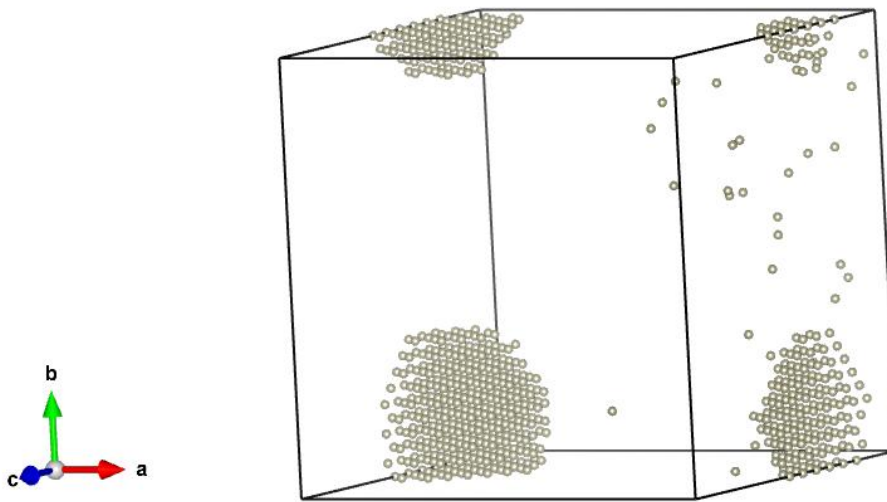
(b) Clustered Re atoms at the end of the Monte Carlo simulation

Figure 6.2: Changes in the configuration of Re atoms for a binary Ni alloy containing 5 at.% Re during the course of the Monte Carlo simulation at 1373 K. The size of the *fcc* simulation cell is $15 \times 15 \times 15$ and the Ni atoms have been deleted for clarity. a, b and c represent the three orthogonal directions.
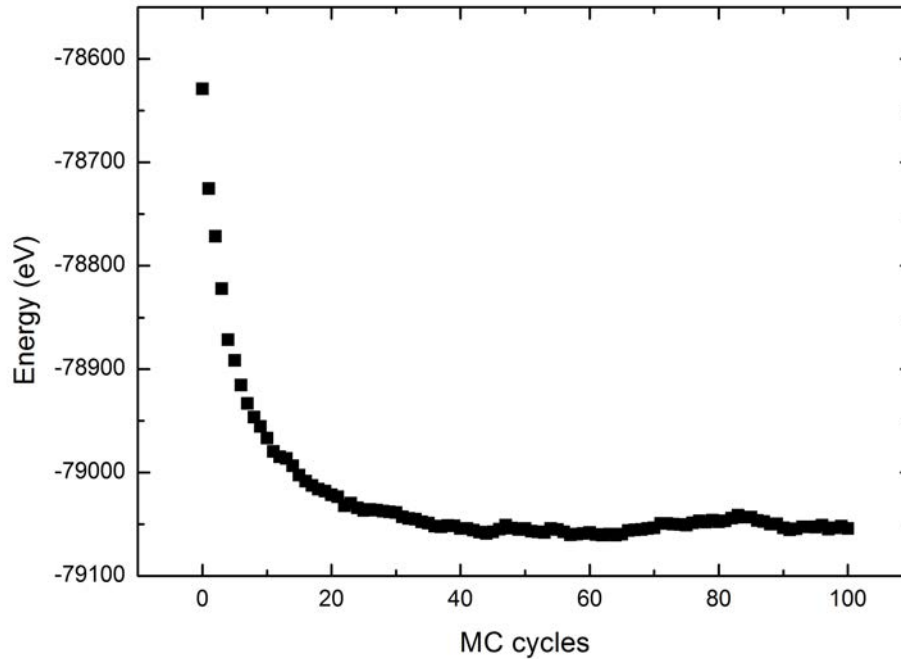
Figure 6.3: Energy of a simulation cell of 5 at.% Re at 1373 K during the course of a Monte Carlo simulation

significantly from an initial random distribution. Figure 6.4 shows the variation in the supercell energy for a sample configuration with 5 at.% Re at 1373 K for the duration of a typical kMC simulation. The change in the energy is negligible when compared to the Monte Carlo simulation suggesting that the system does not evolve sufficiently enough and that Re is expected to be randomly distributed in Ni during the kMC simulations. Thus, the calculated diffusion coefficients would infact be representative of that in a random solution. It must also be pointed out, however that if the kMC simulations were run for a much longer duration, Re atoms would cluster just as the results obtained in MC simulations.

6.3.2 Vacancy diffusion coefficients

The results on the calculated vacancy diffusion coefficients in the non-dilute regime of Ni-Re have been presented in this section. Figure 6.5 shows the running average of D_v

117
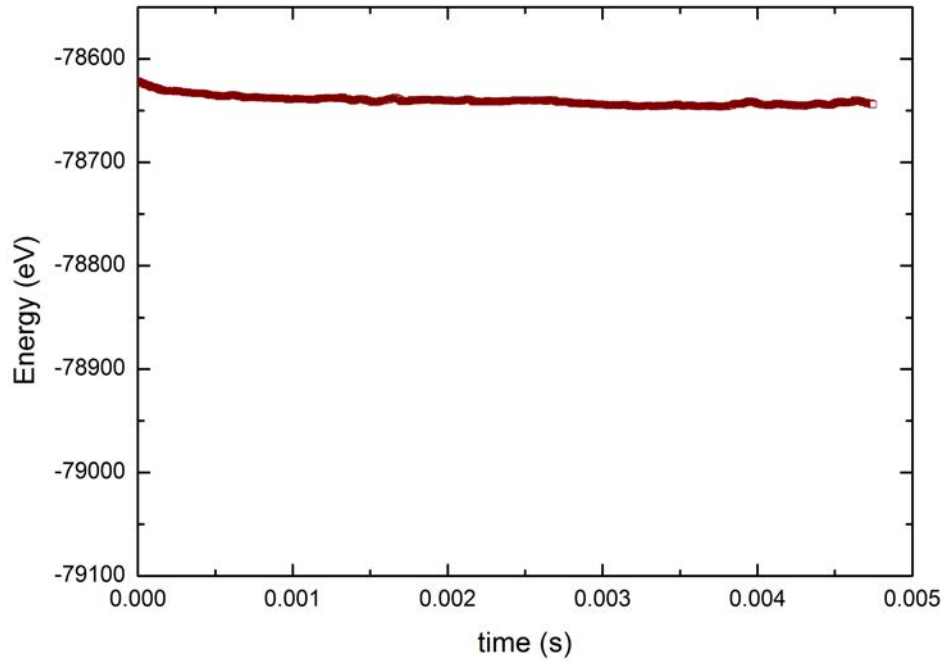
Figure 6.4: Energy of a simulation cell of 5 at.% Re at 1373 K as a function of kMC simulation time (the energy scale has been kept the same as in Figure 6.3 for comparison)

for an alloy with 5 at.% Re at 1373 K over the course of a typical kMC simulation of 15 million vacancy jumps. The D_v value has converged confirming that the duration of the kMC simulations performed in the present work was sufficient.

Figure 6.6 shows the calculated vacancy diffusion coefficients in the non-dilute regime at 1373 K. Several kMC simulations were run for each composition and the mean D_v was calculated. The variation in the results was small, as can be seen from the error bars in Figure 6.6, where the error bars represent the standard deviation from the mean D_v. A linear trend was observed for the entire composition range. This is surprising as it suggests that interactions between Re atoms have no additional effects on vacancy diffusivity. An addition of 10 at.% Re is expected to reduce the D_v in Ni by 36 %.
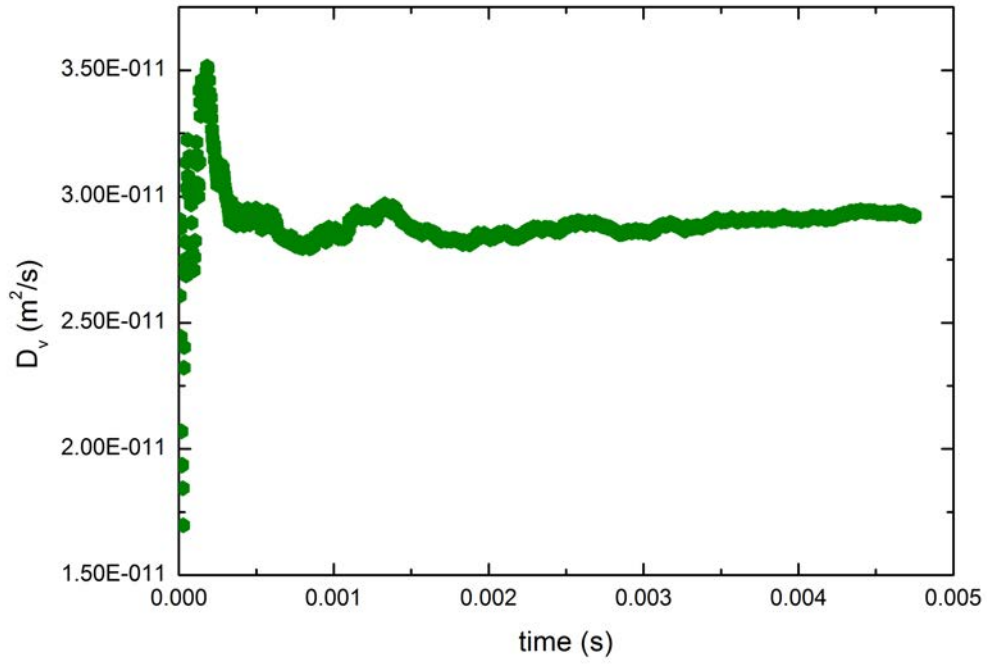
Figure 6.5: The running average of the vacancy diffusion coefficient for an alloy with 5 at.% Re at 1373 K as a function of simulation time
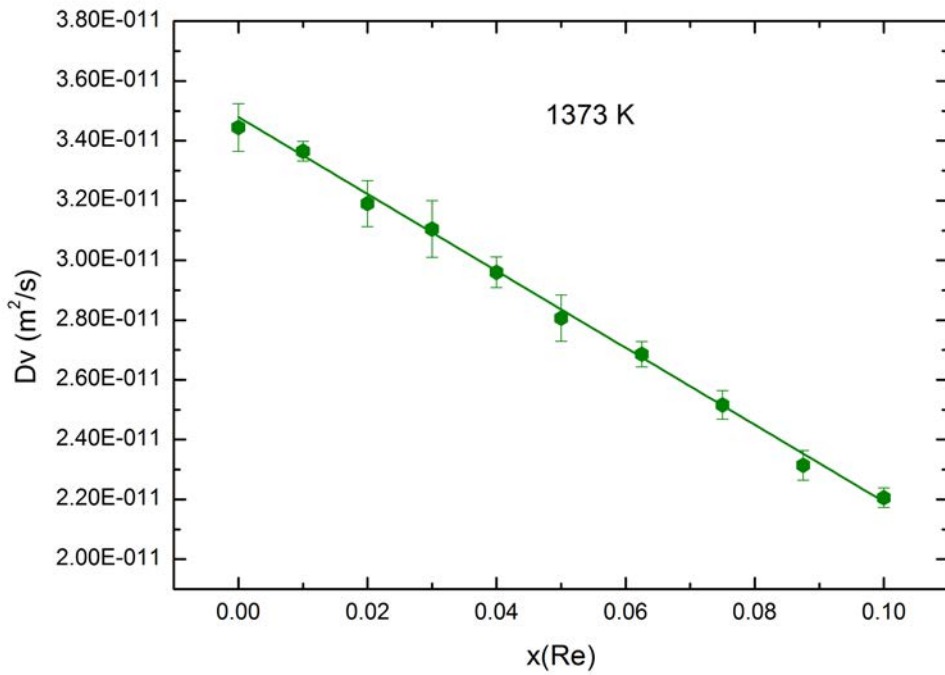
Figure 6.6: Calculated D_v in the non-dilute regime in Ni-Re at 1373 K

119
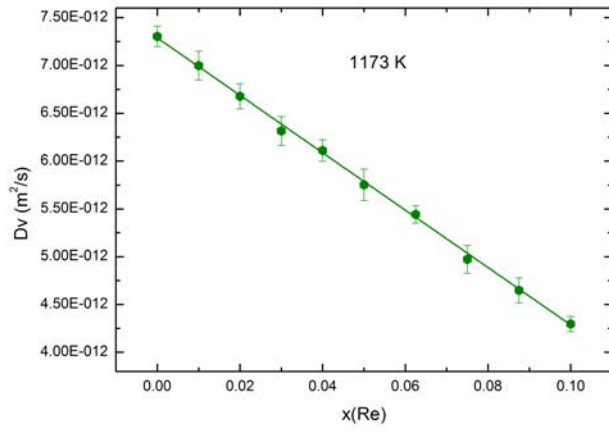
(a) 1173 K
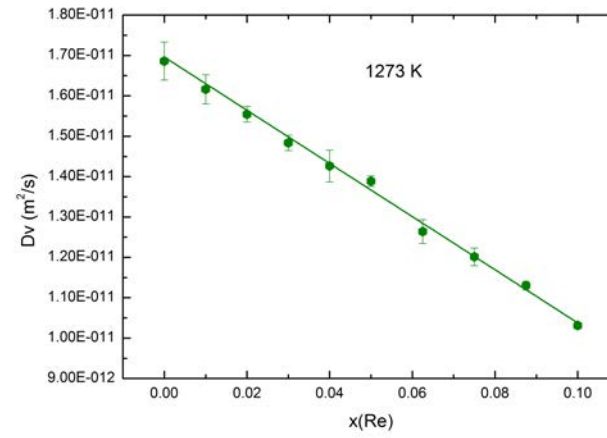
(b) 1273 K
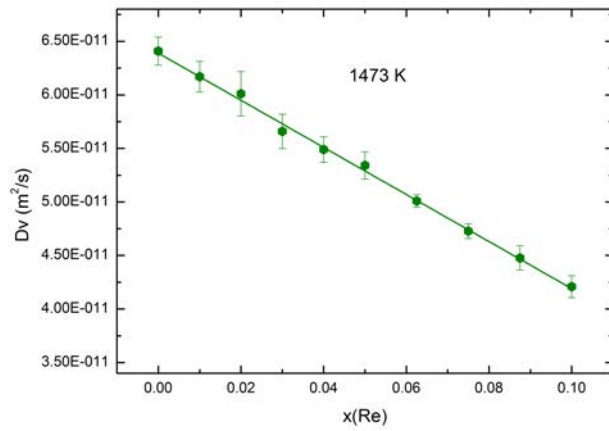
(c) 1473 K
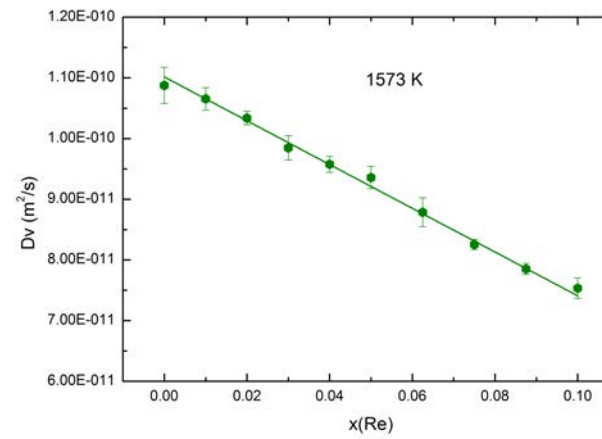
(d) 1573 K

Figure 6.7: Calculated D_{v} in the non-dilute regime in Ni-Re at different temperatures

Table 6.3: The vacancy diffusion coefficient in pure Ni and the calculated slope for D_v as a function of temperature

Temperature (K)	D_v^Ni (m^2/s)	m
1173	7.3E-12	-4.14
1273	1.7E-11	-3.84
1373	3.4E-11	-3.60
1473	6.4E-11	-3.47
1573	1.1E-10	-3.14

The same trend was observed at other temperatures (see Figure 6.7) albeit the reduction in D_v becomes smaller with increasing temperature. From the obtained results, D_v can be described using the following equation:

$$D_\text{v} = D_\text{v}^\text{Ni}(1 + mx_\text{Re}) \qquad (6.6)$$

where D_v is the vacancy diffusion coefficient as a function of Re composition x_Re, D_v^Ni is the vacancy diffusion coefficient in pure Ni and m is the calculated slope. The values for D_v^Ni and m have been tabulated in Table 6.3 for various temperatures.

## 6.3.3   Ni and Re diffusion coefficients

The tracer diffusion coefficients of Ni and Re were also calculated in the non-dilute regime, besides the vacancy diffusion coefficients. The results at 1373 K have been shown in Figure 6.8 and Figure 6.9 for Ni and Re respectively. The error bars representing the standard deviation of D_Ni for the various trials were negligible, while the error bars for D_Re were comparatively larger. This was expected as the number of Ni atoms present in the simulation cells were much larger as compared to the number of Re atoms, and hence better statistical averages were obtained for the case of D_Ni. A deviation from linearity was seen in both D_Ni as well as D_Re as a function of Re composition, however the effect was more pronounced for D_Re. While the D_Ni values decreased with Re concentration monotonically, the D_Re values stayed almost constant up to about 3 - 4 at.% before decreasing in magnitude. This means that up to this concentration, the Re diffusion is
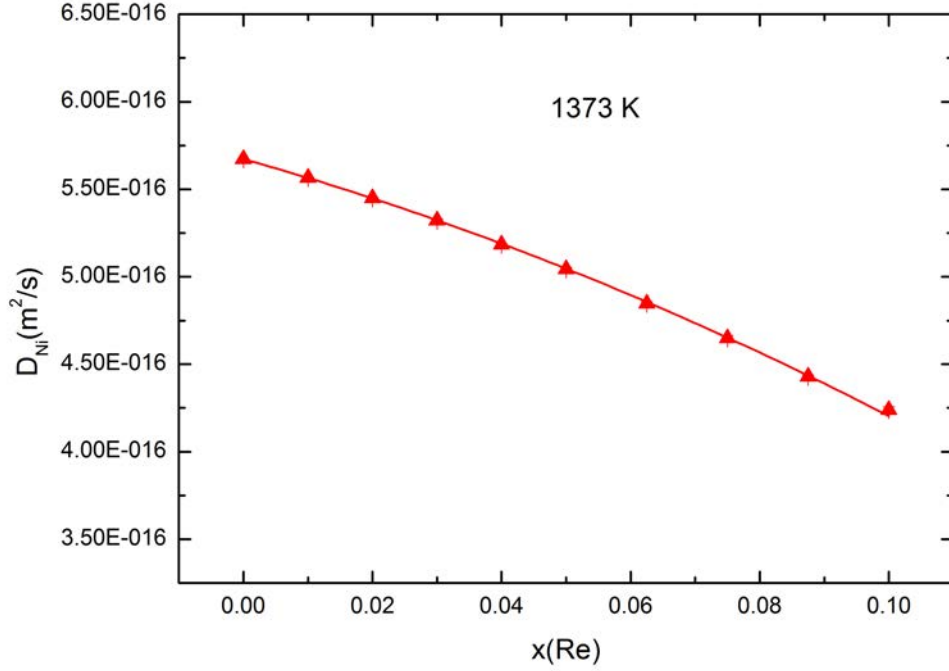
Figure 6.8: Calculated D_{Ni} in the non-dilute regime in Ni-Re at 1373 K

not affected by the presence of other Re atoms and that the Re-Re interactions become sizeable only beyond this concentration.

Empirically, the effect of solute concentration on the self-diffusion coefficient of the solvent and the solute diffusion coefficient in the non-dilute alloys have been described using formulations similar to Equations (6.7) and (6.8) respectively [51, 77]. For the case of D_{Ni}, we have

$$D_{\text{Ni}} = D_{\text{Ni}}^{\text{self}}(1 + b_1 x_{Re} + b_2 x_{Re}^2 + \dots) \tag{6.7}$$

where D_{Ni} is the Ni diffusion coefficient as a function of Re composition x_{Re}, while $D_{\text{Ni}}^{\text{self}}$ is the self-diffusion coefficient of Ni, and b_1, b_2, ... are solvent enhancement factors. It has been argued that b_1 represents the effect of isolated solute atoms on $D_{\text{Ni}}^{\text{self}}$, while b_2 represents the effect of paired solute atoms on $D_{\text{Ni}}^{\text{self}}$ and so on [77]. The term b_1 can be described using analytical formulations [51], however no formulation is available for b_2 and
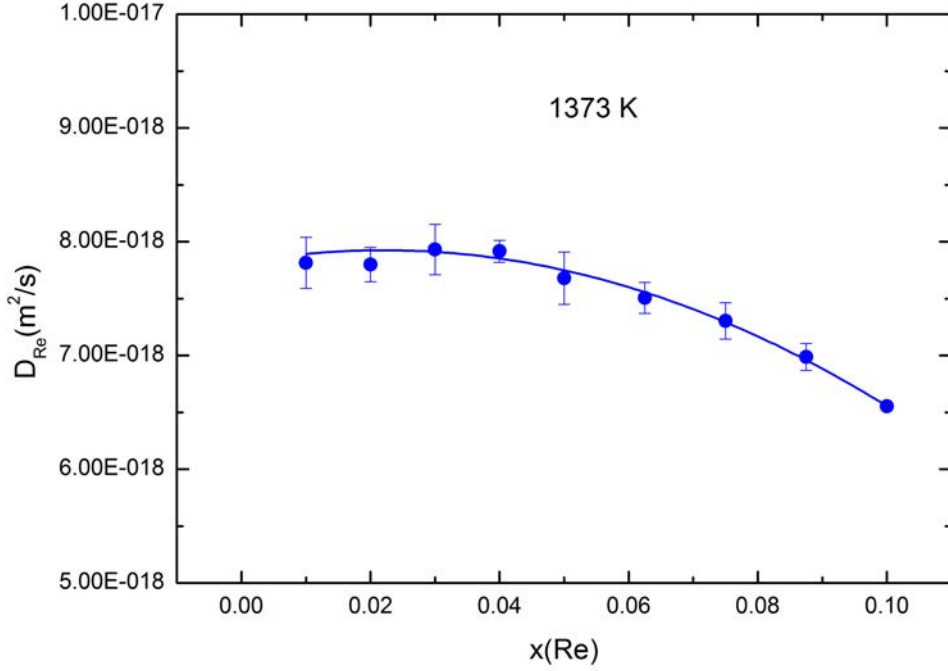
Figure 6.9: Calculated D_{Re} in the non-dilute regime in Ni-Re at 1373 K

higher order terms. Given a deviation from linearity was clearly observed, we have done a parabolic fit of the D_{Ni} data and considered two terms in the Equation (6.7). These fitting parameters have been tabulated in Table 6.4.

Similarly for the case of D_{Re}, we have

$$D_{\text{Re}} = D_{\text{Re}}^{\text{dilute}}(1 + B_1 x_{\text{Re}} + B_2 x_{\text{Re}}^2 + \dots) \tag{6.8}$$

where D_{Re} is the Re diffusion coefficient as a function of Re composition x_{Re}, while

Table 6.4: The self-diffusion coefficient in pure Ni and the calculated solvent enhancement factors for D_{Ni} as a function of temperature

Temperature (K)	$D_{\text{Ni}}^{\text{self}}$ m^2/s	b_1	b_2
1173	1.50E-17	-2.22	-9.81
1273	1.06E-16	-2.02	-8.06
1373	5.67E-16	-1.82	-7.67
1473	2.41E-15	-1.68	-6.34
1573	8.51E-15	-1.53	-6.38

Table 6.5: The Re diffusion coefficient in the dilute case and the calculated solute enhancement factors for D_{Re} as a function of temperature

Temperature (K)	$D_{\mathrm{Re}}^{\mathrm{dilute}}$ m^2/s	B_1	B_2
1173	1.03E-19	0.44	-20.87
1273	1.07E-18	0.73	-23.99
1373	7.82E-18	1.28	-28.95
1473	4.29E-17	1.39	-27.92
1573	1.95E-16	1.40	-27.23

$D_{\mathrm{Re}}^{\mathrm{dilute}}$ represents the Re diffusion coefficient in Ni for the dilute case, and B_1, B_2, ... are solute enhancement factors. The D_{Re} data was also fit to a parabola and these values have been tabulated in Table 6.5. The values for D_{Re} at the Re concentration of 1 at.% were taken as $D_{\mathrm{Re}}^{\mathrm{dilute}}$ in the present case.

The calculated D_{Ni} and D_{Re} values from the kMC simulations at other temperatures have also been shown in Figure 6.10 and Figure 6.11 respectively.
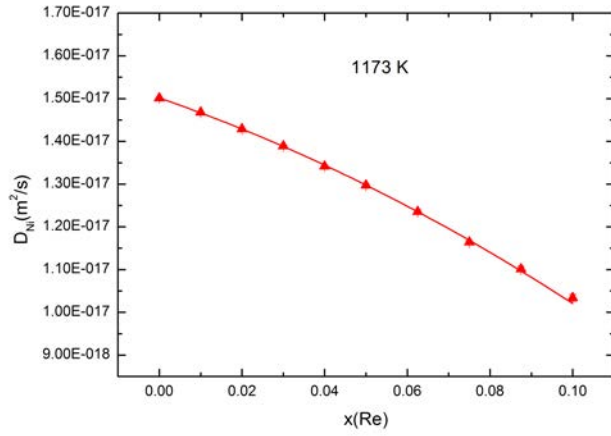
(a) 1173 K
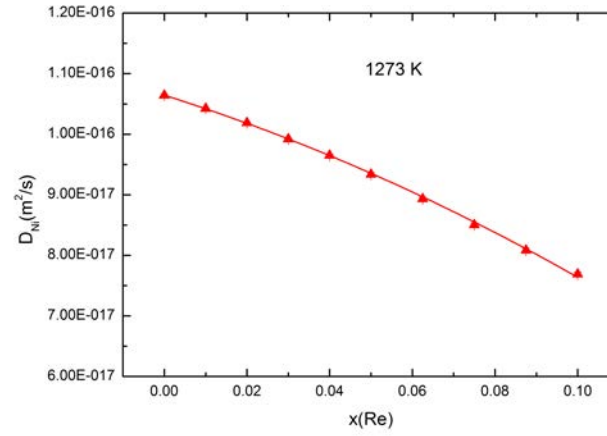
(b) 1273 K
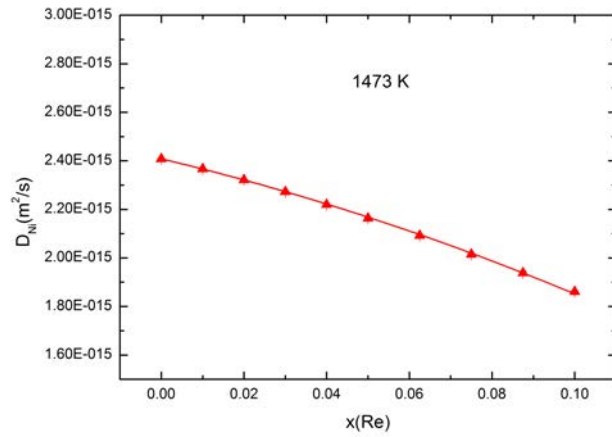
(c) 1473 K
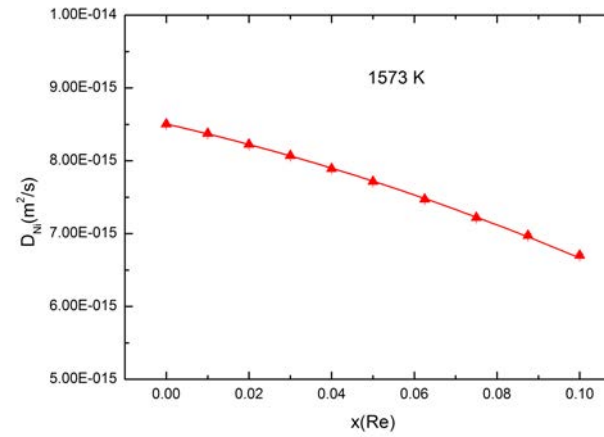
(d) 1573 K

Figure 6.10: Calculated D_{Ni} in the non-dilute regime in Ni-Re at different temperatures
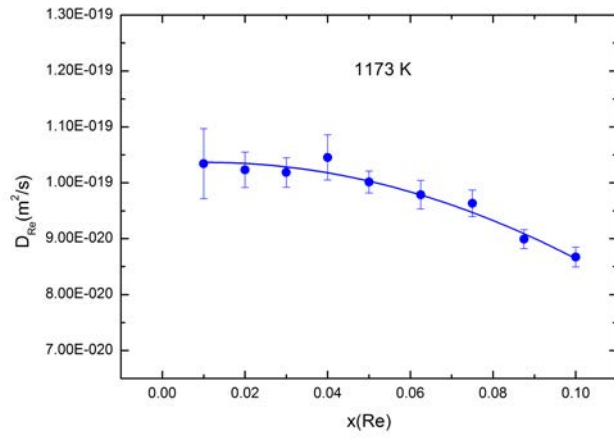
(a) 1173 K
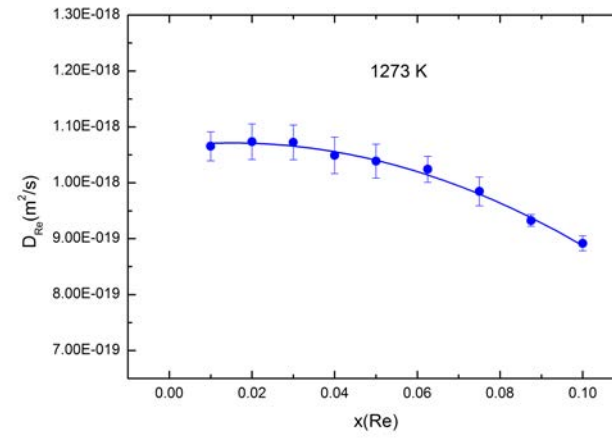
(b) 1273 K
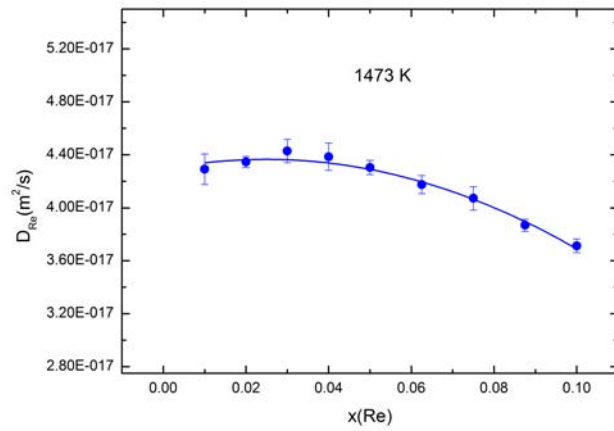
(c) 1473 K
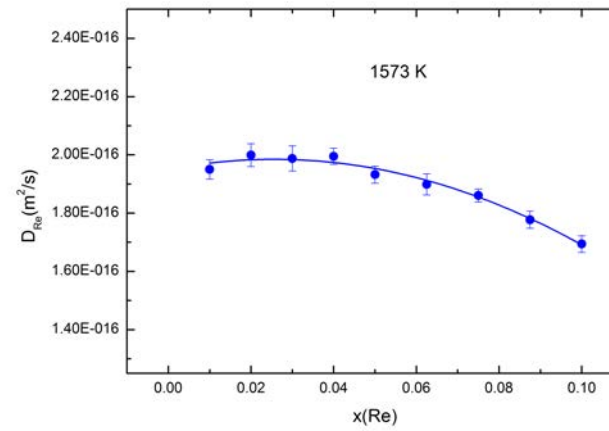
(d) 1573 K

Figure 6.11: Calculated D_{Re} in the non-dilute regime in Ni-Re at different temperatures

6.3.4 Correlation factors

The correlation factors were also calculated from the kMC simulations for the vacancy, the Ni as well as the Re atoms. In the case where an atom or a vacancy does not perform a true random jump, its jump is said to be correlated and its mean square displacement is given as,

$$< |R|^2 >= fn\lambda^2 \tag{6.9}$$

Here, λ is the jump distance, given as $a/\sqrt{2}$, where a is the Ni lattice parameter and n is the number of jumps. Rearranging the Equation (6.9) gives f as,

$$f = \frac{2}{n}\frac{< |R|^2 >}{a^2} \tag{6.10}$$

The kMC simulation was divided over a number of segments and the calculated f values were averaged over these segments. Calculated f_v, f_{Ni} and f_{Re} values for various Ni-Re compositions at 1373 K have been plotted in Figure 6.12. The trend in f_v looks similar to that of D_v at 1373 K (see Figure 6.6). This is expected as D_v is directly proportional to f_v (see Equation (2.18)). f_v is close to unity for pure Ni, and the value gradually drops with increasing Re concentration. However, the decrease in f_v is more pronounced than that predicted by the Manning's model (see Figure 4.7) which predicted a negligible effect of Re concentration on f_v. An addition of 10 at.% Re brings down the f_v to approximately 0.75, implying moderate correlation effects.

An f_{Ni} value of 0.78 was calculated for pure Ni, which matches the value in the literature accurately [58]. The f_{Ni} value decreased linearly with the Re concentration to about 0.62 for 10 at.% Re. This is expected as a reverse jump after a Ni-□ exchange becomes more likely if the Ni atom is surrounded by more Re atoms, given the low value for the Re-□ exchange frequency. As a result, the efficiency of the Ni diffusion is reduced.

In the case of Re, the f_{Re} values could not be calculated up to 5 at.% Re. This is because given the low frequency for a Re-□ exchange, if the Re atoms do not perform a

single jump in an entire kMC segment, the f_{Re} value for that segment becomes undefined, thus giving an error in the overall f_{Re} value. This becomes less likely with increasing Re concentration, as is seen to be the case beyond 5 at.% Re. This is in contrast to the calculation of D_{Re}, where the mean of the squared displacement is taken over all the Re atoms in the system, thus giving a well-defined value even for the case of dilute alloys.

The calculated f_{Re} value was 0.995 for 6.25 at.% Re and dropped only to 0.991 for 10 at.% Re. Thus, effectively the Re diffusive jumps were uncorrelated throughout the investigated composition range, which matches the results from the Lidiard's model (see Figure 4.4).
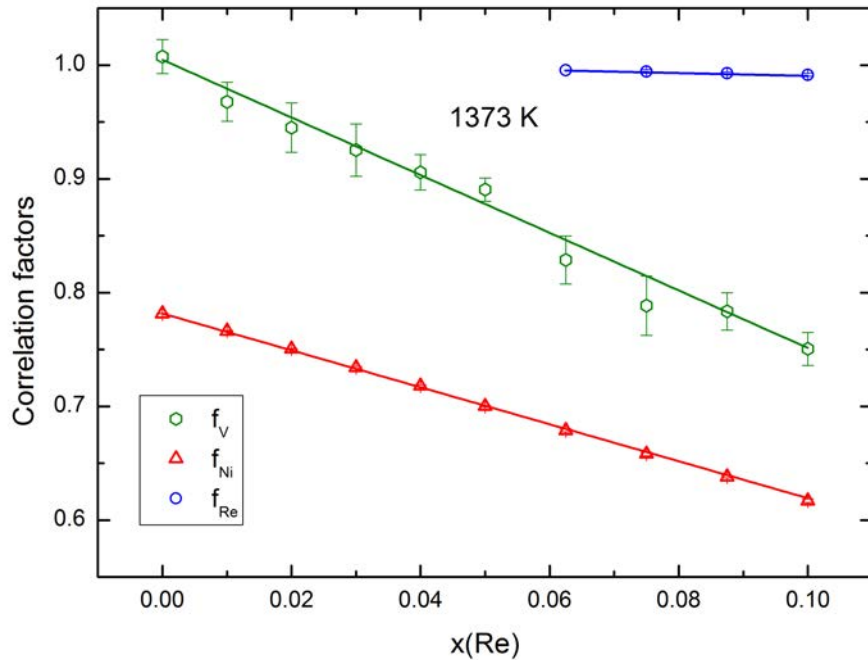
Figure 6.12: Calculated correlation factors in the non-dilute regime in Ni-Re at 1373 K

6.3.5 Variation of D_0 and Q as a function of composition

For pure Ni, the D_0 and Q values can be described using analytical formulations. However, for alloys of Re in Ni, it is difficult to predict these values from analytical formulations, given their complex dependence on temperature. These values were extracted from the

intercepts and the slopes respectively of the $\ln D$ versus $1/T$ curves for the different compositions and have been plotted in Figure 6.13 and 6.14 as a function of composition.

In pure Ni, the calculated D_0^{v} value was 3.03×10^{-7} m^2/s and Q_{v} value was 1.075 eV, compared to the expected D_0^{v} value of 2.81×10^{-7} m^2/s ($a^2 \times \nu_{Ni}^*$) and Q_{v} value of 1.08 eV. D_0^{Ni} and Q_{Ni} values were 10.1×10^{-7} m^2/s and 2.52 eV respectively and matched the expected values from analytical formulations exactly (see Table 4.3). A D_0^{Re} value of 7.7×10^{-7} m^2/s and Q_{Re} value of 2.99 eV was calculated for 1 at.% Re in Ni and these values also matched the expected values for dilute alloys of Re in Ni(see Table 4.3).

While the D_0^{v} curve showed no trend with increasing Re concentration, the Q_{v} values increased almost linearly with the Re concentration. Re, having a ΔE_m value of 1.51 eV compared to a value of 1.08 eV for pure Ni, is expected to increase the overall Q_{v} value in alloys with Ni. A Q_{v} value of 1.14 eV was calculated for 10 at.% Re clearly demonstrating that the vacancy diffusion becomes slower with increasing amount of Re.

Both the D_0^{Ni} and Q_{Ni} values increased with the Re concentration. While the D_0^{Ni} value at 10 at.% Re was about 1.2 times the value in pure Ni, the Q_{Ni} value increased from 2.52 eV to about 2.57 eV, which is equivalent to a decrease in the diffusivity by a factor of approximately 0.65 at a temperature of 1373 K.

However, no trend was observed for the case of D_0^{Re} and Q_{Re}. This can be attributed to the large standard deviations in the calculated D_{Re} data. A smaller value for Re-$\square$ exchange frequency complemented with the smaller number of Re atoms in the simulation cells result in fewer Re jumps over the course of a kMC simulation. This leads to relatively inferior statistics when compared to the case of Ni. It must be noted that D_0 and Q values are highly sensitive to the calculated diffusion coefficients, and hence more precision is required in the diffusion coefficients data when deducing the D_0 and Q values accurately is the main objective. This would require running the kMC simulations for many more times or for longer durations.
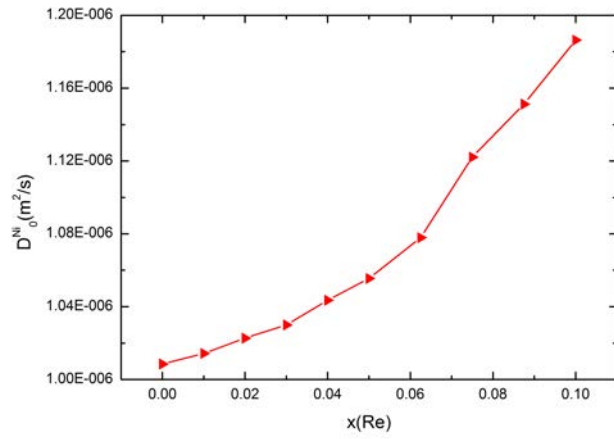
(a) Calculated D_0^{Ni} as a function of Re composition
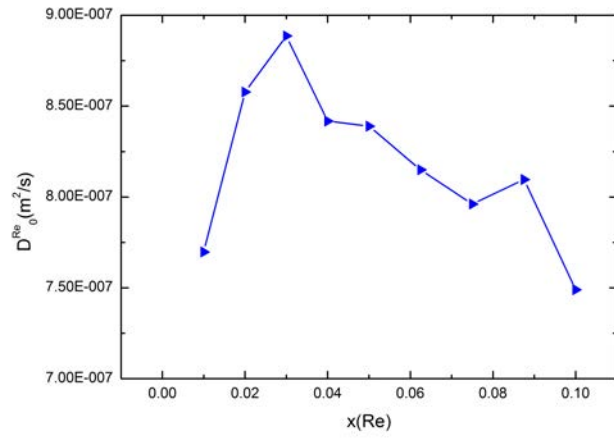
(b) Calculated D_0^{Re} as a function of Re composition
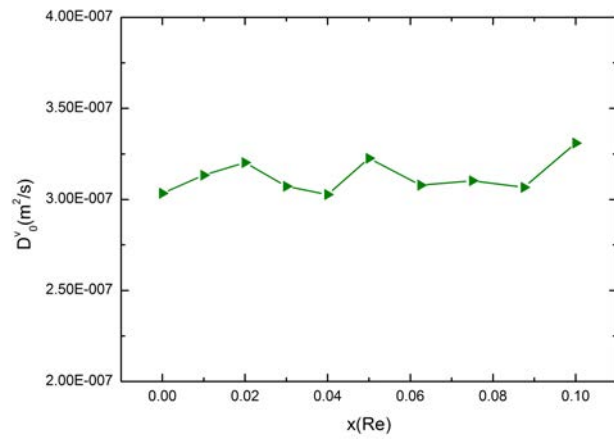
(c) Calculated D_0^{v} as a function of Re composition

Figure 6.13: Calculated diffusion pre-factors as a function of Re composition in Ni
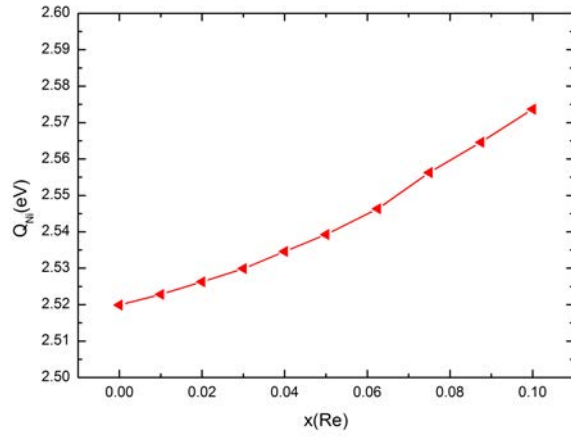
(a) Calculated Q_{Ni} as a function of Re composition
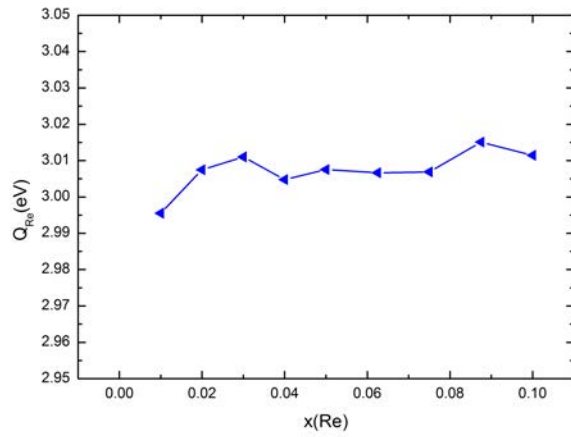
(b) Calculated Q_{Re} as a function of Re composition
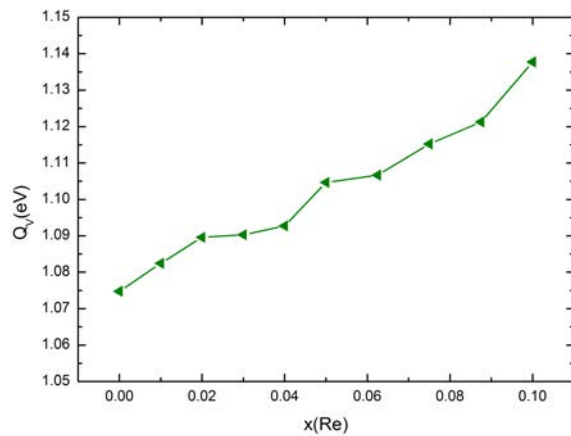
(c) Calculated Q_{v} as a function of Re composition

Figure 6.14: Calculated activation energies as a function of Re composition in Ni
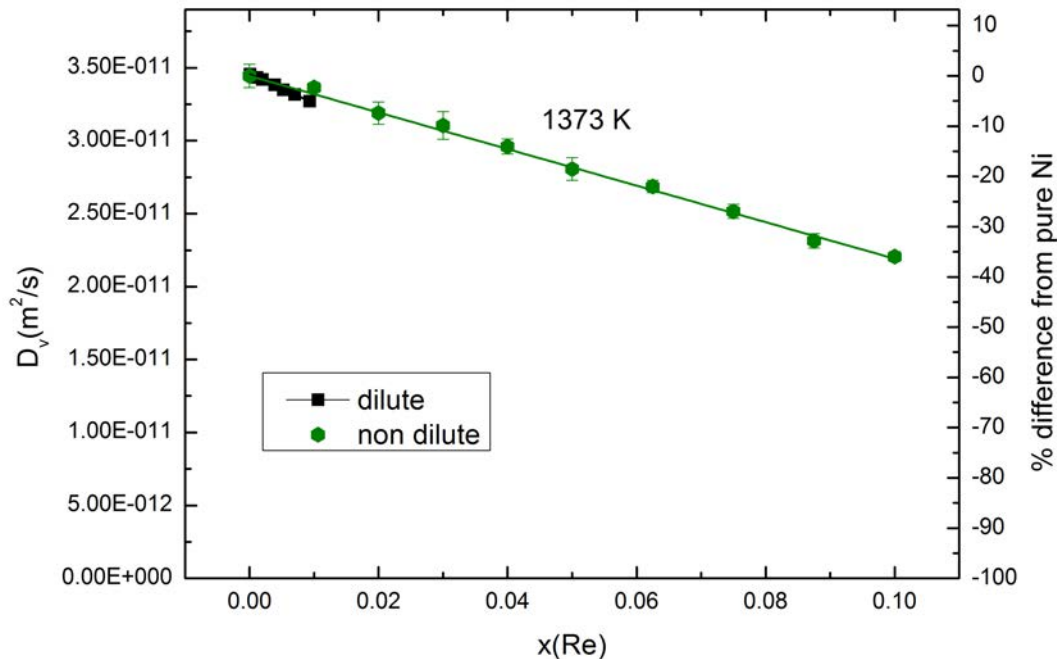
Figure 6.15: Comparison of the calculated D_v in the dilute and the non-dilute regime in Ni-Re at 1373 K

6.3.6 Comparison with the kMC results on dilute alloys

The results from the kMC calculations in the non-dilute regime of Ni-Re have been compared to the results from that in dilute regime at 1373 K(see Figure 6.15). The results match very well and overall the kMC code based on the dilute alloys predicts an effect that is approximately 1.5 times more pronounced than that based on the non-dilute alloys. The consideration of the extended barriers in the kMC code for dilute alloys gives it a more accurate description, however, solute-solute interactions cannot be accounted for therein, and hence, it is only restricted to solute compositions below 1 at.%. The non-dilute code relies on a number of fitting parameters to account for the solute-solute interactions, and hence the predictions depend on the accuracy of these fitting parameters, particularly the KRAs. Better accuracy can be achieved in the prediction of the D_v from the non-dilute code by including more KRAs corresponding to newer configurations with more Re atoms.

6.3.7 Discussion

Having calculated the vacancy diffusion coefficients in the dilute as well as non-dilute regime for Ni-Re alloys, its application to a creep model needs to be verified. It must be reiterated that Ni-based superalloys are used in high temperature applications where creep is the main deformation mechanism. One commonly used creep model is shown in Equation (6.11) [51],

$$\dot{\epsilon} = A_2 D_{\text{eff}} \left[\frac{\gamma_{SFE}}{Gb}\right]^n \left[\frac{\sigma}{E}\right]^m \tag{6.11}$$

where A_2, n and m are structure dependent fitting parameters, D_{eff} is the effective diffusion coefficient, γ_{SFE} is the stacking fault energy, σ is the applied stress, b is the Burgers vector, G is the shear modulus and E is the Young's modulus. Other models such as the one used by Zhu et al [38] also include superalloy microstructural factors like γ' size and volume fraction. Most of these factors are composition dependent and also vary with temperature. Thus, in order to study the effect of one of these factors on the creep rate, all the other factors, in principle have to be constant.

In the present work, we were interested in studying the effect of composition on D_{eff}, which determines the rate of mass transport in the alloy. However, there is no unique formulation for calculating D_{eff} [120, 121, 122, 123] and in the present work, we have argued that D_{v} is an equivalent measure of D_{eff}. Indeed, the atomic mass transport is counter-balanced by the diffusion of vacancies and the net flux of vacancies is equal and opposite to the net flux of atoms in the alloy. Vacancies have to diffuse from emitting dislocation cores to absorbing dislocation cores through the γ matrix for climb to continue at the γ/γ' interface during creep.

For the case of pure Ni, D_{eff} would be the same as D_{Ni}. Comparing Equations (2.6) and (2.18) in pure Ni, we have,

$$D_{\text{v}} = \frac{D_{\text{Ni}}}{x_{\text{v},Ni}} \frac{f_{\text{v}}}{f_{\text{Ni}}} \tag{6.12}$$

From Figure 6.12, the ratio of f_v to f_{Ni} is approximately constant at about 1.25 throughout the probed composition range. If the concentration of vacancies, $x_{v,i}$ in the alloy is also assumed to be constant, then extending Equation (6.12) to an alloy of Ni, we have

$$D_v \propto D_{eff} \tag{6.13}$$

It means that the relative effect of the alloy composition on D_v should be the same as D_{eff}. However, it must be kept in mind that since $x_{v,Ni}$ is very small in magnitude ($\approx 10^{-5}$) even at high temperatures, D_{eff} and D_v would differ by orders of magnitude. Indeed, vacancies have to diffuse for much longer distances through the lattice compared to the individual atoms. Nevertheless, having established that the effective diffusion coefficient is proportional to the vacancy diffusion coefficient to a first approximation, we calculated vacancy diffusion coefficients in the present work. Also, in Chapter 1, the role of vacancies in determining the rate of dislocation climb was discussed and the beneficial role of Re additions was attributed to its possible slowing down of the rate of vacancy diffusion, while its effect on other factors was found to be minimal.

Again, it has been found that the creep strain rate $\dot{\epsilon}$ is inversely proportional to the time to rupture t_r of the superalloy component. Thus, we have

$$\dot{\epsilon} \times t_r = B \tag{6.14}$$

where B is a constant. This is called the Monkman-Grant relationship [1]. Comparing Equations (6.11),(6.13) and (6.14), we have

$$D_v \propto \frac{1}{t_r} \tag{6.15}$$

We use this relationship to validate the creep results of Blavette et al [12] conducted on two different Ni-based superalloys, CMSX-2 and PWA 1480 at a temperature of 1123 K and an applied stress of 500 MPa. Re additions were made to these first generation

superalloys at the expense of W partially or completely. The corresponding Re composition in the γ phase, x_{Re} and time to rupture, t_r for these superalloys before and after Re addition have been tabulated in Table 6.6. The superalloy samples were heat treated at the same temperature as the creep tests, and hence the x_{Re} values represent the actual Re composition of the alloy at the creep temperature. Given that all other factors remain unchanged, the increase in creep lives should be attributed to the change in D_v by the Re addition. Table 6.7 shows the D_v values calculated in the binary Ni-Re alloys for pure Ni, 3 at.% Re and 4 at.% Re at 1173 K, which closely resemble the investigated superalloys. The calculated decrease in D_v accounts for about three-fifth of the decrease in t_r^{-1} in both the cases. This largely explains the origin of the Re-effect in these alloys.

Again, from the calculation of D_v using the code for dilute alloys (see Figure 4.11), it was found that W has the same potency as Re as far as reduction in D_v is concerned. Thus, given that Re additions were made to these alloys at the expense of W, one can justify the improvement in creep lives to the fact that Re partitioning to the γ phase is stronger than W. Indeed, while the W concentration in the γ phase of PWA 1480 alloy was 2.15 at.%, on being replaced by Re completely in the PWA 1480+Re alloy, the Re concentration in the γ phase was 3.71 at.%. Thus, the Re-effect should be explained in totality by its slowing down of the vacancy diffusion together with strong partitioning to the γ phase.

It must be pointed out that validation of our results would require agreement with more creep data on superalloys from a number of sources. However, it is important to understand that the number of variables in superalloys metallurgy is very large, and hence availability of creep data where most variables have been kept fixed is difficult. For example, adding or removing one element at the expense of other does change the partitioning of all the elements, the volume fraction of γ' as well as the elastic properties. Furthermore, the phase composition data is not available for the majority of the creep experiments and the authors tend to fit their creep models to the overall composition instead of the γ composition.

Table 6.6: Re composition in γ phase (x_{Re}) and time to rupture (t_{r}) for some superalloys studied by Blavette et al [12] at 1123 K and 500 MPa

Superalloy	x_{Re}	t_{r} (hours)	% decrease in $\left(\dfrac{1}{t_{\mathrm{r}}}\right)$
CMSX-2	0	382	-
CMSX-2 + Re	0.0287	498	23.3
PWA 1480	0	356	-
PWA 1480 + Re	0.0371	497	28.3

Table 6.7: D_{v} corresponding to Re composition in binary Ni-Re alloys at 1173 K calculated in the present work

Alloy	x_{Re}	D_{v} (m^2/s)	% decrease in D_{v}
Pure Ni	0	7.30E-12	-
Ni-3 at.% Re	0.03	6.32E-12	13.5
Pure Ni	0	7.30E-12	-
Ni-4 at.% Re	0.04	6.11E-12	16.3

In this work, we have tried to quantitatively isolate the effect of few solute elements on D_{v} in binary alloys of Ni to gain a better understanding of diffusion and how it is affected by composition. To get a complete picture, the role of other elements commonly added to Ni-based superalloys on the vacancy diffusion should also be investigated. Further, to understand the impact of one solute element on another, it is desirable to investigate ternary systems. This can similarly be achieved using a combination of cluster expansion and kMC simulations, albeit a larger set of ECIs would be required to model the ternary system, which would require a much larger first-principles dataset. Similarly, development of improved KRAs would be required to accurately describe the activation energy barriers. This will be the subject of further work.

CHAPTER 7

CONCLUSIONS AND SCOPE FOR FUTURE WORK

In this thesis, the effect of solute atoms on diffusional processes was investigated using a variety of computational methods. Analytical approximations were used to study the effect of dilute levels of Re, W and Ta on the diffusivities of vacancies in *fcc* Ni. Results from analytical formulations were compared to kinetic Monte Carlo simulations performed based on data obtained from density functional theory. This was done to attempt to explain how composition may affect the climb of dislocations at the γ/γ' interfaces, with ramifications on creep properties.

Results for diffusivity in the dilute regime suggest the relationship between vacancy diffusivity and solute content for all elements considered is linear in nature. It is apparant from the dilute results that there is a discrepancy between the analytical model and the kinetic Monte Carlo simulations. This is due to several simplifying assumptions in the analytical model, while the kinetic Monte Carlo simulations explicitly included the diffusion processes to accurately describe the systems. The magnitude of the effect predicted by the kinetic Monte Carlo simulations is appreciable in size, however, the concentration of solute elements in the γ phase of Ni-based superalloys is such that solute-solute interactions must be considered to account for the non-dilute concentrations in the relevant phase.

To that effect, this work was extended to consider diffusivity in non-dilute systems

using kinetic Monte Carlo simulations. In order to consider the energetics of a complex binary system, the cluster expansion was employed to efficiently calculate the total energy of a configuration of atoms on the *fcc* lattice while the values of migration energy barriers were also cluster expanded considering first neighbours only. Non-dilute results suggest that solute-solute interactions have minimal effects on vacancy diffusivity. It should be pointed out, however that the reliance of these results on accurate effective cluster interactions and cluster expanded migration barriers means that some inaccuracy should be expected.

Such a comprehensive study of the effect of solute content on vacancy diffusivity and solute/solvent diffusivity in the non-dilute regime has not been carried out in superalloys field and helps to clarify how Re may affect the creep properties in these materials. Indeed, several authors have suggested that the renowned Re-effect could be attributed to the fact that Re, the slowest diffusing solute in Ni-based superalloys, slows down diffusional processes required for dislocation climb. This work indicates that, while Re additions slow down vacancy diffusivity in these alloys, its effect is similar to W. Hence, a key aspect of the beneficial impact of Re additions on creep properties is that Re strongly partitions to the γ phase in superalloys where dislocation climb occurs.

The results of this work were used to rationalise the improvements in creep life of Re containing alloys using simple well-recognised models for predicting creep strain rate. These show that the beneficial effects of Re on the creep properties of Ni-based superalloys can be partially accounted for by the effect of Re on diffusional processes. However, it should be pointed out that whenever alloy compositions are modified to investigate the role of solute elements on creep, several variables are modified at once. Indeed, small additions of Re are known to reduce γ' phase fraction, increase lattice misfit, retard rafting and affect dislocation processes in the γ phase. Therefore, careful experimentation to evaluate each of these effects independently would be desirable.

In terms of future work, there are several areas where the present research can be improved upon. Re clustering in Ni should be investigated in more detail to resolve the

discrepancy between different studies. The calculation of non-dilute diffusivities should be extended to treat ternary systems, which would require effective cluster interaction coefficients and kinetically resolved activation barriers fit against a larger dataset. Diffusion calculations, especially in the non-dilute regime must also be performed on other alloying elements commonly added to Ni-based superalloys. This is desirable in order to get a complete picture of the effect of chemistry on creep in superalloys.

LIST OF REFERENCES

[1] R. C. Reed. *The superalloys: fundamentals and applications.* Cambridge University Press, 2006.

[2] A. Mottura and R. C. Reed. What is the role of rhenium in single crystal superalloys? *MATEC Web of Conferences*, 14:01001, 2014.

[3] G. E. Dieter. *Mechanical metallurgy.* McGraw-Hill series in materials science and engineering. McGraw-Hill, 1986.

[4] V. Paidar, D. P. Pope, and V. Vitek. A theory of the anomalous yield behavior in $L1_2$ ordered alloys. *Acta Metallurgica*, 32(3):435–448, 1984.

[5] C. M. F. Rae and R. C. Reed. The precipitation of topologically close-packed phases in rhenium-containing superalloys. *Acta Materialia*, 49(19):4113 – 4125, 2001.

[6] G. A. Whittaker. Precision casting of aero gas turbine components. *Materials Science and Technology*, 2(5):436–441, 1986.

[7] Y. Amouyal, Z. Mao, and D. N. Seidman. Effects of tantalum on the partitioning of tungsten between the γ and γ'-phases in nickel-based superalloys: linking experimental and computational approaches. *Acta Materialia*, 58(18):5898–5911, 2010.

[8] A. F. Giamei. Deformation and fracture of advanced anisotropic superalloys. AFOSR Annual Report FR-11009, 1978.

[9] A. Sato, H. Harada, T. Yokokawa, T. Murakumo, Y. Koizumi, T. Kobayashi, and H. Imai. The effects of ruthenium on the phase stability of fourth generation Ni-base single crystal superalloys. *Scripta Materialia*, 54(9):1679 – 1684, 2006.

[10] N. Matan, D. C. Cox, C. M. F. Rae, and R. C. Reed. On the kinetics of rafting in CMSX-4 superalloy single crystals. *Acta Materialia*, 47(7):2031–2045, 1999.

[11] A. F. Giamei and D. L. Anton. Rhenium additions to a Ni-base superalloy: effects on microstructure. *Metallurgical Transactions A*, 16(11):1997–2005, 1985.

[12] D. Blavette, P. Caron, and T. Khan. An atom probe investigation of the role of rhenium additions in improving creep resistance of Ni-base superalloys. *Scripta Metallurgica*, 20(10):1395 – 1400, 1986.

[13] D. Blavette, P. Caron, and T. Khan. An atom-probe study of some fine-scale microstructural features in Ni-based single crystal superalloys. In S. Reichman, D. N. Duhl, G. Maurer, S. Antolovich, and C. Lund, editors, *Superalloys 1988*, pages 305–314. The Minerals, Metals and Materials Society, Warrendale, PA, USA, 1988.

[14] J. Li, D. Tang, R. Lao, S. Liu, and Z. Wu. Effects of rhenium on creep rupture life of a single crystal superalloy. *Journal of Materials Science and Technology*, 15(1):53–57, 1999.

[15] S. Wöllmer, T. Mack, and U. Glatzel. Influence of tungsten and rhenium concentration on creep properties of a second generation superalloy. *Materials Science and Engineering: A*, 319-321:792–795, 2001.

[16] A. C. Yeh and S. Tin. Effects of Ru and Re additions on the high temperature flow stresses of Ni-base single crystal superalloys. *Scripta Materialia*, 52(6):519–524, 2005.

[17] B. Gan and S. Tin. Assessment of the effectiveness of transition metal solutes in hardening of Ni solid solutions. *Materials Science and Engineering: A*, 527(26):6809–6815, 2010.

[18] J. P. Hirth and J. Lothe. *Theory of dislocations.* Krieger Publishing Company, Malabar, Florida, 1982.

[19] A. Mottura. *Analysis of atomic-scale phenomena and the rhenium-effect in nickel based superalloys.* PhD thesis, Imperial College London, 2009.

[20] S. L. Shang, C. L. Zacherl, H. Z. Fang, Y. Wang, Y. Du, and Z. K. Liu. Effects of alloying element and temperature on the stacking fault energies of dilute Ni-base superalloys. *Journal of Physics: Condensed Matter*, 24(50):505403, 2012.

[21] X. X. Yu and C. Y. Wang. The effect of alloying elements on the dislocation climbing velocity in Ni: a first-principles study. *Acta Materialia*, 57(19):5914–5920, 2009.

[22] F. Pettinari, J. Douin, G. Saada, P. Caron, A. Coujou, and N. Clément. Stacking fault energy in short-range ordered γ-phases of Ni-based superalloys. *Materials Science and Engineering: A*, 325(1-2):511–519, 2002.

[23] F. Diologent and P. Caron. On the creep behavior at 1033K of new generation single-crystal superalloys. *Materials Science and Engineering: A*, 385(1):245–257, 2004.

[24] N. Wanderka and U. Glatzel. Chemical composition measurements of a nickel-base superalloy by atom probe field ion microscopy. *Materials Science and Engineering: A*, 203(1-2):69–74, 1995.

[25] H. Okamoto. Ni-Re (nickel-rhenium). *Journal of Phase Equilibria and Diffusion*, 33(4):346–346, 2012.

[26] A. Mottura, M. K. Miller, and R. C. Reed. Atom probe tomography analysis of possible rhenium clustering in nickel-based superalloys. In R. C. Reed, P. Caron, T. Gabb, E. Huron, and S. Woodard, editors, *Superalloys 2008*, pages 891 – 900. The Minerals, Metals and Materials Society, 2008.

[27] A. Mottura, N. Warnken, M. K. Miller, M. W. Finnis, and R. C. Reed. Atom probe tomography analysis of the distribution of rhenium in nickel alloys. *Acta Materialia*, 58(3):931–942, 2010.

[28] A. Mottura, R. T. Wu, M. W. Finnis, and R. C. Reed. A critique of rhenium clustering in Ni-Re alloys using extended X-ray absorption spectroscopy. *Acta Materialia*, 56(11):2669–2675, 2008.

[29] A. Mottura, M. W. Finnis, and R. C. Reed. On the possibility of rhenium clustering in nickel-based superalloys. *Acta Materialia*, 60(6-7):2866–2872, 2012.

[30] A. Breidi, S. G. Fries, M. Palumbo, and A. V. Ruban. First-principles modeling of energetic and mechanical properties of Ni-Cr, Ni-Re and Cr-Re random alloys. *Computational Materials Science*, 117:45 – 53, 2016.

[31] S. He, P. Peng, O. I. Gorbatov, and A. V. Ruban. Effective interactions and atomic ordering in Ni-rich Ni-Re alloys. *Physical Review B*, 94(2):024111, 2016.

[32] S. B. Maisel, N. Schindzielorz, A. Mottura, R. C. Reed, and S. Müller. Nickel-rhenium compound sheds light on the potency of rhenium as a strengthener in high-temperature nickel alloys. *Physical Review B*, 90(9):094110, 2014.

[33] P. J. Warren, A. Cerezo, and G. D. W. Smith. An atom probe study of the distribution of rhenium in a nickel-based superalloy. *Materials Science and Engineering: A*, 250(1):88–92, 1998.

[34] K. E. Yoon, D. Isheim, R. D. Noebe, and D. N. Seidman. Nanoscale studies of the chemistry of a René N6 superalloy. *Interface Science*, 9(3/4):249–255, 2001.

[35] B. H. Ge, Y. S. Luo, J. R. Li, and J. Zhu. Distribution of rhenium in a single crystal nickel-based superalloy. *Scripta Materialia*, 63(10):969 – 972, 2010.

[36] A. Janotti, M. Krčmar, C. L. Fu, and R. C. Reed. Solute diffusion in metals: larger atoms can move faster. *Physical Review Letters*, 92(8):085901, 2004.

[37] M. S. A. Karunaratne, P. Carter, and R. C. Reed. Interdiffusion in the face-centred cubic phase of the Ni-Re, Ni-Ta and Ni-W systems between 900 and 1300 °C. *Materials Science and Engineering: A*, 281(1-2):229–233, 2000.

[38] Z. Zhu, H. Basoalto, N. Warnken, and R. C. Reed. A model for the creep deformation behaviour of nickel-based single crystal superalloys. *Acta Materialia*, 60(12):4888–4900, 2012.

[39] J. Danas and V. S. Deshpande. Plane-strain discrete dislocation plasticity with climb-assisted glide motion of dislocations. *Modelling and Simulations in Materials Science and Engineering*, 21(4):045008, 2013.

[40] D. Morderhai, E. Clouet, M. Fivel, and M. Verdier. Introducing dislocaiton climb by bulk diffusion in discrete dislocation dynamics. *Philosophical Magazine*, 88(6):899–925, 2008.

[41] S. M. Hafez Haghighat, G. Eggeler, and D. Raabe. Effects of climb on dislocation mechanisms and creep rates in γ'-strengthened Ni base superalloys single crystals: a discreet dislocation dynamics study. *Acta Materialia*, 61:3709–3723, 2013.

[42] B. F. Dyson. Microstructure based creep constitutive model for precipitation strengthened alloys: theory and application. *Materials Science and Engineering: A*, 25(2):213–220, 2009.

[43] D. A. Porter and K. E. Easterling. *Phase transformations in metals and alloys, third edition (revised reprint)*. Taylor & Francis, 1992.

[44] P. Shewmon. *Diffusion in solids*. Wiley, 1991.

[45] R. E. Reed-Hill. *Physical metallurgy principles*. University series in basic engineering. Van Nostrand, 1973.

[46] H. C. Yu, A. Van der Ven, and K. Thornton. Theory of grain boundary diffusion induced by the Kirkendall effect. *Applied Physics Letters*, 93(9):091908, 2008.

[47] A. Van der Ven, H. C. Yu, G. Ceder, and K. Thornton. Vacancy mediated substitutional diffusion in binary crystalline solids. *Progress in Materials Science*, 55(2):61 – 105, 2010.

[48] K. Maier, H. Mehrer, E. Lessmann, and W. Schüle. Self-diffusion in nickel at low temperatures. *Physica Status Solidi B*, 78(2):689–698, 1976.

[49] H. Bakker. A curvature in the ln D versus 1/T plot for self-diffusion in nickel at temperatures from 980 to 1400 °C. *Physica Status Solidi B*, 28(2):569–576, 1968.

[50] A. Seeger, G. Schottky, and D. Schumacher. The contribution of multiple vacancies to self-diffusion. *Physica Status Solidi B*, 11(1):363–370, 1965.

[51] C. L. Zacherl. *A computational investigation of the effect of alloying elements on the thermodynamic and diffusion properties of fcc Ni alloys, with application to the creep rate of dilute Ni-X alloys*. PhD thesis, The Pennsylvania State University, 2012.

[52] S. Schuwalow, J. Rogal, and R. Drautz. Vacancy mobility and interaction with transition metal solutes in Ni. *Journal of Physics: Condensed Matter*, 26(48):485014, 2014.

[53] M. E. Glicksman. *Diffusion in solids: field theory, solid-state principles, and applications*. John Wiley and Sons, 1999.

[54] M. Mantina, Y. Wang, R. Arroyave, L. Chen, Z. Liu, and C. Wolverton. First-principles calculation of self-diffusion coefficients. *Physical Review Letters*, 100(21):215901, 2008.

[55] A. Seeger and D. Schumacher. On the analysis of nonlinear Arrhenius plots of self-diffusion coefficients for *fcc* metals. *Materials Science and Engineering*, 2(1):31–36, 1967.

[56] G. H. Vineyard. Frequency factors and isotope effects in solid state rate processes. *Journal of Physics and Chemistry of Solids*, 3(1-2):121–127, 1957.

[57] H. Eyring. The activated complex in chemical reactions. *The Journal of Chemical Physics*, 3(2):107–115, 1935.

[58] K. Compaan and Y. Haven. Correlation factors for diffusion in solids. *Transactions of the Faraday Society*, 52:786–801, 1956.

[59] A. B. Lidiard. CXXXIII. Impurity diffusion in crystals (mainly ionic crystals with the sodium chloride structure). *Philosophical Magazine Series 7*, 46(382):1218–1237, 1955.

[60] A. D. Leclaire and A. B. Lidiard. LIII. Correlation effects in diffusion in crystals. *Philosophical Magazine*, 1(6):518–527, 1956.

[61] J. R. Manning. Correlation factors for impurity diffusion. *bcc*, diamond, and *fcc* structures. *Physical Review*, 136(6A):A1758–A1766, 1964.

[62] A. D. Leclaire. Solute effects in diffusion. *Thin Solid Films*, 25(1):1–14, 1975.

[63] K. N. Goswami and A. Mottura. Can slow-diffusing solute atoms reduce vacancy diffusion in advanced high-temperature alloys? *Materials Science and Engineering: A*, 617:194–199, 2014.

[64] J. R. Manning. Correlation factors for diffusion in nondilute alloys. *Physical Review B*, 4:1111–1121, 1971.

[65] J. R. Manning. Correlation effects in impurity diffusion. *Physical Review*, 116:819–827, 1959.

[66] M. P. Allen and D. J. Tildesley. *Computer simulation of liquids*. Oxford University Press, 2000.

[67] D. Frenkel and B. Smit. *Understanding molecular simulation (second edition)*. Academic Press, 2002.

[68] N. Metropolis, A. W. Rosenbluth, M. N. Rosenbluth, A. H. Teller, and E. Teller. Equation of state calculations by fast computing machines. *The Journal of Chemical Physics*, 21(6):1087–1092, 1953.

[69] J. Rogal. *Stability, composition and function of palladium surfaces in oxidizing environments: a first-principles statistical mechanics approach*. PhD thesis, Freie Universität Berlin, Berlin, 2006.

[70] A. F. Voter. Introduction to the kinetic Monte Carlo method. In K. E. Sickafus, E. A. Kotomin, and B. P. Uberuaga, editors, *Radiation Effects in Solids*, pages 1–23, Springer Netherlands, 2007.

[71] J. R. Norris. *Markov Chains*. Cambridge University Press, 1997.

[72] H. C. Kang and W. H. Weinberg. Dynamic Monte Carlo with a proper energy barrier: Surface diffusion and two-dimensional domain ordering. *The Journal of Chemical Physics*, 90(5):2824–2830, 1989.

[73] K. A. Fichthorn and W. H. Weinberg. Theoretical foundations of dynamical Monte Carlo simulations. *The Journal of Chemical Physics*, 95(2):1090–1096, 1991.

[74] A. B. Bortz, M. H. Kalos, and J. L. Lebowitz. A new algorithm for Monte Carlo simulation of Ising spin systems. *Journal of Computational Physics*, 17(1):10–18, 1975.

[75] Y. A. Du, J. Rogal, and R. Drautz. Diffusion of hydrogen within idealized grains of *bcc* Fe: a kinetic Monte Carlo study. *Physical Review B*, 86(17):174110, 2012.

[76] R. E. Howard and J. R. Manning. Kinetics of solute-enhanced diffusion in dilute face-centered-cubic alloys. *Physical Review*, 154(3):561–568, 1967.

[77] A. D. Leclaire. Solute diffusion in dilute alloys. *Journal of Nuclear Materials*, 69-70:70–96, 1978.

[78] I. V. Belova and G. E. Murch. Enhancement of solute self-diffusion in *fcc* alloys. *Philosophical Magazine*, 86(12):1615–1629, 2006.

[79] J. M. Sanchez, F. Ducastelle, and D. Gratias. Generalized cluster description of multicomponent systems. *Physica A: Statistical Mechanics and its Applications*, 128(1-2):334–350, 1984.

[80] A. Van der Ven and G. Ceder. First principles calculation of the interdiffusion coefficient in binary alloys. *Physical Review Letters*, 94(4):045901, 2005.

[81] A. Van der Ven, J. C. Thomas, Q. Xu, B. Swoboda, and D. Morgan. Nondilute diffusion from first principles: Li diffusion in Li_xTiS_2. *Physical Review B*, 78(10):104306, 2008.

[82] A. Van der Ven, J. C. Thomas, Q. Xu, and J. Bhattacharya. Linking the electronic structure of solids to their thermodynamic and kinetic properties. *Mathematics and Computers in Simulation*, 80(7):1393–1410, 2010.

[83] A. Walle and G. Ceder. Automating first-principles phase diagram calculations. *Journal of Phase Equilibria*, 23(4):348–359, 2002.

[84] A. Van der Ven and G. Ceder. Vacancies in ordered and disordered binary alloys treated with the cluster expansion. *Physical Review B*, 71(5):054102, 2005.

[85] A. Van der Ven, G. Ceder, M. Asta, and P. D. Tepesch. First-principles theory of ionic diffusion with nondilute carriers. *Physical Review B*, 64(18):184307, 2001.

[86] P. Hohenberg and W. Kohn. Inhomogeneous electron gas. *Physical Review*, 136:B864–B871, 1964.

[87] W. Kohn and L. J. Sham. Self-consistent equations including exchange and correlation effects. *Physical Review*, 140:A1133–A1138, 1965.

[88] D. S. Sholl and J. A. Steckel. *Density functional theory: a practical introduction.* Wiley, 2009.

[89] W. E. Pickett. Pseudopotential methods in condensed matter applications. *Computer Physics Reports*, 9(3):115–197, 1989.

[90] D. Vanderbilt. Soft self-consistent pseudopotentials in a generalized eigenvalue formalism. *Physical Review B*, 41(11):7892–7895, 1990.

[91] P. E. Blöchl. Projector augmented-wave method. *Physical Review B*, 50:17953–17979, 1994.

[92] G. Henkelman, B. P. Uberuaga, and H. Jónsson. A climbing image nudged elastic band method for finding saddle points and minimum energy paths. *The Journal of Chemical Physics*, 113(22):9901–9904, 2000.

[93] H. Jónsson, G. Mills, and K. W. Jacobsen. Nudged elastic band method for finding minimum energy paths of transitions. In B. J. Berne, G. Ciccotti, and D. F. Coker, editors, *Classical and Quantum Dynamics in Condensed Phase Simulations*, pages 385–404. World Scientific, 1998.

[94] G. Kresse and J. Furthmüller. Efficient iterative schemes for *ab initio* total-energy calculations using a plane-wave basis set. *Physical Review B*, 54:11169–11186, 1996.

[95] G. Kresse and D. Joubert. From ultrasoft pseudopotentials to the projector augmented-wave method. *Physical Review B*, 59:1758–1775, 1999.

[96] J. P. Perdew, K. Burke, and M. Ernzerhof. Generalized gradient approximation made simple. *Physical Review Letters*, 77:3865–3868, 1996.

[97] M. Methfessel and A. T. Paxton. High-precision sampling for Brillouin-zone integration in metals. *Physical Review B*, 40:3616–3621, 1989.

[98] G. Henkelman and H. Jónsson. Improved tangent estimate in the nudged elastic band method for finding minimum energy paths and saddle points. *The Journal of Chemical Physics*, 113(22):9978–9985, 2000.

[99] H. J. Monkhorst and J. D. Pack. Special points for Brillouin-zone integrations. *Physical Review B*, 13:5188–5192, 1976.

[100] C. Kittel. *Introduction to solid state physics.* John Wiley & Sons, 2005.

[101] T. Wang, L. Q. Chen, and Z. K. Liu. Lattice parameters and local lattice distortions in *fcc*-Ni solutions. *Metallurgical and Materials Transactions A*, 38(3):562–569, 2007.

[102] R. Nazarov, T. Hickel, and J. Neugebauer. Vacancy formation energies in *fcc* metals: Influence of exchange-correlation functionals and correction schemes. *Physical Review B*, 85(14):144118, 2012.

[103] J. D. Tucker, R. Najafabadi, T. R. Allen, and D. Morgan. *Ab initio*-based diffusion theory and tracer diffusion in Ni-Cr and Ni-Fe alloys. *Journal of Nuclear Materials*, 405(3):216 – 234, 2010.

[104] K. G. Lynn, C. L. Snead Jr, and J. J. Hurst. Positron lifetime studies of pure Ni from 4.2 to 1700K. *Journal of Physics F: Metal Physics*, 10(8):1753–1761, 1980.

[105] J. Wolff, M. Franz, J. E. Kluin, and D. Schmid. Vacancy formation in nickel and α-nickel-carbon alloy. *Acta Materialia*, 45(11):4759–4764, 1997.

[106] A. R. Wazzan and J. E. Dorn. Analysis of enhanced diffusivity in nickel. *Journal of Applied Physics*, 36(1):222–228, 1965.

[107] W. Wycisk and M. Feller-Kniepmeier. Quenching experiments in high purity Ni . *Journal of Nuclear Materials*, 69-70(0):616–619, 1978.

[108] H. Mehrer. Atomic jump processes in self-diffusion. *Journal of Nuclear Materials*, 69-70:38–60, 1978.

[109] J. E. Reynolds, B. L. Averbach, and M. Cohen. Self-diffusion and interdiffusion in gold-nickel alloys. *Acta Metallurgica*, 5(1):29–40, 1957.

[110] J. R. MacEwan, J. U. MacEwan, and L. Yaffe. Self-diffusion in polycrystalline nickel. *Canadian Journal of Chemistry*, 37(10):1623–1628, 1959.

[111] J. R. MacEwan, J. U. MacEwan, and L. Yaffe. Diffusion of Ni^{63} in iron, cobalt, nickel, and two iron-nickel alloys. *Canadian Journal of Chemistry*, 37(10):1629–1636, 1959.

[112] H. Burgess and R. Smoluchowski. Note on self-diffusion of nickel. *Journal of Applied Physics*, 26(4):491–492, 1955.

[113] H. W. Allison and G. E. Moore. Diffusion of tungsten in nickel and reaction at interface with SrO. *Journal of Applied Physics*, 29(5):842–848, 1958.

[114] J. M. Walsh and M. J. Donachie. Interdiffusion in the nickel-tungsten and thoria-dispersed nickel-tungsten systems. *Metal Science Journal*, 3(1):68–74, 1969.

[115] C. Schulze and M. Feller-Kniepmeier. Transmisson electron microscopy of phase composition and lattice misfit in the Re-containing nickel-base superalloy CMSX-10. *Materials Science and Engineering: A*, 281(1-2):204–212, 2000.

[116] D. Lerch, O. Wieckhorst, G. L. W. Hart, R. W. Forcade, and S. Müller. UN-CLE: a code for constructing cluster expansions for arbitrary lattices with minimal user-input. *Modelling and Simulation in Materials Science and Engineering*, 17(5):055003, 2009.

[117] O. Levy, M. Jahnátek, R. V. Chepulskii, G. L. W. Hart, and S. Curtarolo. Ordered structures in rhenium binary alloys from first-principles calculations. *Journal of the American Chemical Society*, 133(1):158–163, 2010.

[118] G. L. W. Hart, V. Blum, M. J. Walorski, and A. Zunger. Evolutionary approach for determining first-principles hamiltonians. *Nature Materials*, 4(5):391–394, 2005.

[119] D. C. Harris. *Quantitative Chemical Analysis.* W. H. Freeman, 2003.

[120] C. Herring. Diffusional viscosity of a polycrystalline solid. *Journal of Applied Physics*, 21(5):437–445, 1950.

[121] J. Weertman. Creep of indium, lead, and some of their alloys with various metals. *Transactions of the American Institute of Mining and Metallurgical Engineers*, 218(2):207–218, 1960.

[122] A. Heckl, S. Neumeier, M. Göken, and R. F. Singer. The effect of Re and Ru on γ/γ' microstructure, γ-solid solution strengthening and creep strength in nickel-base superalloys. *Materials Science and Engineering: A*, 528(9):3435–3444, 2011.

[123] A. P. Miodownik, X. Li, N. Saunders, and J. Ph. Schille. Modelling of creep in nickel based superalloys. In A. Strang, editor, *Parsons 2003: Engineering Issues in Turbine Machinery, Power Plant and Renewables*, pages 779–787. Institute of Materials, Minerals, and Mining, Maney Publishing, London, 2003.